Università degli Studi di Milano Bicocca
Facoltà di Scienze MM.FF.NN.

Ph. D. school of

Materials Science

Modeling elastic and plastic relaxation in Silicon-Germanium heteroepitaxial nanostructures

Advisor:
Prof. Leo Miglio

Doctorate thesis of:
Riccardo Gatti

January 2011

Contents

Outline

The aim of this thesis is the understanding of elastic and plastic relaxation in SiGe heteroepitaxial nanostructures. This issue is addressed by developing ad hoc methods, based on the coupling between linear elasticity theory and numerical simulations in the Finite Element Method (FEM) framework. The outline is the following. Chap. 1 recalls the state of the art and the main features of Ge on Si(001) heteroepitaxial growth, showing that the lattice mismatch between Ge and Si (strain is accumulated in the Ge epilayer) and different growth conditions lead to nucleation of three dimensional islands (elastic relaxation) or layer by layer growth (plastic relaxation via dislocation nucleation). Chap. 2 is focused on the modeling of the elastic relaxation in islands, calculating the detailed elastic field in nanostructures using FEM simulations. Chapter 3, on the contrary, is dedicated to the analysis of plastic relaxation. Thanks to a novel method, developed in the FEM framework, the study of dislocations in heteroepitaxial nanostructures is addressed. Plastic relaxation is analyzed in a layer by layer growth on patterned substrates, highlighting how the patterning could be a viable path to dislocation confinement. In Chap. 4 and Chap. 5 the plastic relaxation in overgrown island is studied. In fact, the elastic relaxation channel is not fully effective and, during the growth, dislocation are nucleated in islands as well. In particular the onset of plasticity (first dislocation nucleation) is calculated in Chap. 4 , exploiting the FEM methodology developed in Chap. 3. Chap. 5 is focused on the nucleation and the evolution of dislocations, at large island volumes. A simple analytical method is used to determine periodic dislocation nucleation occurring in islands, while a suitable adapted Dislocation Dynamics (DD) code is used to predict the dislocation microstructure deposited at interface between islands and substrate.

1

State of the art

Silicon is the material which has dominated the semiconductor industry for over 30 years, even though the first transistor was fabricated using Germanium as active material. The reasons are simple. Silicon-based technology has the clear advantage of a low-cost and an easy processing that made it the standard technology for microelectronic applications. Nowadays silicon devices has reached the nano-meter scale. Therefore the size has become critical from a technological point of view. In fact, the nanometer scale it recognized as the scale at which a top-down approach is ineffective to shrink the size down of any device, like a Field Effect Transistor (FET). Due to the fatigue of keeping the reliable top-down approach alive, researchers has been driving importance to bottom-up approaches where Silicon can still be the main actor. This is the reason why SiGe heteroepitaxial self-assembled nanostructures have attracted a considerable interest in the development of new electrical and optical devices. The aim of this thesis is the basic study of the physical properties that play in determining the formation and the evolution of such self-assembled nanostructures.

1.1 Main features of Epitaxy

Epitaxy is defined as a controlled phase transition that leads to a single crystalline solids [1]. In this process a material, called *epilayer*, is deposited onto a crystalline solid, called *substrate*, of a given structure. In epitaxy epilayer grows layer by layer and the crystallographic orientation is determined by the exposed surface of the substrate. If the epilayer and the substrate are of the same material such process is called *homoepitaxy*. In contrast, when atoms of material A grow on a material B (A and B with the same crystalline structure) the process is called *heteroepitaxy*. The epilayer adopts the in-plane lattice parameter of the substrate. If A has different lattice parameter than B, elastic energy is stored in the epilayer. In heteroepitaxy three growth modes are observed [2]: Frank Van der Merve, Volmer-Weber and Stranski-Krastanow mode. The three mode, sketched in Fig. 1.1, can be described as layer by layer two dimensional growth, island growth and layer by layer (*wetting layer*) plus island growth respectively. The growth mode is mainly governed by surface energies and by lattice mismatch.

In lattice matched systems (A and B have the same lattice constant) the growth mode is governed by surface energy only. Let us call γ_{epi} the surface epilayer energy, γ_{int} the energy

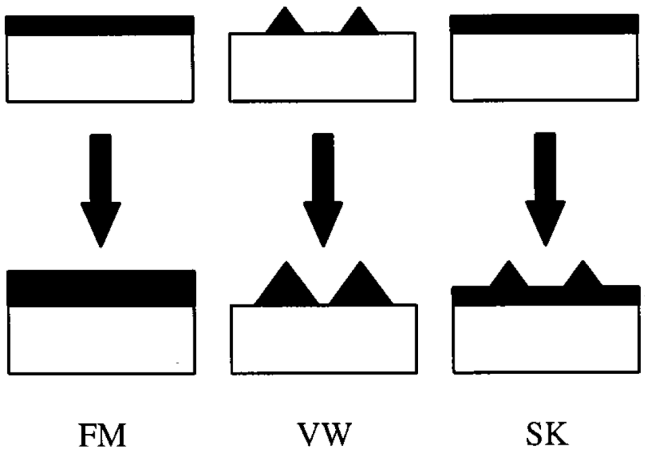

FIGURE 1.1: Schematic diagrams of the three growth modes for heteroepitaxial systems: Frank-van der Merwe (FM), Volmer- Weber (VW), and Stranski-Krastanow (SK).

of the interface between A and B and γ_{sub} the surface substrate energy. If $\gamma_{epi}+\gamma_{int} < \gamma_{sub}$, the deposited material wets the substrate, and the growth proceeds in the FM mode. A change in $\gamma_{epi} + \gamma_{int}$ alone may drive a transition to the FM to VW growth mode: the epilayer either wets the substrate or does not. In lattice mismatched systems there is an additional possibility. In case of systems with small interface energy but large lattice mismatch, SK growth mode is favored. Initial growth is layer by layer, but because a thicker layer has large elastic energy, islands are formed to relax the strain.

1.2 SiGe/Si heteroepitaxy

Silicon and Germanium are group-IV semiconductors. At room temperature they are found in diamond crystalline structure [3], so that each atom has four nearest neighbours (in bulk) [4]. Lattice constants, along the [100] direction, are $a_{Si} = 5.432\,\text{Å}$ and $a_{Ge} = 5.658\,\text{Å}$ [5]. Thus, Ge/Si is a mismatched system, where the difference in lattice parameter accounts for about 4%. From a chemical point of view, Ge and Si are very similar. Alloying is favored and $Si_{1-X}Ge_X$ (X is the Ge content) alloys are fully miscible in the whole composition range for temperatures used in heteroepitaxy [6]. By tuning the Ge content X, the lattice mismatch between the alloy and the substrate varies from 0% to 4%. The surface energy $Si_{1-X}Ge_X$ is lower than the surface energy of Si, and their interface energy is small, so the Ge content x is a key parameter in determining the heteroepixial growth mode of SiGe alloys on Si. In the high Ge content regime the epilayer growth in SK mode. The initial growth occurs layer by layer, then three-dimensional islands are formed to relieve the elastic energy stored in the system (elastic relaxation). In the low Ge content regime, lattice strain plays a minor role, the epilayer grows forming a pseudomorphic layer following the FM mode. As the epilayer become thicker and thicker, the elastic energy stored in the pseudomorphic epitaxial layer increases and dislocation nucleation is observed (plastic relaxation). Besides the alloy lattice parameter, the temperature and the growth technique (Molecular Beam Epitaxy (MBE) and Chemical Vapor Deposition (CVD) the most common) are of relevant importance in determining the growth mode. For instance varying the temperature is possible to change the growth mode from SK or FM (or viceversa). We can conclude that

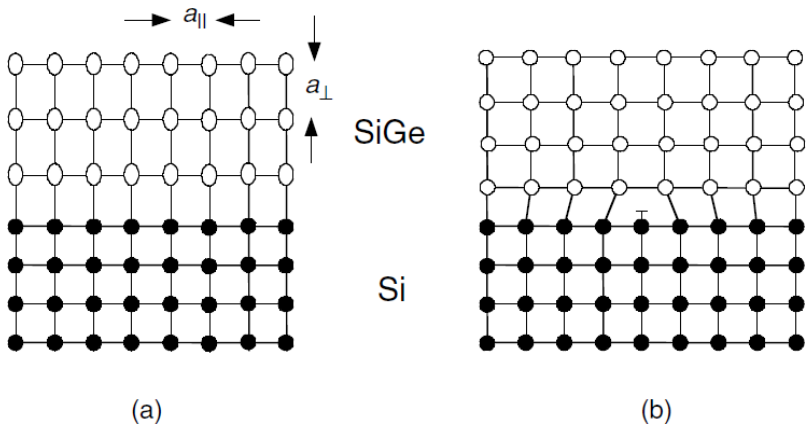

FIGURE 1.2: Sketch of a SiGe layer grown epitaxially on a Si substrate. (a) Pseudomorphic case with tetragonal distortion. (b) Plastic relaxation case with introduction of one dislocation.

in $Si_{1-X}Ge_X$/Si heteroepitaxy strain (Ge content) and deposition condition are the main actors in determining the growth mode. In the following part of the chapter we focus our attention on $Si_{1-X}Ge_X$ on Si(001) substrate, studying strain relief mechanism leading to a 3D morphology (elastic relaxation) rather than dislocation nucleation (plastic relaxation).

1.3 Layer by layer growth: plastic relaxation

Low lattice mismatch, that is low Ge content, leads $Si_{1-X}Ge_X$ epilayers to layer by layer growth (FM). The relaxed lattice parameter a_e of the epilayer is different to the relaxed lattice parameter of the substrate a_s. Thus a lattice mismatch strain f is defined as follows :$f = (a_e - a_s)/a_s$. In the $Si_{1-X}Ge_X$/Si(001) system the mismatch f is positive and can vary from 0 to 0.04 as X varies from 0 to 1. In the first steps of the growth, as mentioned, the heteroepitaxial layer tends to grow coherent or pseudomorphic with the substrate, that is the in plane lattice parameter $a_{\|}$ of heteroepitaxial layer is equal to the substrate lattice parameter and the unit cells are tetragonal distorted, as shown in Fig. 1.2 (a). Therefore the pseudomorphic layer has a in-plane strain $\varepsilon_{\|}$ equal to the lattice mismatch : $\varepsilon_{\|} = f$. Increasing the thickness of the epitaxial layer, the elastic energy stored in the pseudomorphic layer grows up.

At a certain thickness, called critical thickness h_c, is energetically more favorable to introduce a random network of Misfit Dislocations [1] (MD) ,at the interface between the substrate and the growing layer, to relax some of the mismatch strain (see Fig. 1.2 (b)). Thus beyond the critical thickness of the epilayer, a part of the stored energy is relaxed plastically by MD network (plastic relaxation), as shown in Fig. 1.3.

Different models have been developed to predict the critical thickness of the strained epitaxial layer. Van der Merwe [8] produced a thermodynamic equilibrium model comparing the strain energy relaxed by a misfit dislocation and the energy cost associated to the introduction of the dislocation itself in the system. The critical thickness is defined as:

$$h_c = \frac{b}{8\pi f}\left(\frac{1-\nu\cos^2\beta}{(1+\nu)\cos\lambda}\right)\left[\ln\left(\frac{h_c}{b}\right)+1\right] \tag{1.1}$$

[1] the basic concepts of dislocation in hereroepitaxial structures are recalled in App. B

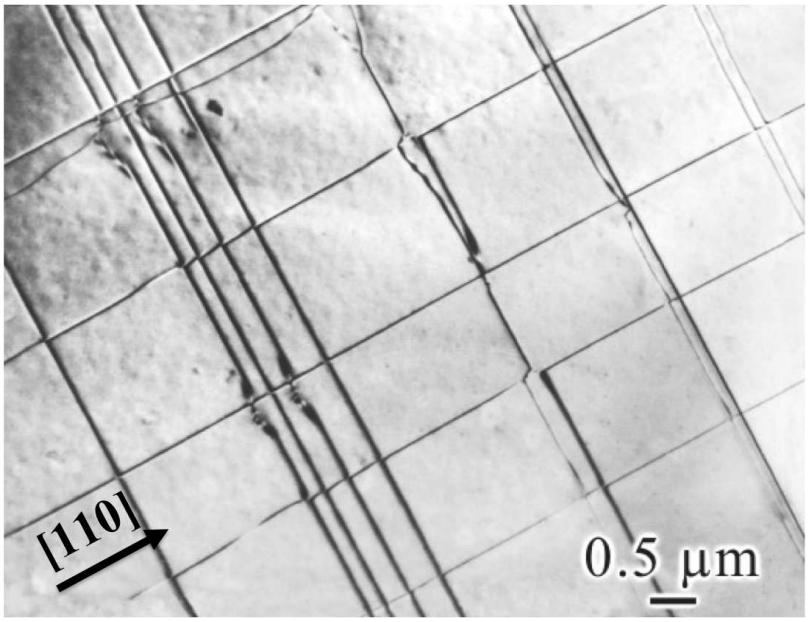

FIGURE 1.3: Misfit dislocation network at the interface of $Si_{0.98}Ge_{0.02}$/Si heteroepitaxial film [7].

where b is the misfit dislocations Burgers vector, β is the angle between b and the dislocation line direction and λ is the angle between b and a direction normal to the dislocation line in the epilayer/substrate interface plane (to account for the real component of the dislocation acting on reliving the strain in the epilayer). Matthews and Blakeslee used an equivalent approach, balancing the forces acting on a dislocation terminating at the epilayer surface (threading dislocation) [9]. The critical thickness, in this case, is given by:

$$h_c = \frac{b}{2\pi f}\left(\frac{1-\nu\cos^2\beta}{(1+\nu)\cos\lambda}\right)\left[\ln\left(\frac{h_c}{b}\right)+1\right] \tag{1.2}$$

where β is the angle between the dislocation line and its Burgers vector and λ is the angle between the Burgers vector and the direction in the interface normal to the dislocation line. Notice that in both model h_c is proportional to f^{-1} that is to ε^{-1}. Therefore as the lattice mismatch between epilayer and substrate decrease, the thickness for which a film remains pseudomorphically distorted (stable) increases. It was observed experimentally that many pseudomorphic layers could be grown well above the critical thickness values predicted from the above equilibrium theories. These results can be explained considering a non-equilibrium growth condition. Epilayers with $h > h_c$ are often found in a metastable strained state. The transition to stable epilayer is achieved by annealing at high temperature. In fact high growth temperatures and post growth annealing, leads to a good agreement between experimental critical thickness and the values predicted by Eq. 1.2. Kinetic barriers have to be overcome to appreciate the nucleation and the motion of dislocation. Some attempts to model the above described kinetic limitation are due to People and Bean [10, 11], Dodson and Tsao [12, 13] and Houghton [14]. By the way, the kinetic effects are strongly related to the peculiar growth condition, such as the substrate temperature, the initial dislocation density and growth rate making this field still challenging.

1.4 Islands formation: elastic relaxation

High lattice mismatch that is high Ge content leads $Si_{1-X}Ge_X$ epilayers to Stranski-Krastanow growth mode. SK growth of coherent Ge islands on Si(001) was firstly reported by Eaglesham and Cerullo at Bell Labs in 1990 [15]. Given a flat surface of Si(001), Ge accommodates first as a flat film of no more than 3 ML, called wetting layer. Even in the case of nominally-pure Ge deposition over Si, wetting layer is known not to reach 100% Ge concentration, while it ends at values of $\simeq$80% Ge, as demonstrated by recent photoluminescence experiments [16]. Quantitative similar results, on the other hand, have been obtained via dedicated atomistic simulations [17], also with a Monte Carlo approach [18] of allowed Ge-Si chemical mixing during Ge layer-by-layer deposition.

Deformed in the pseudomorphic structure, the wetting layer stores elastic energy that will find paths to be released. By increasing the amount of deposited material, because of the high lattice mismatch, the elastic energy stored in the lattice is sufficient to nucleate 3D nanostructures, called quantum dots or *islands*, arising from the substrate in a bottom-up fashion. Ge-on-Si quantum dots represent a more effective route towards elastic relaxation with respect to a flat film, at the cost of an extra surface energy exposed.

Islands are best represented with the set of crystallographic facets composing them, together with their aspect ratio ρ, defined as the ratio between the island height h and the square root of the island base surface S:

$$\rho \equiv \frac{h}{\sqrt{S}}.$$

The following paragraphs describe the main features of Ge quantum dots on Si. The first islands to appear are unfacetted, low-aspect-ratio nanostructures, called pre-pyramids. The nucleation barrier to nucleate such structures is zero [19], which accounts for its actual experimental observation. At later stages of growth, those structures transform into fully-3D faceted islands, with the shape of a truncated pyramid [20]. Evidently Ge islands exposes defined crystallographic facets among all the possible available; this already implies that there must be facets with higher and others with lower surface energy, so that Ge islands, among all the possible ones, have shapes such that they expose the lowest-energetic ones. Facet stability is separated into the so-called "major" and "minor" stable surfaces, a systematic study of which was made by Gai et al [21].

Before transition to a full-3D structure, it was shown the stability of intermediate, metastable shapes of Ge elongated "huts" [22], particularly visible under specific growth conditions.

The peculiar shape of *mature* Ge islands on Si(001) is now briefly reviewed here. It is worth starting from the plot reported in Fig. 1.4, where the aspect ratio is plotted against the island base size. Smaller islands are shaped as square-base pyramids bounded with {105} facets: for this reason, those are usually called "{105} pyramids". Their aspect ratio is thus 0.1: these islands should be considered as rather flat, since facets join the substrate with an angle of 11.4°. These pyramids are the first to appear because the extra-surface cost associated with island formation is balanced by the gain of exposing a low-energy crystallographic facet, together with the gain in elastic energy compared with a flat wetting layer.

Among others, Ge {105} facet with the so-called "rebounded-step" (RS) reconstruction shows to be sensitive to lattice strain condition. Correspondent surface energy, in fact,

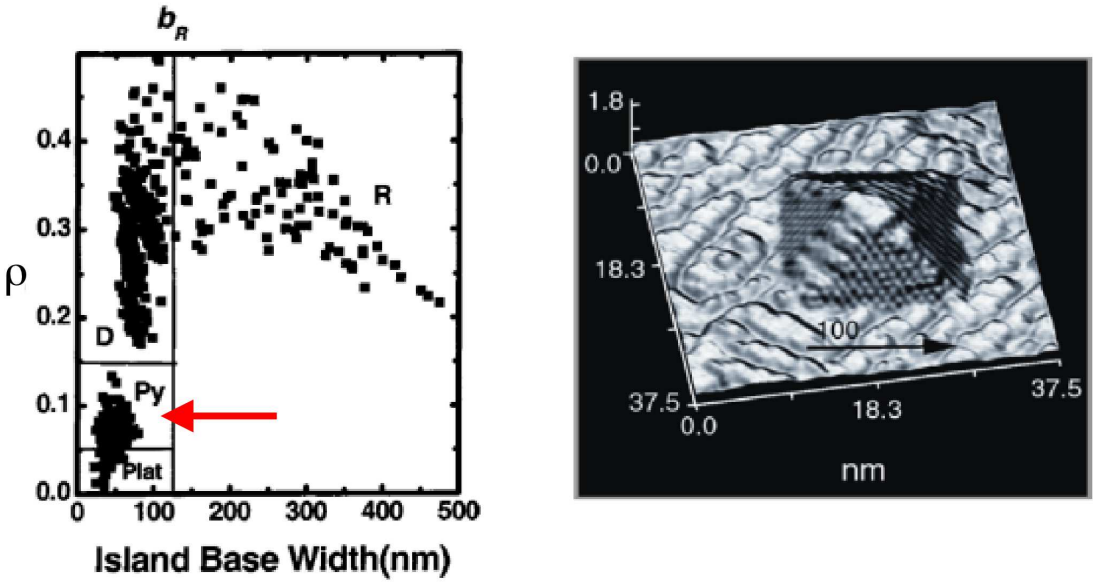

FIGURE 1.4: (left) Aspect ratio versus island base plot for a typical sample of Ge islands grown on Si(001). (right) The first 3D-islands to appear are the so-called {105} pyramids, like the example (right) here shown (from [23]).

decreases with increasing strain [24]; this feature is not found in other crystallographic facets [25]. The peculiar surface energy of the {105}-RS Ge surface is critical in determining the stability of the corresponding Ge huts/pyramids with respect to the same amount of material displaced as a wetting layer. Dedicated atomistic molecular-dynamics simulations, first carried out by Raiteri et al [26] and later by Liu [27], confirmed the gain in energy which is accompanied by island nucleation, with respect of a flat wetting layer. Finally, dedicated atomistic simulations of {105}-RS reconstructed ridges were able to estimate the edge energy to be of the order of 8 meV/Å [28].

It is found that, with increasing amount of deposited material, a new island shape appears: it is called dome [29] and corresponds to a more complex, high-aspect ratio ($\rho \simeq 0.2$) island. It is interpreted as a first-order shape transition from pyramids [30]. A typical dome, recorded as a STM image, is shown in Fig. 1.5. Domes cover a range of aspect ratios varying from ~ 0.17 to ~ 0.26: they thus represent an ensemble of different islands, at variance with {105} pyramids which are always located at $\rho = 0.1$ (simply for geometrical reasons). As clear from Fig. 1.5, there is thus a *gap* in aspect ratio between pyramids and domes, confirmed by an extensive amount of experiments [31]. At the same time, experiments carried out at low deposition temperature with chemical sapor deposition (CVD), showed that the transition can be continuous in special cases, without an aspect-ratio gap [32].

Domes are composed by this set of facets: {15,3,23} [33] and {113} [34, 35] at the base, capped with {105} facets terminated with a flat (001) facet at their top. It is relevant to note that this model corresponds to one peculiar realization of a dome shape of a given aspect ratio, while the relative size of each facet type can vary. For this reason, it is more convenient to refer to "dome" any island shape built with {15,3,23}, {113}, {105} and (001) facets, independently from their relative size over the island.

The atomic-scale mechanism that triggers the shape transition from pyramid to dome is the accumulation of Ge at the top of a {105} pyramid, because it represents a local

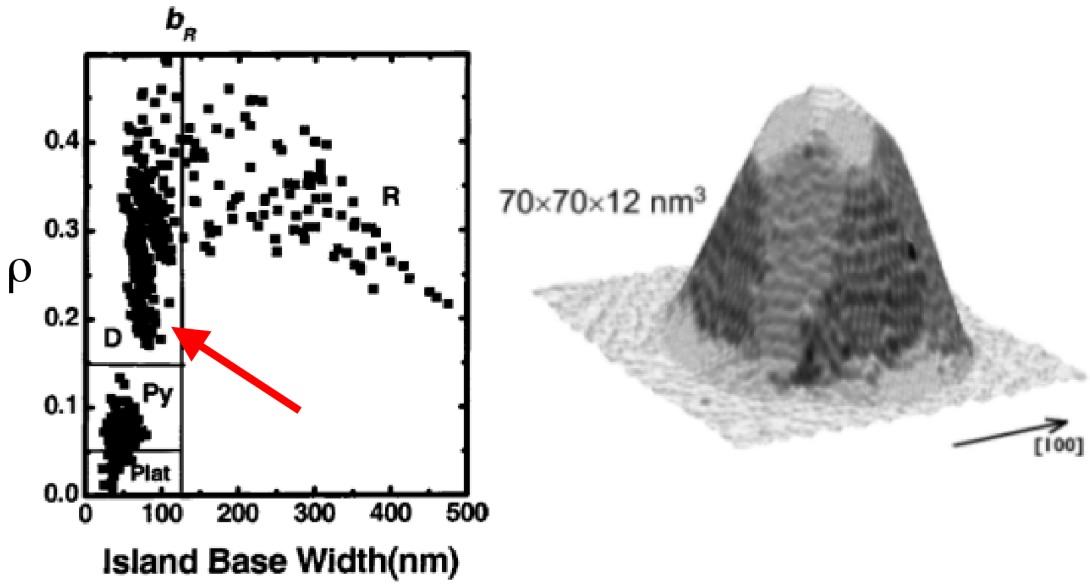

FIGURE 1.5: (left) Aspect ratio versus island base plot of a typical sample of Ge islands grown on Si(001). (right) STM image of a dome of typical size and shape (from [39]).

minimum of the pyramid chemical potential [36].

Once domes are formed, material is extracted from the island periphery, forming trenches. Trenches represent a newly available source of Si to mix with Ge [37] and act as centers of relaxation for the island elastic energy [38]. Intermixing phenomenon takes place, the Ge islands starts to incorporate Si. The island changes its composition (decrease of Ge content means reduction of the mismatch) and so lowering its elastic energy. This issue will be addressed in the next section.

Recently [40] a new, still defect-free, island shape was discovered. It is called "barn" in compliance with a similar island shape observed in different growth conditions [41]. Barn is composed of {111}, {20,4,23}, {23,4,20}, {15,3,23}, {113}, {105} and {001} facets. With steeper facets, a barn points at aspect ratios ~ 0.3, becoming the highest coherent island found on a flat Si (001) substrate. It is interesting to point out that {20,4,23} and {23,4,20} are stable facets for Si and not for Ge [42], so that strong intermixing is believed to be the key ingredient in the dome-to-barn shape transition. A sketch of the barn shape, together with the position on the (ρ, V) plot, is reported in Fig. 1.6

1.5 Intermixing in SiGe Islands

The SK growth leads to islands formation, as mentioned in the previous section. Increasing the amount Ge deposited, transition from shallow to steeper islands is observed, in order to minimize the energy of the system. The pyramid-to-dome shape transition is accompanied by the formation of trenches surrounding the island [38]. Trenches dig into the Si substrate [43], thus representing a fresh source of Si at that stage of growth. Ge islands start to incorporate Si and intermixing phenomenon takes place. The driving force towards Si incorporation is the entropy of mixing that leads to alloy Si and Ge. By lowering the Ge content the local lattice parameter of a $Si_{1-X}Ge_X$ alloy comes closer to the Si bulk decreasing the lattice mismatch. The compositional profile of the SGe island is clearly affected

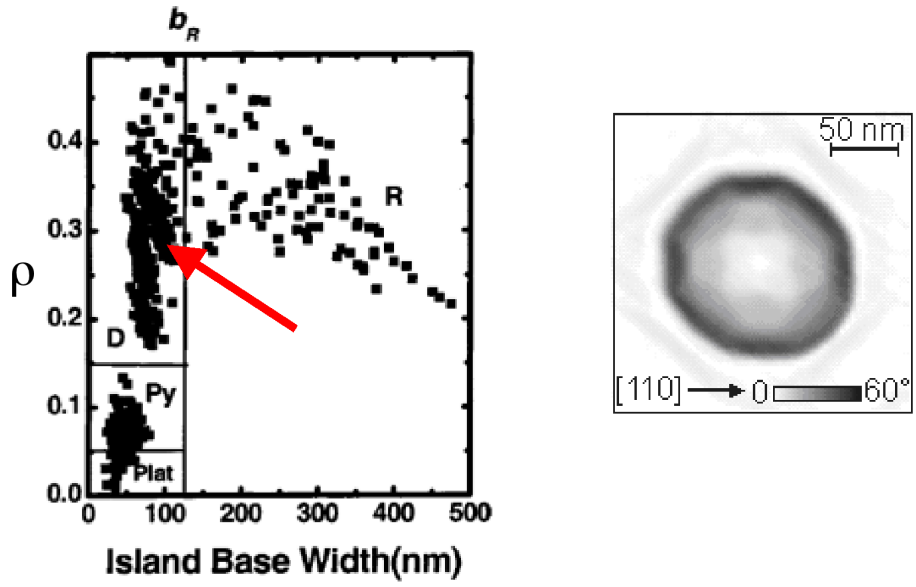

FIGURE 1.6: (left) Aspect ratio versus island base plot of a typical sample of Ge islands grown on Si(001). (right) STM image of a barn-shaped island from top view (from [40]).

by the intermixing phenomenon. The intermixing of the deposited Ge, with Si popping up from the substrate, which has been shown to decrease the Ge content with increasing growth temperatures, both in CVD [44] and MBE [45, 46] growths. One experimental technique successfully applied to study the composition profiles inside island is etching [47]. By the use of a chemical solvent (the etchant), islands can be selectively removed over the substrate, allowing for the study of the reaction of the islands upon attack with a solution able to remove SiGe alloy, but not pure Si. In particular, wet chemical etching with a 30% solution of hydrogen peroxide (H_2O_2) selectively removes $Si_{1-X}Ge_X$ alloys with compositions having $x > 0.65$ (i.e. Ge-rich material) [48]. At this stage, etching is thus useful to explore the 65% Ge isocompositional profile inside islands, which is already enough to get into some details of the anisotropic island Ge concentration. Recent experiments, carried out with etchants able to remove material up to the complete dissolution of the islands, were carried out assisted by atomic force microscopy (AFM) scan of the partially etched island at every etching step [49]. Known the etchant composition selectivity at every etching step, it is finally possible to reconstruct a cross-sectional map of the Ge content, as reported in Fig. 1.7.

The maps come already very useful to get the first insights of the actual Ge distribution inside islands (domes). The general features are here listed. First of all, a Ge-rich core is clearly present at the top of the island. Second, Si-rich areas are visible at the island corners, which can be explained as the accumulation of material driven by strain by intermixing, during the trenches excavation, as mentioned above. Finally, even if it cannot be inferred from the maps of Fig. 1.7, it is expected a pure-Ge layer at the very free island surface. This happens because of the reduced surface tension of Ge with respect to Si: the energy of a dangling bond, in fact, is 0.96 eV for Ge and 1.15 eV for Si from Tersoff potential [50]. This effect is called "surface segregation" and consists in the tendency of material to expose Ge to a greater extent than Si. This effect has thus strong influence especially when Si is deposited on Ge, where now surface segregation becomes a direct driving force towards

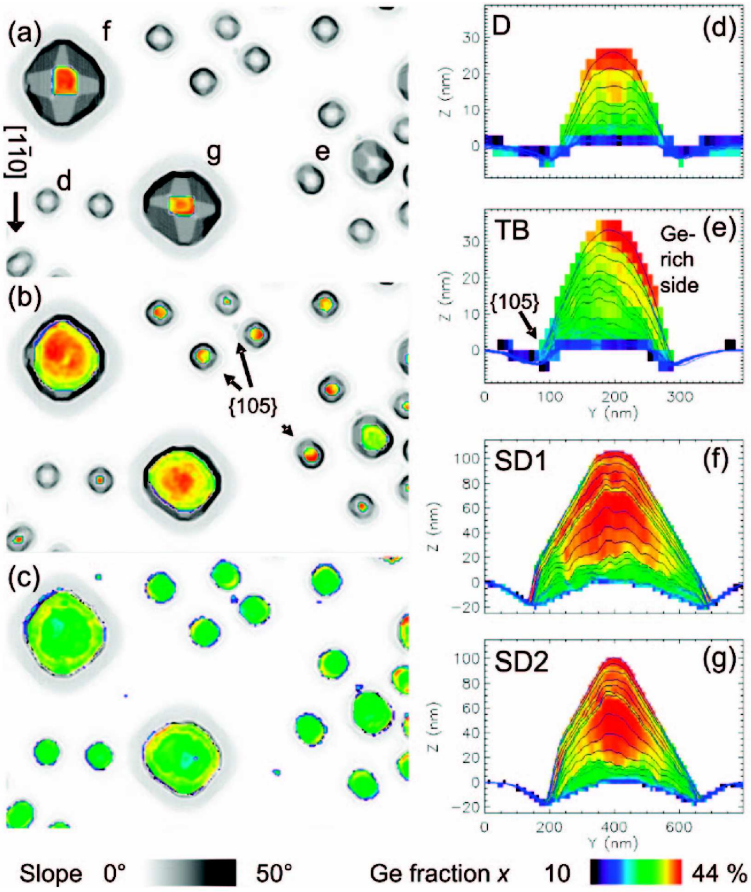

FIGURE 1.7: Cross-section composition profile reconstructed from etching experiments for a dome (d), a transition barn (e) and two superdomes (f,g). Top view of the sample under etching is in (a,b,c). The average Ge content in the islands is $\simeq 0.36$, The color map reveal that the top of the island is Ge-rich, while the bottom edges, close to trenches are Si rich. Reproduced from [49].

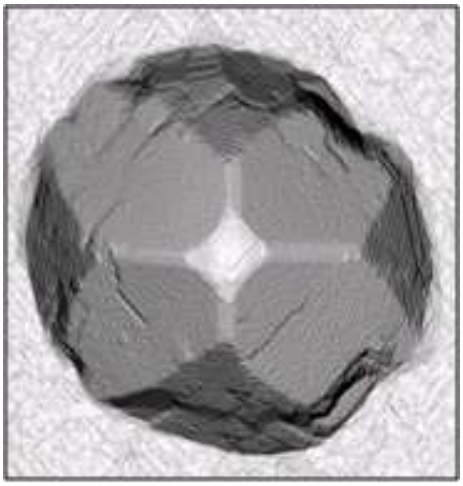

FIGURE 1.8: Typical STM image of a dislocated dome. The presence of the crystallographic defects alter the island growth, making it asymmetric.

intermixing [51].

1.6 Plastic relaxation in SK growth

Evolution towards higher aspect ratios, is abruptly interrupted by the opening of an alternative (plastic) channel for strain relaxation. Islands reach barn shape and, upon further deposition of Ge on the substrate, misfit dislocations are eventually injected (onset of plastic relaxation). Dislocated islands can be distinguished on a sample because their shape loose the symmetry typical of any coherent island, as shown in Fig. 1.8. Dislocation nucleation deeply influences evolution at larger volumes. An intriguing *cyclic growth* regime is actually observed, involving a periodic flattening of the island shape each time a new dislocation (60° dislocation deposited at the SiGe/Si interface) nucleates in the island [52, 53],generating an average decrease in ρ, back to about 0.25-0.27 (Superdome islands [39]. This drop in the aspect ratio is nicely highlighted also in Ref. [44], for samples grown by Chemical Vapor Deposition (CVD).

The cyclic growth phenomenon was observed by real time Transmission Electron Microscopy (TEM) in situ [52, 53] and deduced from the Atomic Force Microscopy (AFM) analysis of the "footprints" left by dislocated islands on the Si substrate [39, 54], after selective wet chemical etching of the SiGe epilayer.

In fig. 1.9 are shown TEM in situ analysis performed at 650° C, during island growth. Fig. 1.11 (a) shows the island after the formation of the first 60° dislocation, close to the island edges. Once dislocation is nucleated, the island becomes more relaxed, hence a preferential site for Ge attachment.

A quick lateral expansion is observed (few seconds) and the island decreases its aspect ratio. Therefore the island increases in size, moving again towards higher aspect ratio (some minutes), reaching superdome shape. As soon the second dislocation nucleation occurs, Fig. 1.11 (b) the islands, again, grows laterally, and the mechanism just described is repeated ciclycally, as shown Fig. 1.11 (c) (d) (e). This is the reason why such process is called cyclic growth. The final pattern formed by the evolution of 60° dislocations during the cyclic growth mechanism is shown in Fig. 1.10, revealing that dislocation forms a series of concentric rings, avoiding the center of the island [55].

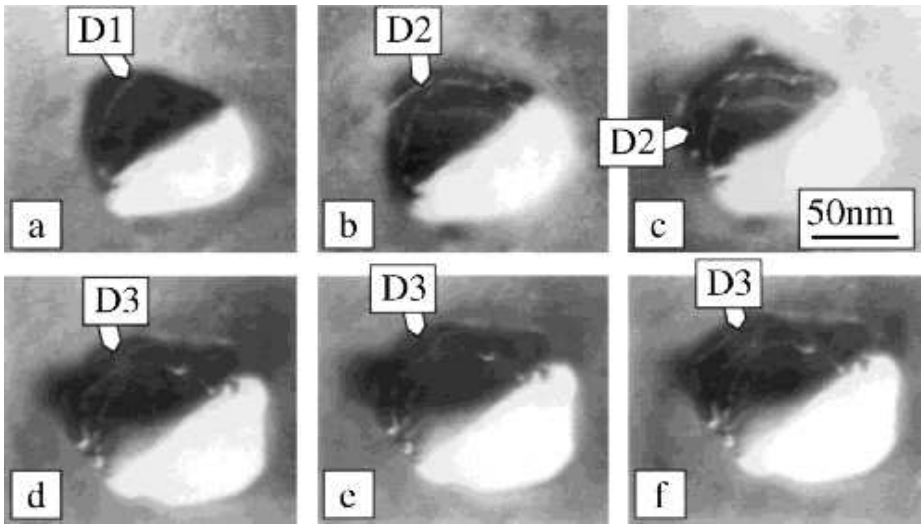

FIGURE 1.9: Evolution of dislocations in a superdome island. The TEM in situ images show the first dislocation nucleated at the island edges (a). A second dislocation event occurs in (b). The island grows to recover its elastic budget and the dislocation evolves in the system (c), till a third nucleation events appears (d). Therefore the island again recover its elastic budget and its aspect ratio. The described process is called *cyclic growth*, periodically dislocation nucleation events are observed. Reproduced from [53]

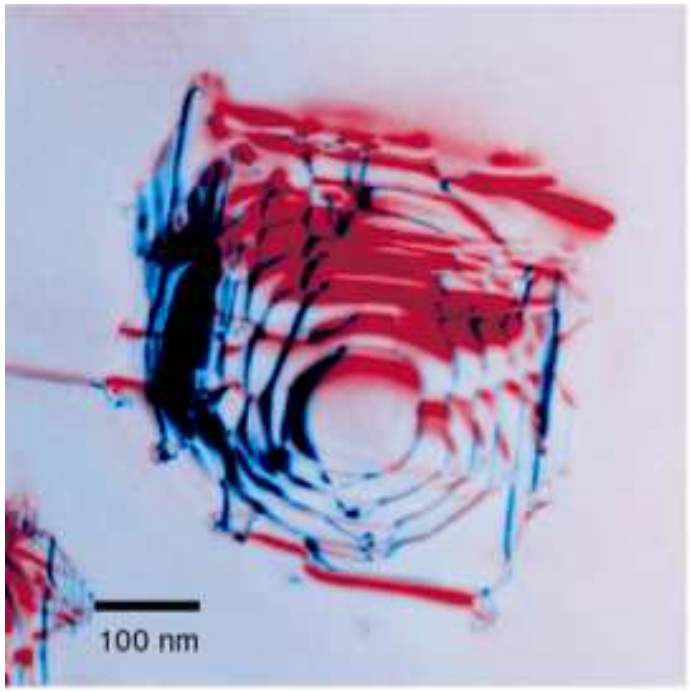

FIGURE 1.10: Dislocation pattern observed at SiGe-Superdome/Si interface. Dislocations form a series of concentric rings, avoiding the center of the island. This image was obtained by superimposition of two dark field (g,3g) weak beam images with g=(220) and g=($\bar{2}$20).

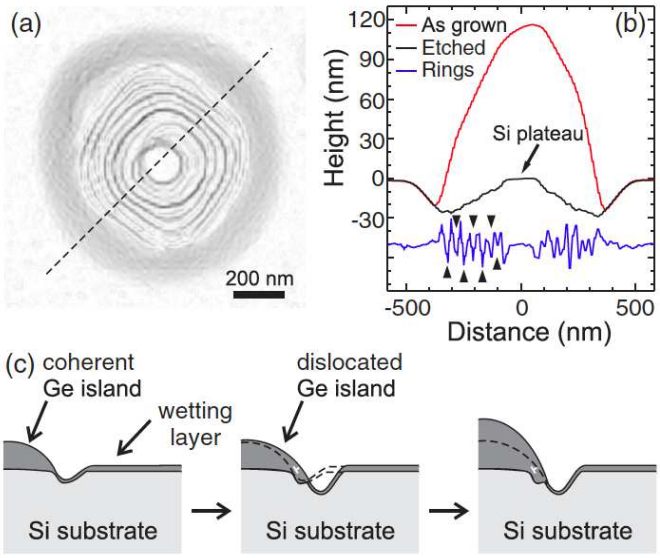

FIGURE 1.11: (a) AFM scan of the tree-ring structure left over by a single superdome after etching. (b) Cross-sectional profile of the same superdome before and after etching taken along the dashed line shown in (a). The bottommost curve represents the numerical second derivative (in arbitrary units) of the AFM topograph of the profile after etching. The solid triangles indicate the position of the rings. (c) Schematic representation of the mechanism leading to the formation of ring structure.Reproduced from [54]

The AFM analysis performed by selective wet etching, confirming the TEM scenario, shows that during cyclic growth a tree-ring structure is left by islands on the Si substrate. In particular the tree-ring structure consists of several nearly concentric, rings surrounding a central plateau. The central Si plateau can be interpreted as the original island base prior to introduction of the first dislocation. Its size can thus be taken as a measure of the critical diameter for the first dislocation introduction [56]. The concentric rings can be ascribed to the cyclic growth mechanism: when an island increases its aspect ratio, a deep trench in the Si substrate at the perimeter of the island base is carved. This stage corresponds to a short steep profile in the AFM scan of the Si substrate. As the critical conditions for one dislocation nucleation are met, sudden lateral expansion of the island is observed, providing a full coverage of the trench bottom line. This stage corresponds to a small plateau in the etched samples. Periodic repetition of these two stages during the cyclic growth gives rise to a clear stepped profile in the Si substrate, which appears in form of concentric grooves in the AFM images. Therefore we can thus interpret the number of rings as the number of dislocations introduced in the island during its growth. The issues about the onset of plastic relaxation, and the evolution of dislocations in "mature" SiGe island will be addressed in chapters 4 and 5.

2

Elastic relaxation in three-dimensional Ge/Si islands

This chapter is devoted to the calculation of the elastic field in realistically-shaped Ge/Si islands. As mentioned in chapter 1 three mechanism are in charge of elastic relaxation: free surfaces relaxation, substrate deformation (both provided by SK growth mode) and alloying due to intermixing phenomenon. A continuum approach based on linear elasticity theory joint with Finite Element Method (FEM) calculations is used to understand free surface relaxation and substrate deformation. After a brief introduction about computational approach adopted to properly simulate with FEM heteroepitaxial structures, a detailed analysis of elastic field in the Stranski-Krastanow nano-islands grown on Si (001) is performed. We followed the evolution of islands in enhancing elastic relaxation towards higher aspect ratio (ρ), from shallow {105} pyramids to steeper barns. The third mechanism in charge of elastic relaxation is investigated in the second part of the chapter. The alloying occurring in the islands during the growth is analyzed with a dedicated Monte Carlo-FEM approach. Thanks to the Monte Carlo algorithm, coupled with FEM, is possible to calculate the variation compositional profile that minimize the elastic energy in system.

2.1 Computational approach

Several approaches can be applied to the computation of the elastic field in Ge/Si islands. Continuum models built in the framework of elasticity theory, that yield analytical solutions, are surely a valid tool to obtain fast, semi-quantitative estimates. Starting from the Green function associated to a point-like inclusion of Ge in a semi-infinite Si substrate [57], the elastic field due to a macroscopic island is obtained integrating this Green function over the island volume. Based on this starting point, a method generally known as "flat-island approximation" was developed [2, 58]. The latter was demonstrated to be valid for low-aspect ratio islands (i.e. {105} pyramids), while expected to generally fail in determining the elastic field in steeper islands. Recently, an improvement of this method has been obtained by taking into explicit account the base-to-top stress relaxation in islands. The improved method has shown to yield a good estimate of the elastic field also for pyramids with ρ similar to domes [59].
However, the critical shortcoming is that the analytical solution can be computed only

for simple island shapes, and/or in two dimensions. Ge/Si systems, on the other hand, are characterized by a rather broad spectrum of island shapes, some of them being very complex, like domes and barns.

Two approaches particularly suited for treating any geometry are classical molecular dynamics (MD) simulations and calculations based on continuum elasticity theory as solved by Finite Element Methods (FEM).

In MD, the system is built atom by atom. Possible many-body interatomic potentials have been proposed for the Si/Ge system. Here we recall the very popular ones introduced by Stillinger and Weber [60] and by Tersoff [50]. One of the advantages of atomistic simulations is that they can handle atomic-scale features like surface reconstructions, defects [61, 62], or non-homogenous distributions of atomic species [63]. The latter phenomenon, called intermixing, has been widely investigated experimentally [64, 65, 47], and it has been shown to strongly influence the global relaxation inside the island [43].

MD simulations have been shown to yield results consistent with experiments in several investigations dealing with Ge islands on Si(001). For example, a total-energy calculation based on the Tersoff potential was used to demonstrate the critical role of facets reconstruction to determine the stability of {105} pyramids [26]. Atomistic calculations represent also a useful tool for the investigation of the elastic-field interaction between islands. When a sequence of Ge/Si layers are grown in a stacked array, islands show a general trend of enhancing the spatial order as the number of Ge/Si layers is increased. While a beautifully simple model based on dipolar fields was shown to capture the main physics of the ordering process [66], MD simulations allowed for a detailed characterization of the strain field generated in Si by buried Ge islands [67, 68]. Interestingly, an increase in lateral ordering was reported also for a single Ge-dot layer on Si(001), and shown to be triggered by partial capping with silicon [69]. Also in this scenario MD simulations proved to be useful, suggesting that the ordering driving force was the elastic interaction between adjacent islands, inducing an energetic unbalance among the facets of the dots, eventually determining an effective lateral motion aimed at increasing the island-island separation [69, 70]. Asymmetric alloying has also been shown to promote lateral motion [70, 71]. In the total-energy island budget, it has been shown that, at least for small islands, the contributions due to island edges are critical to predict the correct size of island nucleation [72, 73]; classical MD simulations have been recently used to directly compute this term [28].

Despite the above reported examples of success in determining key phenomena associated with island-induced strain fields, MD simulations become computationally very demanding when handling systems with more than a few million atoms, so that FEM-based calculations are often applied to treat realistic-scale systems. In the next sections, we show FEM calculations are reliable in computing the elastic field (strain,stress and elastic energy) in realistic Ge/Si islands used. We highlight that FEM allows one for treating complex geometries, and that properly combined with different method FEM allows for handle defects and non-homogenous intermixing in solid.

2.2 Boundary value problem and finite element method

Classical linear elasticity theory describes the equilibrium state of a solid in terms of internal stresses $\sigma_{ij}(u)$, as a function of the displacement field u with respect to the initial position

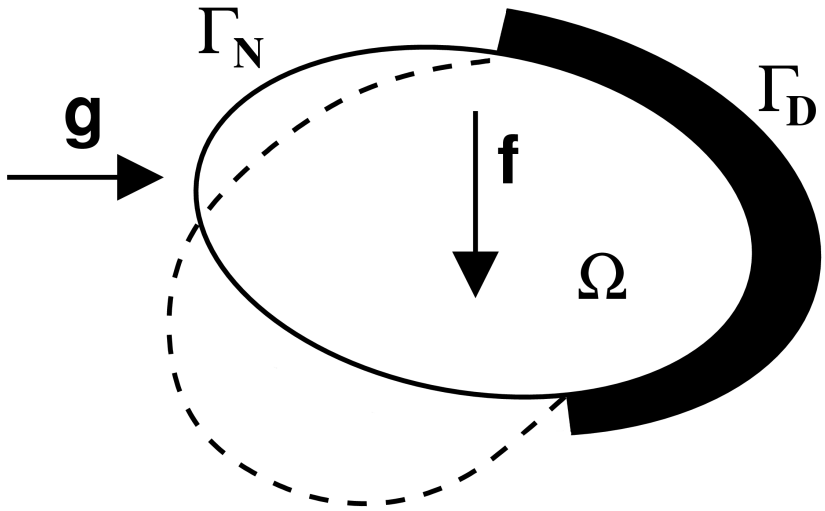

FIGURE 2.1: Sketch of an elastic body Ω with applied forces f and g, and boundary conditions Γ_N and Γ_D. See text and Eqn. 2.1 for details.

[1], and applied external forces f_i. With Fig. 2.1 as a reference, we define the elastic body as the domain Ω, with boundary $\partial\Omega = \Gamma_D \cup \Gamma_N$. Equilibrium equations can be written in a boundary value problem as [74]:

$$\begin{cases} -\sum_{j=1}^{3} \frac{\partial}{\partial x_j}\sigma_{ij}(u) = f_i & \text{inside} \quad \Omega \\ \sum_{j=1}^{3} \sigma_{ij}(u) n_j = g_i & \text{on} \quad \Gamma_N \\ u_i = 0 & \text{on} \quad \Gamma_D \end{cases} \tag{2.1}$$

Γ_N are Neumann boundaries, Γ_D the Diriclet ones, $\mathbf{n}$ is the vector normal to Γ_N, g_i is the force acting on Γ_N. The first equation is the statement of equilibrium condition: the sum of forces inside Ω has to balance the force f_i acting on the elastic body (the internal properties of the body and so the reactions to applied forces are completely described by its elastic constants).

Two types of boundary conditions are applied. At the Neumann boundaries we may fix the values of g_i to simulate a traction on that boundary or set $g_i = 0$ to have free-surface-like boundary. At the Diriclet boundaries a given prescribed displacement can be set. Only simple problems allow for analytical solution of the boundary value problem in equations 2.1. In our case, in order to calculate the elastic field in complex elastic bodies, such as nanometric 3D islands, no analytical solutions are available. We use finite element method (FEM) to numerically solve the problem. FEM starts with the discretization of the elastic bodies into a set of points which define a 3D (or two dimensional) grid to fill all the body. This set of points (called "nodes"), together with the elementary elements which have nodes as vertices, is called mesh. in our calculation we always use the proper tetrahedral (or triangular in the bidimensional calculation) mesh to fill the body. Once the mesh is generated,a key point is the set up of the proper boundary and internal condition. In our calculation there are not external forces acting on the island, so $f_i = 0$. The island itself is the origin of the stress in the system. As we will see in the next session,it is possible to mimic the mismatch between $Si_{1-X}Ge_X$ island and Si substrate treating the island as an inclusion in a not deformed matrix (substrate). We impose to the bottom of

[1] see App. A for a brief introdution of linear elasticity theory

the simulation box the Diriclet condition ($u_i = 0$) letting free the other exposed surfaces. With this condition the boundary value problem becomes:

$$\begin{cases} -\sum_{j=1}^{3} \frac{\partial}{\partial x_j}\sigma_{ij}(u) = 0 & \text{inside} \quad \Omega \\ \sum_{j=1}^{3} \sigma_{ij}(u) n_j = 0 & \text{on} \quad \Gamma_N \\ u_i = 0 & \text{on} \quad \Gamma_D \end{cases} \tag{2.2}$$

Solving Eq. 2.2 is possible to calculate the displacement field u at each node, and the elastic properties of the system (stress, strain and elastic energy). The results showed in this thesis are obtained using the commercial FEM code Comosol Multiphysics.

2.2.1 Mimicking lattice mismatch between islands and substrate

Lattice mismatch between Germanium and Silicon is the origin of the stress field in heteroepitaxial structures. Using FEM or analytical calculation one of the main point is how to mimic the mismatch in a continuum framework. Eshelby's theory of inclusion can be a useful tool and it presented in the following. Suppose we have a media where there is a region Ω completely embedded in it, which undergoes a permanent, not elastic deformation. The material inside Ω is called an *inclusion*, while the media surrounding it is generally called *matrix*. If we could pick up the entire Ω region and take it away from the media, it would experience a deformation which could restore the zero-stress condition, that is, it would assume a uniform strain ϵ^*_{ij} that is known as *eigenstrain*.

In general, we say that there is a condition of eigenstrain ϵ^* in a certain region of the body if the stress vanishes as $\epsilon = \epsilon^*$. As a consequence, the eigenstrain tensor can be defined in the following way:

$$\sigma_{ij} = \mathcal{C}_{ijkl} \left(\epsilon_{ij} - \epsilon^*_{ij}\right) . \tag{2.3}$$

The previous relation *defines* the eigenstrain ϵ^* as the value of the strain field at which the stress field is zero. In point of fact,

$$\epsilon_{kl} = \epsilon^*_{kl} \quad \Rightarrow \quad \sigma_{ij} = 0 . \tag{2.4}$$

Furthermore, the *eigenstress* is defined as

$$\sigma^*_{ij} = \mathcal{C}_{ijkl}\, \epsilon^*_{ij} . \tag{2.5}$$

However, since the inclusion is surrounded by the matrix, it is not able to reach the state of eigenstrain, i.e. the condition of zero stress. Instead, both the matrix and the inclusion will deform in order to minimize the elastic energy: the *Eshelby's problem of inclusion* consists indeed in the problem of finding the displacement field due to the condition of eigenstrain in the entire space. This is exactly our problem. We can assume that the Ge island (or more generally the epilayer) determines a *permanent condition of strain* in the Si substrate due to the mismatch between the lattice parameters of the two species. The specific expression of such a permanent deformation must take into account the the microscopic differences between the Si and Ge crystal structures. It is well-known that both have diamond structure, with a lattice mismatch given by

$$\epsilon_m = \frac{a_{\mathrm{Ge}} - a_{\mathrm{Si}}}{a_{\mathrm{Ge}}} . \tag{2.6}$$

In case of pure Ge value of such a parameter is found to be

$$\epsilon_m \approx 0.0399 \ . \tag{2.7}$$

The fact that the materials have the same crystalline structure implies that, microscopically, the unique condition of stress must is by the lattice parameter mismatch. As a consequence, one can assume a simple eigenstrain,

$$\epsilon^*_{ij} = \epsilon_m \delta_{ij} \ , \tag{2.8}$$

According to the eigenstrain principle, if we were able to take the island away from the substrate, it would undergo an elastic deformation that would recover its natural lattice parameter.

Evidently, the problem of finding the solving the elastic problem of an heteroepitaxial island really resembles the one of an inclusion, since the main idea is that some SiGe alloy is forced into a Si matrix, thus leading to a condition of stress because of the lattice parameter mismatch ϵ_m.

2.3 Elastic relaxation in islands with realistic shape

The formation of 3D stable islands is possible because it allows for a partial relaxation of its lattice parameter with respect to a flat film. Two main mechanisms are responsible of such relaxation: free surface relaxation and and substrate deformation [59]. The in-plane compression can be reduced by exploiting all of the free surfaces inclined with respect to the (001) interface. In fact, all the forces acting along the free surface normal vanish, being the material free to change its effective lattice parameter in that direction. The force components parallel to the free surfaces, on the other hand, can be reduced by involving a deformation of the substrate. It is important to notice that while the first mechanism allows for an effective reduction of the elastic energy, the second one redistribute the deformation between the island and the substrate. To analyze quantitavely the effects of elastic relaxation described above FEM calculations have to be performed, choosing the proper condition to impose at Eq. 2.2, and imposing Eshelby eigenstrain condition in the island.

2.3.1 Island geometries and boundary conditions

Before performing any calculation, it is necessary to define precisely the domain Ω, that is to properly construct the geometry of island and substrate in which elastic relaxation has to be studied. Furthermore, it is necessary to define what kind of boundary conditions have to be imposed and how to manage properly the substrate on which the island relies. We modeled island geometries mimicking the real shapes experimentally observed.

105 pyramid (ρ=0.1), dome (ρ=0.2) and barn (ρ=0.3) shaped islands are shown in Fig. 2.2 according to their crystallographic orientation.

The substrate, indeed, is modeled by a box with edges L_x, L_y and L_z. After contacting the bottom of the island with the top of the substrate, we fixed the displacement at the bottom and at the sidewalls of the substrate, applying Diriclet boundary conditions. Because of that we chose L_x, L_y and L_z large enough to avoid interactions between the stress field of the system and the fixed boundaries. We have performed a simple check of the correct choice of L_x, L_y and L_z by evaluating the elastic energy of the system while

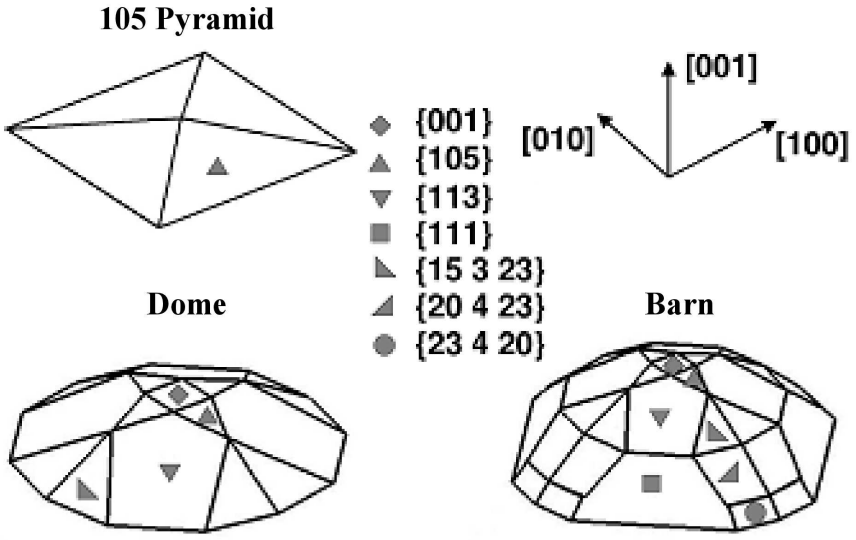

FIGURE 2.2: Island geometries used in FEM calculations. Geometries are modeled to fit the experimental observations, free surfaces are marked in order to distinguish among different facet inclinations.

the length in the different directions is varied. On the contrary, free surface conditions are imposed at the top of the substrate and at the exposed surfaces of the island.

2.3.2 Eigenstrain condition in Ge island

Before solving the problem we need to assign the internal stress in order to simulate the lattice mismatch between islands and substrate according to Eq. 2.8:

$$\begin{cases} \sigma_{ij} = \mathcal{C}_{ijkl}\,\epsilon_m & \text{island} \\ \sigma_{ij} = 0 & \text{substrate} \end{cases} \tag{2.9}$$

As already highlighted in section 2.2.1, the epilayer acts as stressor in the system.

2.3.3 Detailed elastic field in Ge islands by FEM

Once properly defined the initial condition it is possible to compute the elastic field in the structure. In order to give a quantitative estimation of the relative redistribution of the elastic energy due to the two relaxation mechanism described above mechanisms, we start our analysis with the results of a FEM calculation performed on a {105} pyramid. In Fig. 2.3, Panels (a) and (b) show a gray-scale map of the elastic energy density in the island and in the substrate, respectively. The elastic energy is stored in both the island and the substrate; in particular it can be noticed that the upper part of the island has lower energy density with respect to the wetting layer condition (pseudomorphically distorted and used as reference, $-1.3eV/nm^3$) via free surface relaxation and substrate loading, while the substrate has higher elastic energy with respect to the initial condition (no stress is assigned to the substrate, see Eq. 2.9). It is important to point out that, beyond surfaces, also the lateral edges joining adjacent island facets act as further centers of deformation relieve. Indeed, in this region each surface atom can exploit enhanced degrees of freedom to locally adjust distances.

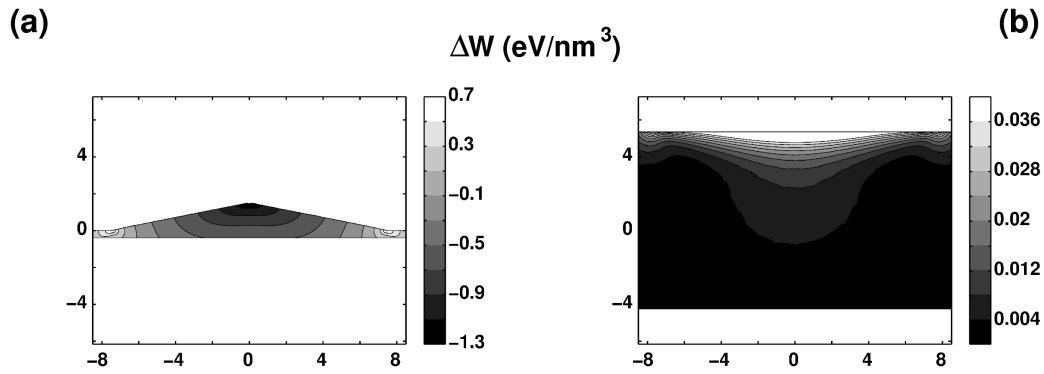

FIGURE 2.3: Elastic-energy-density plot for a vertical scan crossing through the island apex, for a 105 pyramid. In (a) the elastic energy is referred to the wetting-layer one. Negative values correspond to higher relaxation; (b) elastic energy density stored in the Si substrate.

TABLE 2.1: Reference of the experimental elastic constants for Si and Ge and the correspondent values computed with the Tersoff potential.

(GPa)	Si		Ge	
	Exp.	Tersoff	Exp.	Tersoff
C_{11}	167.5	142.6	131.5	138.6
C_{12}	65.0	75.5	49.4	44.5
C_{44}	80.1	69.0	68.4	66.8

2.3.4 Comparison between FEM and atomistic calculations

For sake of robust and reliable FEM calculations, it is worth starting with a direct comparison with atomistic calculations. A 3D {105} pyramid was simulated with an atomistic code to get the relaxed atom configuration, using the Tersoff interatomic potential [50]. For a significant comparison, elastic constants obtained by using this potential (see Tab. 2.1) were implemented in the FEM code and used to simulate the same pyramid. Since a comparison of the elastic strain with color map between a FEM and an atomistic is not sufficient to declare the agreement of the two methods, a comparison of the elastic field on localized positions was made. In particular, data were extracted from both simulations for the ε_{xx} strain tensor component along a vertical line passing through the island apex. The comparison is made in Fig. 2.4 where it can be noticed the nice overlap between FEM and atomistic solution of the same problem. At high z, fluctuations in the atomistic solution are ascribed to step effects due to the local geometry of the pyramid at the atomic scale.

2.3.5 Elastic relaxation from {105} pyramid to barn

Elastic relaxation guarantees a global reduction of the elastic energy, establishing a non uniform elastic field in the island and in the substrate. In the following we will describe such field in its general features and in the island-shape dependent characteristics. Figures 2.5, 2.6, 2.7 depict the ε_{xx}, ε_{zz}, ε_{xz} strain tensor components for a vertical cross section inside each island, for pure Ge island and the Si substrate lattice obtained via FEM calculations. In addition, a horizontal cross cut at the island base is exploited to map the xy and in-plane

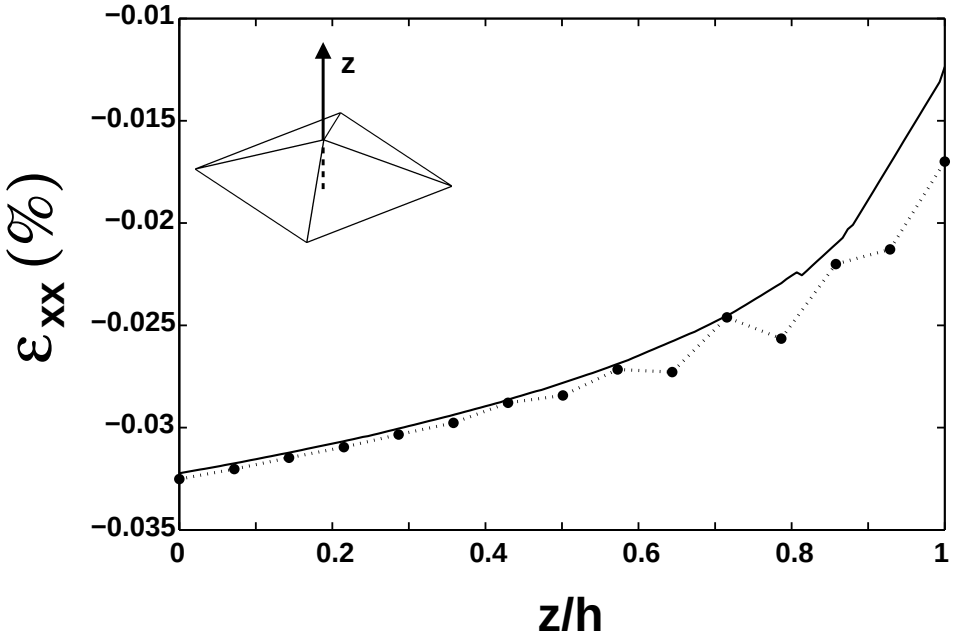

FIGURE 2.4: Comparison of FEM and atomistic calculation of deformation field inside a {105} pyramid. Data are taken along a vertical line passing through the island apex, as illustrated in the inset. Here h is the total island height. Excellent agreement is obtained by comparing FEM (solid line) and atomistic calculation (dashed line).

(i.e. $\frac{1}{2}(\varepsilon_{xx} + \varepsilon_{yy})$) strain components. Each figure is focused upon a shape:{105} pyramid, dome, barn, respectively, as summarized in Fig. 2.2.

There are common features of the ε_{xx} component in the three shapes. Two regions are clearly visible, located at the island corners and in the substrate too, where the lattice is highly compressed. This compression is higher than the misfit ε_m, so that this effect cannot be only due to the pseudomorphic arrangement of the Ge lattice on the Si substrate. In fact, this compression is one of the fingerprints of the elastic energy redistribution previously mentioned. Underneath the island, on the other hand, it is visible a region where the Si lattice parameter is expanded with respect to its native lattice parameter. This is another effect of the energy redistribution due to the presence of the island. Notice that this deformation is absent in the case of a flat film (in this case $\varepsilon_{xx} = \varepsilon_m$), so that the elastic energy does not propagate inside the substrate and is instead confined exactly at the Ge epilayer. Inside the island, from the bottom to top, the horizontal compression decreases. This is the effect of surface relaxation, which continues to relieve elastic energy as soon as the island top is reached. Analyzing The map of the ε_{xx} component for different shapes it is clear that island edges are more compressed as the aspect ratio increases. The maps show that the top edges (convex) are centers of relaxation, with respect to the high compression located at the bottom edges (concave). By increasing the aspect ratio, the strain value reached at the island top decreases, from -3% for a {105} pyramid to almost zero for barn. This trend represents the net effect of surface relaxation, which is more effective in high-aspect ratio islands since they have a surface-to-volume ratio larger than shallow, {105} pyramids. The dome and barn shape display the most uniform strain map: we ascribe this finding to the presence of the multiple facets characterizing these shapes.

The ε_{zz} component is directly linked to the ε_{xx} (or ε_{yy}) component, through the analytical

relation $\varepsilon_{zz} = -\frac{\nu}{1-\nu}(\varepsilon_{xx} + \varepsilon_{yy})$ (ν is the Poisson ratio), that is exact for a flat film and approximated for an island. The sign of this formula points out that once the ε_{xx} and ε_{yy} components are negative, the ε_{zz} is positive and vice versa. This means, as can be directly seen from the figures 2.5, 2.6 and 2.7 , that the centers of local horizontal compression correspond to a tensile deformation in the z direction. For the same reason, the Si lattice, if expanded in the x,y directions, is compressed in the z direction. Focusing on shapes, It can be seen that the strain field inside {105} pyramids is quite non-uniform, while the rounded shape of domes and barn produces a more uniform strain field in this case too.
The off-diagonal strain tensor components quantify the lattice bending. For instance, the ε_{xz} component gives the local lattice bending in the (x,z) plane, as well as the xy component gives the torsion in the (x,y) horizontal plane. A careful analysis of these components reveals that the elastic field is symmetric in sign with respect to the island center: at every point lattice with a given strain value, there exists another point with the same value and opposite sign meaning that the curvature inside the island follows the symmetry of the island shape. The ε_{xz} maps show that with increasing aspect ratio, two symmetrical lobes located at the island bottom edges become more and more defined, also increased in absolute value.
Finally, the in-plane strain component displays, by definition, symmetry with respect to the island center. It shows how the deformation propagates inside the inner island regions, far from surfaces. It is a common feature that the in-plane elastic field decreases moving from the island boundaries to its center; this is another fingerprint of edges as local sites of high deformation.
The in-plane strain component shows that the deformation is always decreasing moving from the island boundary to the center. The shape of the contour lines always resembles the shape of the corresponding boundary: squares in square-base pyramids and circular in domes and barns.
The ε_{xy} component shows a very non-uniform strain distribution, being always larger at the corners than at the island center. Four lobes are present: their shape and size evolve moving towards steeper islands. While they are small and very localized in {105} pyramids, these lobes are more spread – and correspond to higher values – in steeper islands.

2.3.6 Self-similarity of the elastic field

The last important point about elastic field in island is highlighted in the following paragraphs. Given a 3D quantum dot placed on the substrate, it is worth questioning wheter the elastic field changes while the island grows. Three FEM simulations were carried out with a dome where the lateral size is doubled and doubled again. The comparison of the elastic field, reported in Fig. 2.8, demonstrates that *the elastic field is exactly the same.* No changes can be appreciated while varying the island size. This effect is called "self-similarity" — or "scale-invariance" — of the elastic field and can be explained as follows. It has been seen in the previous Section that features like the facet inclination angle are key to influence the elastic field in the island. By varying the size, but not the shape, geometrical angles are preserved so that there are actually no reasons why the elastic field should change by varying the island size. In conclusion, one could even not be restricted to explicitly mention the lateral size of the island, since it does not affect the elastic field inside the shape. In conclusion, elastic field is a function of island shape, and not of island size. Analytic approaches demonstrated the ability to capture the essence of this effect as well [75].

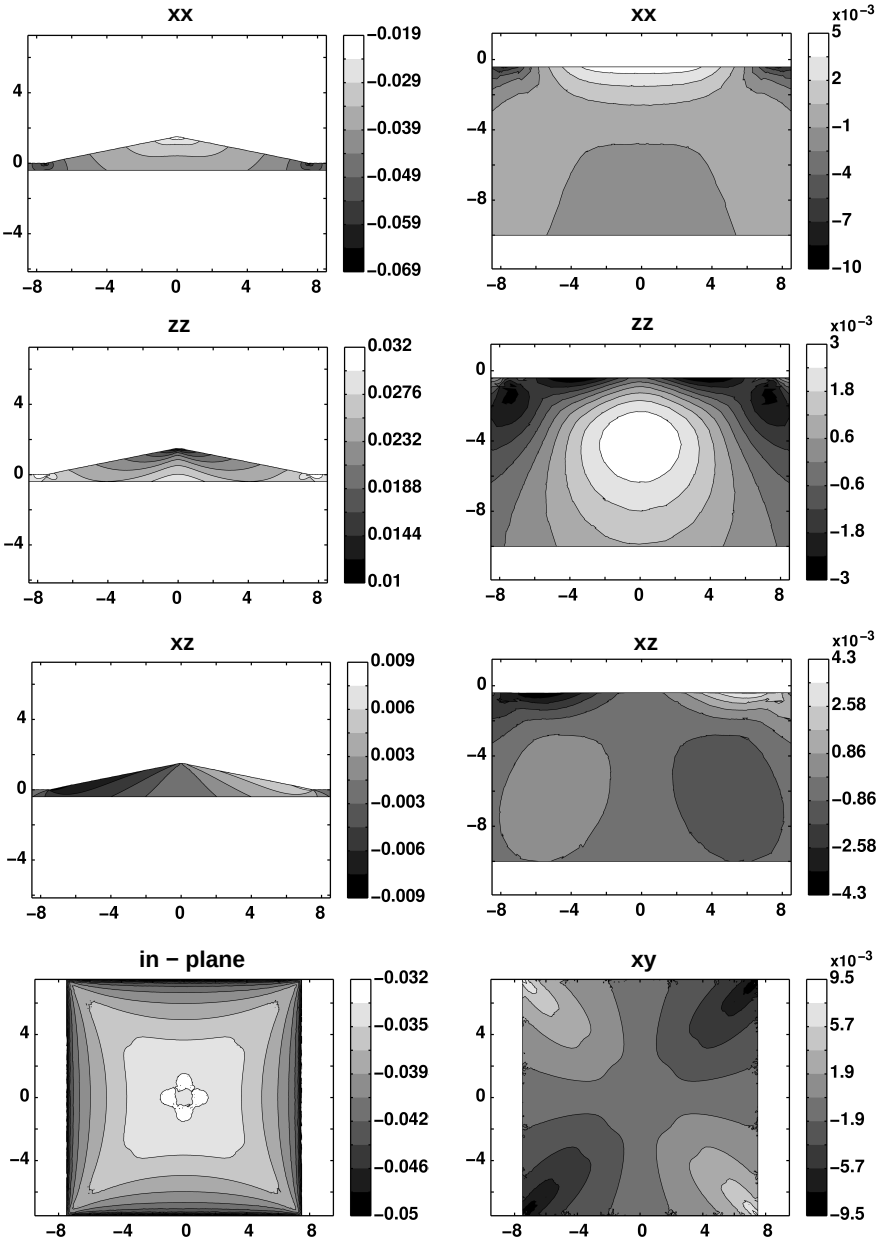

FIGURE 2.5: Maps and contour lines of the independent strain tensor components calculated for a full {105} pyramid by FEM. Anisotropic elastic constants are taken into account.

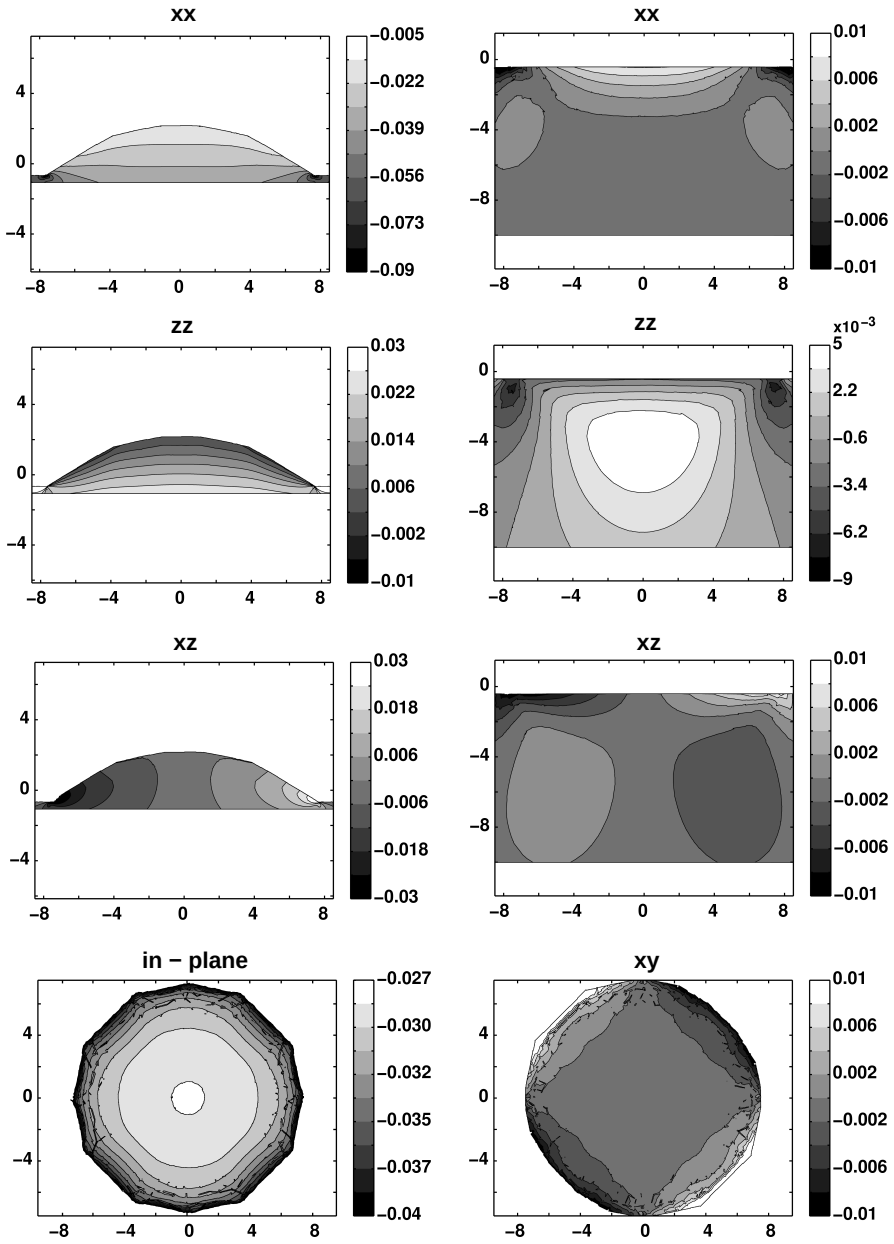

FIGURE 2.6: Maps and contour lines of the independent strain tensor components calculated for a dome by FEM. Anisotropic elastic constants are taken into account.

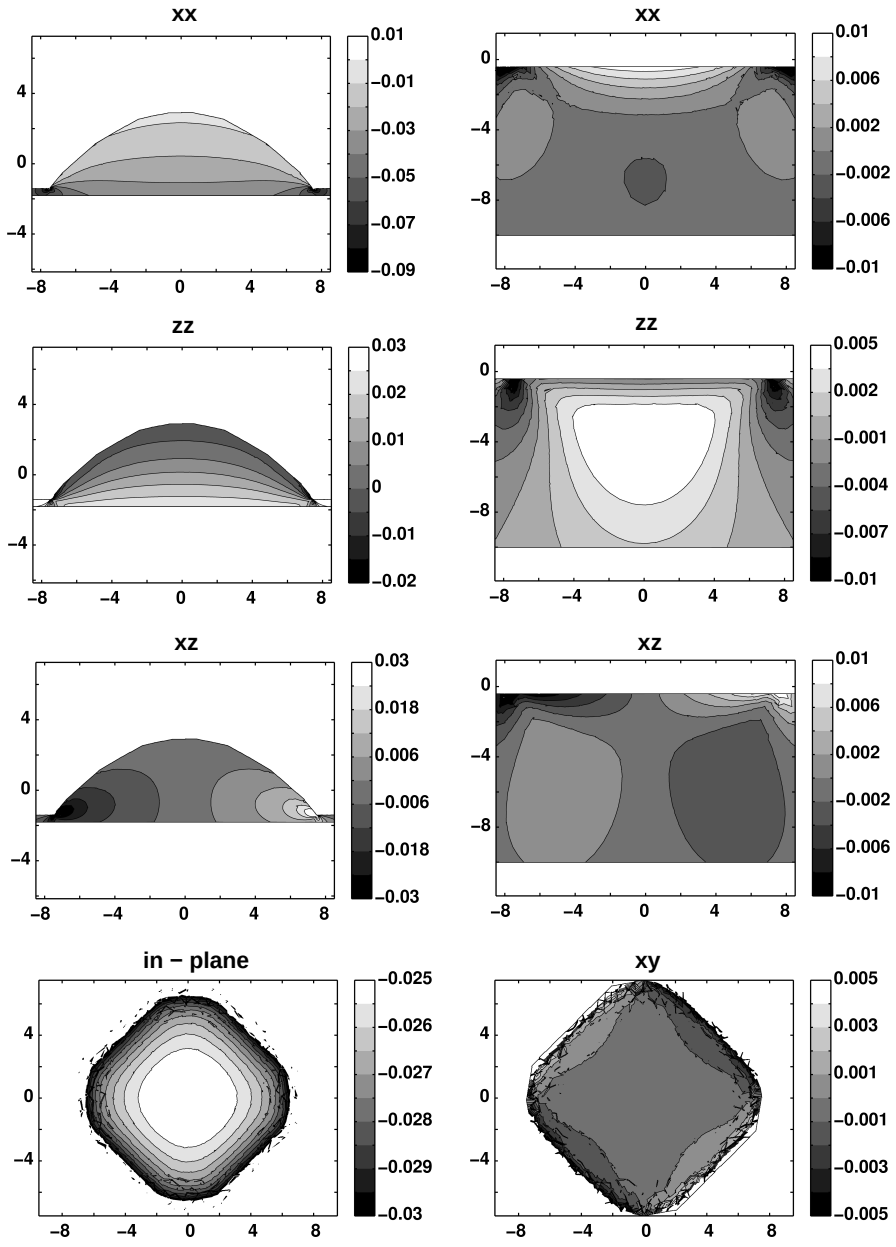

FIGURE 2.7: Maps and contour lines of the independent strain tensor components calculated for a barn by FEM. Anisotropic elastic constants are taken into account.

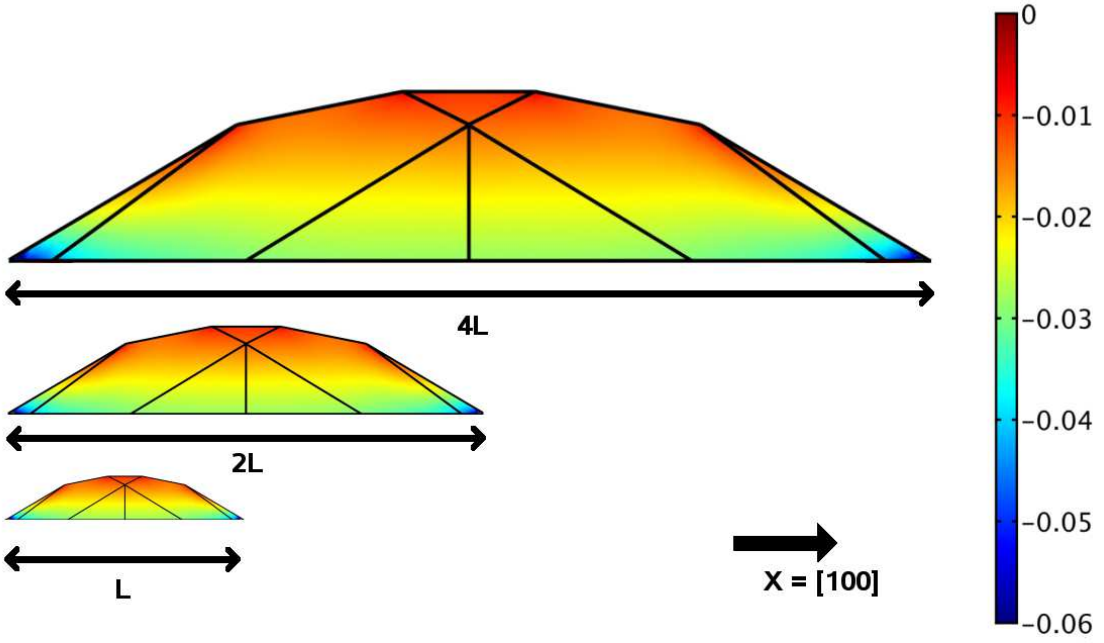

FIGURE 2.8: Self-similarity of the elastic field, showed for a dome-shaped island. When an island of size L is doubled and doubled again, the behavior of the elastic field is unaltered (the color map of the ε_{xx} strain component is shown).

It is worth mentioning that the self-similarity statement, in any case, is strictly true only in absence of a wetting layer. Since its thickness is always 3 ML, independently of the island size, its weight over the whole elastic body (island+wetting layer+substrate) changes as the island volume changes.

2.4 Alloying of the islands due to intermixing phenomenon

The mechanisms described in previous sections do not allow for a complete relaxation of the elastic energy in the islands, the bottom edges remain strongly loaded with stress (Sec. 2.3.5). From different set of experiments, and with the help of theory [76, 43], it emerged that the actual concentration profile in 3D islands depends on the growth conditions and it is determined by the complex and not yet fully understood cooperation between elastic-energy relaxation, frozen kinetics [2], and entropy maximization (enthalpy of mixing has been shown to be rather negligible [76, 64]). Since the growth-parameter space cannot be sampled at will in experiments, a promising way for understanding the role played by each of such phenomena is surely given by directly relating the experimentally-derived concentration profile with theoretical simulations performed under conditions tuned to emphasize the different contributions. With this goal in mind that we developed a very fast method for determining the concentration profile which minimizes the elastic energy in realistically shaped 3D heteroepitaxial islands for a given average concentration value. Beside a very nice model allowing for an analytical treatment of the problem [78] (limited however, to the description of islands formed at the very first stages of growth), a very direct method

[2] Bulk diffusion in Si/Ge systems is usually considered to be totally frozen at typical dots growth temperatures. Very recently, however, a bulk diffusion length $\sim$ 1nm, was estimated at a non-dramatically high temperature $T = 750^{\circ}$C [77].

for finding the optimal Ge distribution is given by exploiting atomic-scale Monte Carlo (MC) simulations, the system energy in each configuration being computed through classical empirical potentials [79, 80, 81, 82]. Minimization can be achieved by iterating a procedure consisting in chemical-species random exchanges, energy optimization, and acceptance based on the Boltzmann statistical weight [79]. The drawback of the atomistic MC approach is given by the computational cost. The volume of typical experimental islands can easily exceed 10^5 nm^3 (particularly so, if alloying is pronounced), making an atomistic treatment impossible. If it is true that the self-similar behavior of the deformation field allows one to work at a reduced scale [83], two main problems might be encountered. First, the effective number of bulk-like atoms could become comparable with the surface ones, making surface effects too strong. Secondly, the complex, multifaceted geometry of realistic islands like domes [84, 29] or barns [40] works against excessive size shrinking since each facet must be created with a physically meaningful extension in order to avoid artifacts (such as the overlap between the strain field coming from edges and/or vertex). In practice, this means working with islands of at least 10^4–10^5 atoms, making the convergence procedure extremely long. Motivated by this limitation, even in this case, we have designed a rather simple and very fast way for achieving elastic-energy minimization within a Finite Element Method (FEM) framework. While in this thesis we shall provide an application to Ge/Si(001), a system for which several experiments analyzing alloying have been reported [85, 44, 86, 87, 88, 47, 64], it is important to emphasize that the physics involved is rather general (see the interesting discussion in [89]), and applies also, for example, to the popular III-V systems [90]. In InAs/GaAs films, moreover, the larger lattice mismatch is expected to provide a stronger driving force for non-homogeneous alloying, so that all the effects here below discussed should be even stronger.

2.4.1 Monte Carlo-FEM approach

In order to treat non-uniform distributions we propose a particular procedure which has the appealing feature of exploiting only typical operations performed by any FEM code, allowing for a simple implementation. Here we recall that the core of a FEM calculation consists in dividing the space into elements (typically, tetrahedrons for 3D problems), and by evaluating any function $f(x, y, z)$ considering an interpolation based solely on the values of the function at the nodes of the element containing (x, y, z) (see, e.g., [74]). Here, we shall make use of two different meshes at the same time. A first one, called *concentration mesh*, and made by n nodes located at (x_i, y_i, z_i), $i = 1, \ldots, n$, is used to define a non-uniform concentration profile. Values are assigned at the nodes ($c_i = c(x_i, y_i, z_i)$, $i = 1, \ldots, n$), while a linear interpolation scheme is used for evaluating the concentration at any other point, including the nodes (X_j, Y_j, Z_j) ($j = 1, \ldots, N, N \gg n$) of a second, much finer grid (called simply *FEM grid* in the following), used for finding the elastic body equilibrium condition. For the systems considered in this work, concentration meshes with $n \sim 400$ turned out to be sufficient to accurately describe the concentration profiles in 3D islands (in practice, only 1/8 of the n points were used, see Section 2.4.2).

Once the initial strain condition is assigned, the minimization of the elastic energy proceeds by a MC iterative procedure. Two vertices of the concentration grid are chosen randomly and their assigned values are randomly changed so that the overall composition of the island remains the same. This constrain can be rather easily fulfilled for linear interpolation leading only to a pre-calculation of necessary weights. The new elastic energy

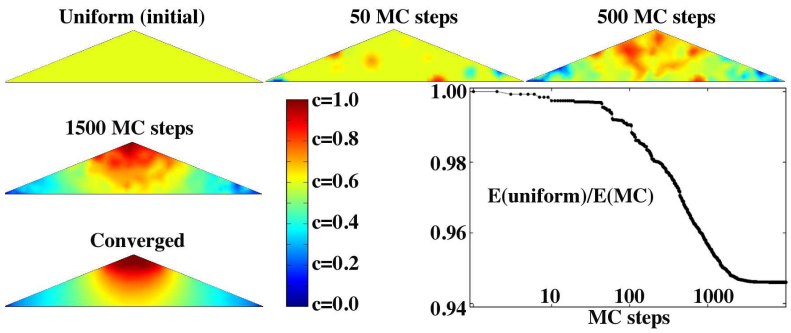

FIGURE 2.9: Evolution of the concentration profile for a two-dimensional ridge, with average Ge concentration $c = 0.6$. After $\sim$ 3000 Monte Carlo steps, the energy of the system, plotted in the bottom right panel in the form of ratio between the actual energy and the one of the uniform distribution, reaches convergence.

is then calculated by a full FEM calculation, using linear elastic theory. While to this goal we used the commercial Comsol Multiphysics code, the method can be obviously implemented with any FEM solver. Moves (i.e., concentration exchanges) are accepted if the energy is lowered and rejected otherwise. This procedure is repeated until the concentration profile does not change anymore. It is important to emphasize that at each MC step a new solution of the elastic problem is found, so that the calculation is fully self-consistent: changes in the elastic field accompanying Si/Ge redistribution are correctly described. In order to speed-up convergence, we used a guiding function to bias moves. The bias function is built on the fly, and assigns different statistical weights at the concentration values using information on all previously accepted moves.

A schematic representation of the system evolution during our MC procedure is reported in Fig. 2.9 for a two-dimensional case, for which illustration of the system evolution is particularly simple. In the reported example, the Ge island (of height to base aspect ratio 0.2) is actually a ridge, infinitely extended in one dimension. The Si substrate is not reported in this figure and in the following ones. The concentration grid was made of 109 points, and the average c was set to 0.6. Experimental Ge and Si lattice constants were used [5]. In the figure, a color map is used to highlight different Ge contents. After $\sim$ 1000 steps the system starts converging toward the final situation, where Ge accumulates at the top of the island, while Si tends to fill the lower edge region. Notice that the final distribution in Fig. 2.9 is nicely symmetric, although no constraints were imposed. Indeed, while first validating our approach, we found out that checking for artificial lack of symmetry was sometimes more indicative than simply looking at the elastic energy convergence. After several trials runs (both in 2D and 3D) convinced us that our implementation was correct, however, we started exploiting symmetry to speed-up convergence.

2.4.2 MC-FEM in realistic 3D islands

Let us now consider more realistic, 3D applications. We have applied our MC-FEM procedure to the three main shapes observed in Ge/Si(001) molecular beam epitaxy experiments [40], already described Section 2.3.5, i.e. (105) pyramids multifaceted domes and multifaceted barns. Ge and Si elastic anisotropy was taken into account in the calculations, even

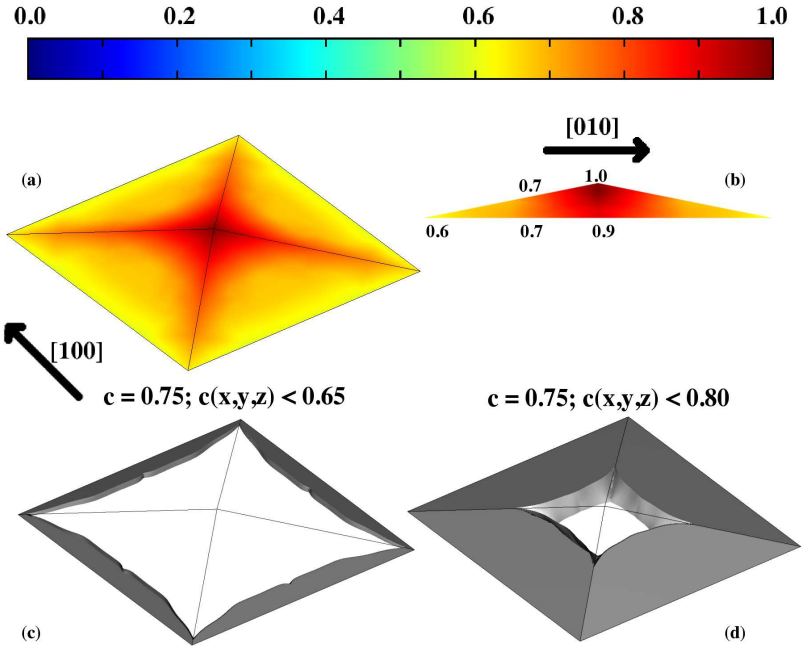

FIGURE 2.10: Concentration profiles for a (105) pyramid. The average Ge content is fixed to $c = 0.75$. (a) 3D view of the distribution along the island facets. (b) Cross-sectional view. (c) 3D distribution of material with a Ge concentration below 0.65 (selective-etching profile). (d) 3D distribution of material with a Ge concentration below 0.80.

if we verified that qualitatively similar results are obtained also in the isotropic case. Pyramids, domes and barns can be easily divided into 8 equivalent sub-regions. Since the 3D FEM solution of the elastic problem is computationally rather demanding, considering that it is required at each MC step, exploiting symmetry is rather important for accelerating convergence. We therefore defined our concentration mesh only in the subregions, propagating every attempted concentration exchange in the rest of the island before calling the FEM solver. In this way, the single elastic-energy calculation is not faster, but the number of MC iterations is reduced since fewer concentration mesh points are needed to reach a satisfactory description of the atomic distribution in the subregions. A further advantage is given by the fact that the solution displays the correct symmetry at each step, so that the portion of the sampled concentration space is reduced.

Let us start the analysis of our results by looking at the behavior displayed by (105) pyramids. Simulations were performed using an average Ge concentration value $c = 0.75$, in order to reproduce the experimental estimate reported in [40]. In Fig. 2.10, panels a and b, we report the final Ge concentration in the island using a 3D perspective view (panel a) showing $c(x, y, z)$ at the island facets, and a cross-sectional 2D view, obtained by cutting the island along the [010] direction (panel b). Color maps are used to distinguish different concentrations in the on-line version. A few representative values are also superimposed in panel b, in order to facilitate the reader of a black and white printed version. Overall, there is a spread in concentration of ~ 0.35 between Ge-rich and Ge-poor regions, the latter being located close to the island bottom edges. In panels c and d, instead, we plot only the subregions occupied by less than 65% (c) and 80% (d) of Ge atoms. The analysis of

the corresponding isocompositional surfaces is interesting for two main reasons. If from one side they give a good idea of the 3D Ge distribution in the island interior, the 0.65 case also allows for a direct comparison with the selective-etching experiments of Ref.[40], where Ge-rich (above 0.65) regions are eliminated by a suitable etchant. From panel c, it is evident that the concentration profile minimizing the elastic energy in a (105) pyramid of average $c = 0.75$ displays almost entirely regions where the Ge content is above 0.65. Only at the very bottom of the island, and along the base edges, material is therefore predicted to resist the etching action. Comparing our results with the ones of Ref.[40], it is evident that the agreement is only qualitative: in both cases it is confirmed that Si-rich regions are located far from the top of the islands, but in the experiments the four corners appear more rich in Si with respect to the center of the edges, i.e. the reverse of the behavior found in panel c. Notice that, as stressed in Section 2.4, differences between the concentration profile minimizing the elastic energy and the real one must in general be expected, since entropic and kinetic effects are not taken into account. With this respect, we find the comparison between our results and the experimental ones particularly useful in evidencing that the actual profiles do not allow for the maximum possible strain relaxation. A further observation can be made. The main difference between our results and the experimental ones does not seem to stem in different degrees of deviation from a uniform distribution, but only in the actual location of the Si-richer regions. With this respect, we believe that the observed difference should not be attributed to entropic effects. Kinetic effects, as suggested in Ref.[40] (see also [48]), could explain the observed distribution. The 0.80 isocompositional surface (panel d), although not corresponding directly to experimental etching profiles, provides further interesting information on Ge distribution, showing that a Ge-rich region, starting from the top of the island (where pure Ge is found), extends in the center of the island reaching the substrate. A similar behavior is found also for dome islands, for which experimental evidence of this hole was reported. Results for domes are reported in Fig. 2.11. In this case, always trying to reproduce experimentally reported values [40, 91], we considered an average Ge content $c = 0.6$. Panels a,b, and c of Fig. 2.11 display the same kind of results shown in Fig. 2.10 for pyramids. Notice that in this case, differences in concentration exceeding 0.9 are reported between the top and the base of the island. Evidently, the strong compression at the edges, induced by the higher aspect ratio [92], strongly attracts Si atoms which better accommodate in a low lattice-parameter environment. The simulated etching profile (panel c) confirms this observation, showing that removing material exceeding 0.65 of Ge induces a clear hole in the center of the island. Looking at the composition map obtained by atomistic MC at $T = 8$K in Ref.[79], one can infer an analogous behavior, thus providing a rather convincing proof of the reliability of our continuum-theory based approach to non-uniform concentration distribution in heteroepitaxial islands.

The comparison between our results for domes and the corresponding experimental results of Ref.[40] shows an agreement much more pronounced with respect to the pyramidal-island case, once it is taken into account that convolution effects produce a rounding effect in the images of [40], and that in our figures proportions in the x,y, and z directions are maintained. Not only the presence of the central hole is confirmed experimentally, but also the slight tendency towards maximal accumulation along the [110] directions seems to be in agreement. Experiments in [40] were repeated by raising the growth temperature, therefore enhancing the Si concentration in the island, in order to check possible variations

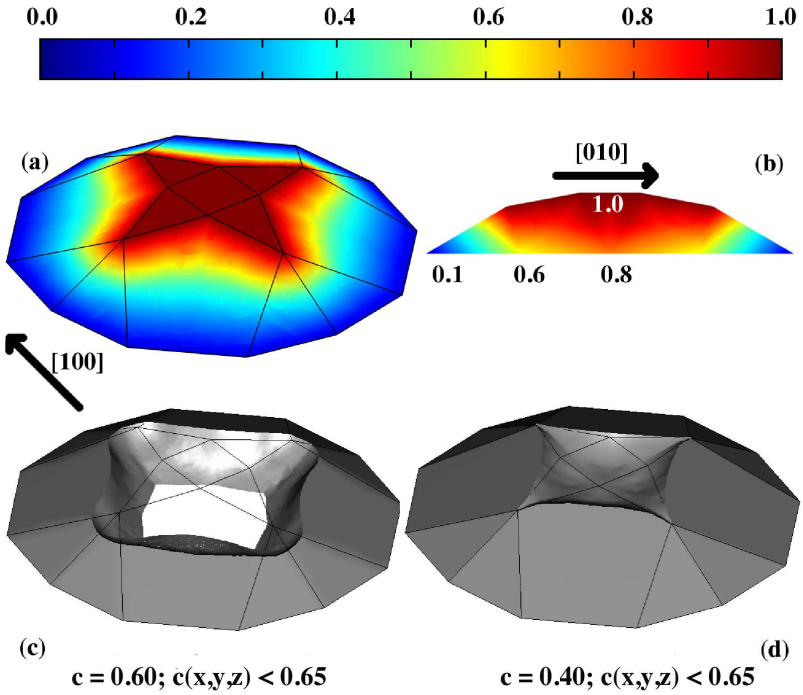

FIGURE 2.11: Concentration profiles for a typical dome-shaped island. (a) 3D view of the distribution along the island facets for an average Ge content $c = 0.60$. (b) Corresponding cross-sectional view ($c = 0.60$). (c) 3D distribution of material with a Ge concentration below 0.65 (selective-etching profile), always for $c = 0.60$. (d) As in in panel c, but for $c = 0.40$.

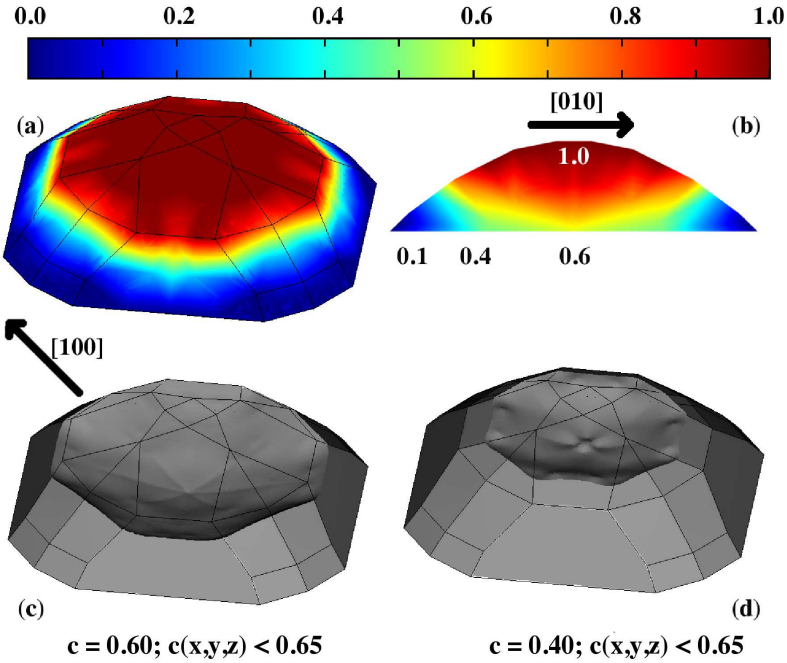

FIGURE 2.12: Concentration profiles for a typical barn-shaped island. (a) 3D view of the distribution along the island facets for an average Ge content $c = 0.60$. (b) Corresponding cross-sectional view ($c = 0.60$). (c) 3D distribution of material with a Ge concentration below 0.65 (selective-etching profile), always for $c = 0.60$. (d) As in in panel c, but for $c = 0.40$.

in the etching profile. The higher Si content, indeed, was shown to qualitatively change the morphology of the material resisting the etching action which no longer displayed the central depleted zone. In order to check for reported change in behavior, we have run a further simulation for $c = 0.4$, obtaining the result displayed in Fig. 2.11d. As in the experiments, the hole disappeared, leaving only a slight depression, possibly not visible in experiments due to the above mentioned convolution effects.

For sake of completeness, we have also investigate the behavior of barn-shaped islands, simulated under the exact same conditions ($c = 0.6$ and $c = 0.4$) considered for domes. From our results, it is quite evident that by raising the island aspect ratio, the tendency towards segregating Si at the island base gets stronger. However, the concentration profile now looks more regular, as a direct consequence of the different geometry: isoconcentration lines are more rounded with respect to the dome case, as it appears clearly from both the 3D (Fig. 2.12a) and the cross-cut images (panel b). Also the etching profile (panel c) looks different, the $c = 0.6$ result for the barn resembling the $c = 0.4$ case for the dome (depression, not hole). Finally, for $c = 0.4$, we predict etching to cause a simple and moderate flattening of the very top of the island.

So far we have focused our attention on the concentration profiles within the islands. Let us now look at the influence of the non-uniform concentration profiles on the elastic energy distribution. Since we have verified that a qualitatively similar behavior is displayed

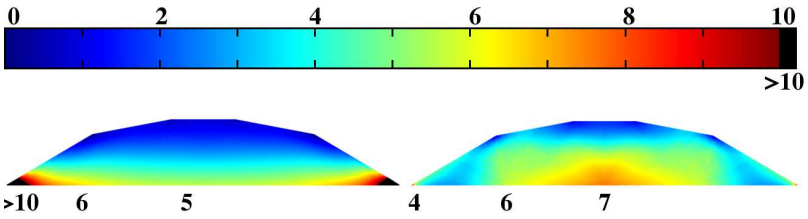

FIGURE 2.13: Left panel: elastic-energy distribution for a dome-shaped island with a uniform Ge distribution, and $c = 0.6$. Right panel: elastic-energy distribution for the Ge concentration profile, illustrated in Fig. 2.11, panels a, b, and c, minimizing the elastic energy. The cross-sectional view is as in Fig. 2.11b. Energies are reported in meV/atom. For the uniform case, the elastic energy at the island edges strongly exceeds 10 meV/atom. In order to show the main differences between the two cases, however, it was more convenient to display color maps between 0 and 10 meV/atom, representing all points above 10 meV/atom with a uniform black color.

by all three geometries, we shall directly illustrate only the dome case. In Fig. 2.13 elastic-energy maps are presented for $c = 0.6$ in the case of a uniform distribution (panel a) and for the distribution obtained after MC optimization (corresponding to the concentration distribution displayed in Fig. 2.11a,b, and c). Energy is expressed with the usual (for atomistic approaches) meV/atom, meaning that a local atomic distribution of atoms yielding, on average, the concentration $c(x, y, z)$ would have the corresponding elastic energy (per atom). Differences between the uniform and the optimized distributions are rather strong, pointing out the importance of using a self-consistent approach. In the former case (already discussed in several papers, for instance see [92]), the upper portion of the island is almost fully relaxed while at the edges the elastic load is particularly significant. Indeed, upon MC-FEM optimization, it is precisely the strong accumulation at the edges which is relieved. While, obviously, the total energy of the system is decreased (by $\sim 12\%$) in passing from the situation illustrated in Fig. 2.13a to the one of Fig. 2.13b, elastic-energy relaxation at the edges is accompanied by a mild (but well detectable) increase in the central portion of the island, decaying while moving towards its top. Clearly, the common picture of a base-to-top elastic energy relaxation is modified by the non-uniform concentration profile.

2.4.3 Outlook about MC-FEM

When we decided to get involved in the problem of concentration distributions in heteroepitaxial islands our initial goal was to start tackling the problem by providing a fast method [3] able to search for the profile $c_{min} = c(x, y, z)$ minimizing the elastic energy. Being a well defined quantity, independent on the growth conditions and representative of the maximum possible level of strain relaxation (for a given island shape and average composition), we

[3] For an island composed of $\sim 10^4$ atoms, we directly verified that atomistic MC based on typical empirical potentials is ~ 50 slower than MC-FEM in providing the minimum-energy concentration distribution. The computational boost allowed for by MC-FEM is however in many cases much higher. Realistic islands at experimental concentration values are in fact made of more than 10^5 atoms, making the use of atomistic simulations prohibitive. Also if the method is applied at finite temperatures, an application not discussed in this work, the speed-up guaranteed by MC-FEM becomes much larger, due to the need of averaging over multiple independent atomistic simulations.

found c_{min} a quantity of particular interest. We were aware, however, that entropic contributions at experimental growth temperatures were demonstrated by atomistic simulations [79] to be fully dominant on elastic effects, driving perfect intermixing. Notice that also the very low energy values (much lower than k_BT for any T relevant for the experiments) reported in Fig. 2.13 indicate the negligible stability of the 0K c_{min} distribution at finite temperatures. In addition, we were also aware of the limitations of a thermodynamic approach allowing for site exchanges for systems were bulk diffusion is frozen. Therefore, we expected to use c_{min} as a simple starting point to analyze deviations at finite temperatures. The successful comparison between the simulated and the experimental selective-etching profiles, came out unexpected. Interestingly, it looks like elastic energy is (at least roughly) minimized while entropy is not allowed to raise. These results appear in contradiction with the conclusions of [64]. There, the authors estimated the entropy values based on the experimentally determined concentration profiles. The mixing entropy S, multiplied by the growth temperature T and estimated on the basis of the simple relation holding for random alloys, turned out to be much larger than the elastic energy E_{el}, leading to the suggestion that strain release is not a significant driving force. This result puzzled us, since their experimental profiles were qualitatively rather similar to ours: a dominating entropic term should have prevented the formation of the observed highly non-homogeneous Si distribution in the island. To clarify this point, we have applied their same TS estimate to our minimum-energy concentration profiles, also finding that the TS contribution outweighs the elastic one. For instance, for a 60% Ge-rich dome, the average TS at the typical growth temperature of 873K is almost 7 times larger than E_{el}, a value very similar to what reported in [64]. Entropy, however, played no role at all in determining our concentration profile, the only driving force allowed by our MC-FEM procedure being elastic-energy minimization. Obviously, we are not saying that entropy plays no role in the experimental profiles, but simply that E_{el} minimization is indeed important, the comparison between the absolute values of TS and E_{el} being misleading in this sense.

It still remains to be explained how the system is able to approach the minimum-energy configuration given that bulk diffusion is frozen. A model able to predict the whole formation process based on an accurate description of the system kinetics seems to be needed. The most promising attempt so far is probably the one reported in Ref.[43], even if important ingredients, such as kinetics of Si/Ge exchanges at islands facets, are still missing.

3

Dislocations in nanostructures by FEM

The chapter is dedicated to the study of plastic relaxation in heteroepitaxial structure using FEM. At this purpose we developed a straightforward method to handle dislocations in nanostructrures directly in FEM framework. In fact the elastic field of dislocations in nano-object is strongly influenced by the small size of the structure, deeply interacting with free surfaces and interfaces. We show how our novel computational strategy can be applied to the study key properties of heteroepitaxial structures such as the plastic relaxation onset (introduction of the first dislocations) in flat film and, in next chapter, in Ge/Si islands. Furthermore we depict how by proper patterning of the Si (001) substrate it is possible to predict dislocation confinement in a prescribed area of the heteroepitaxial system, opening a viable path for dislocation engineering. For a brief introduction about the concept of dislocation see App. B

3.1 Dislocations in FEM code

Many different strategies have been developed approaching defected structures. Atomistic simulations can be carried out in order to obtain atoms configurations around dislocation lines, core geometries and energies (e.g. Refs. [93, 94, 95, 96, 97]). A long computational time is however required so that, for instance, the simulation of dislocated island, despite the nanometer scale, can be performed only for idealized, prototypical cases (an example will be given in the section 4.1).
An analytical approach is therefore highly desirable. The unavoidable consequent loss in the description of the core regions, when realistic structures are modeled, does not influence the calculation of mechanical properties, because of their small extensions. Classical dislocation theory [98] even if it remains the touchstone of all the tried analytical approaches, fails in managing complex three dimensional structures with multiple surfaces and interfaces. Most of the models proposed in literature are developed considering dislocations described by analytical infinite domain solutions and correction terms (image stresses) tackling surfaces and interfaces interactions, generally approximated by empirical/analytical formulae valid for simple boundary geometries [99]. We provided a continuum based approach exploiting the capability of numerical calculations to handle the interactions between dislocations and

surfaces, as described in the following.
Let us consider first the general case of the calculation of the stress field due to a dislocation segment in a finite structure where no other sources of the elastic field are present.
As we have seen in sec 2.2, classical elasticity theory describes the equilibrium state of a solid in terms of internal stresses $\sigma_{ij}(u)$, as a function of the displacement field u with respect to the initial position, and external applied forces fi. Defining the body as the domain Ω, with boundary $\partial\Omega$, equilibrium equations can be written in a boundary value problem as highlighted in Eq. 2.1. FEM allows the numerical solving of the equations system 2.1 so that assigning the proper conditions it's possible to find the elastic field in any domain (see chapter 2).
We conceived to use the FEM calculation starting from the stress field of a dislocation segment in an infinite body and using the solver to find the solution that satisfy also the finite body boundary conditions for free surfaces and interfaces. In particular, an external function is used in communicating to the FEM code the analytic stress tensor $\sigma_{ij}^{dislo}(u)$ $(i,j = 1,2,3)$ produced by a dislocation segment in a bulk [98]; then, we replace in Eq. 2.2 $\sigma_{ij}(u)$ with $\sigma_{ij}(u) + \sigma_{ij}^{0}$(u) where $\sigma_{ij}^{0}(u) = \sigma_{ij}^{dislo}(u)$ (i, j=1,2,3). The proper boundary value problem is then solved also where no external forces are considered ($f_i = 0$). When convergence is reached, the solution for $\sigma_{ij}(u)$ is found and the total stress tensor $\sigma_{ij}^{tot}(u)$ can be written as:

$$\sigma_{ij}^{tot}(u) = \sigma_{ij}^{surf}(u) + \sigma_{ij}^{int}(u) + \sigma_{ij}^{dislo}(u) \tag{3.1}$$

where $\sigma_{ij}^{surf}(u)$ is the correction to $\sigma_{ij}(u)$ due to the interaction between the dislocation and free surfaces (i.e. due to the first boundary condition in (1)), while $\sigma_{ij}^{int}(u)$ is the one due to the interaction between the extended defect and the interface (i.e. due to internal boundaries among different materials) [100].
The whole procedure has to be carried out taking into consideration that the bulk solution $\sigma_{ij}^{dislo}(u)$ (i ,j=1,2,3) is singular along the dislocation line, so that some technical requirements for the FEM calculation are needed. A first obvious condition is that the mesh used to solve the boundary value problem system must not contain nodes exactly along the dislocation line, otherwise infinite values would be introduced. In addition, a sufficiently dense mesh must be defined close to the core region, where the stress field reaches high values, also in derivative. This second key requirement can be fulfilled following a geometrical construction which also allows the quantitative estimates of the elastic energy in a dislocated structure. A small cylinder has been built around the dislocation line and we define a very dense array of nodes within it. We set the radius as $\left|\vec{b}\right|/\alpha$ with $\alpha = 2.71$. Excluding only such small cylinder (about 1,5 Åin radius) in the elastic energy calculation, the core contribution is empirically included (see e.g. Refs. [98, 9, 101]). Notice that the definition of a suitable grid, as the one described above, is straightforward within several available FEM packages. Meshes, indeed, can be automatically generated by the codes, at variable levels of node density, based solely on the geometry of the objects composing the system. By introducing the very small cylinder explicitly, one automatically forces the mesh generator to introduce several nodes around the core region, as it was desired. However, a careful control of convergence as function of the mesh density is mandatory.
To give a simple example of the flexibility and the accuracy of the method, we illustrate a case study where a direct comparison with the exact analytical solution is possible. Let us consider a dislocation with Burgers vector $\vec{b}$ and dislocation line $\vec{l}$ parallel to a single,

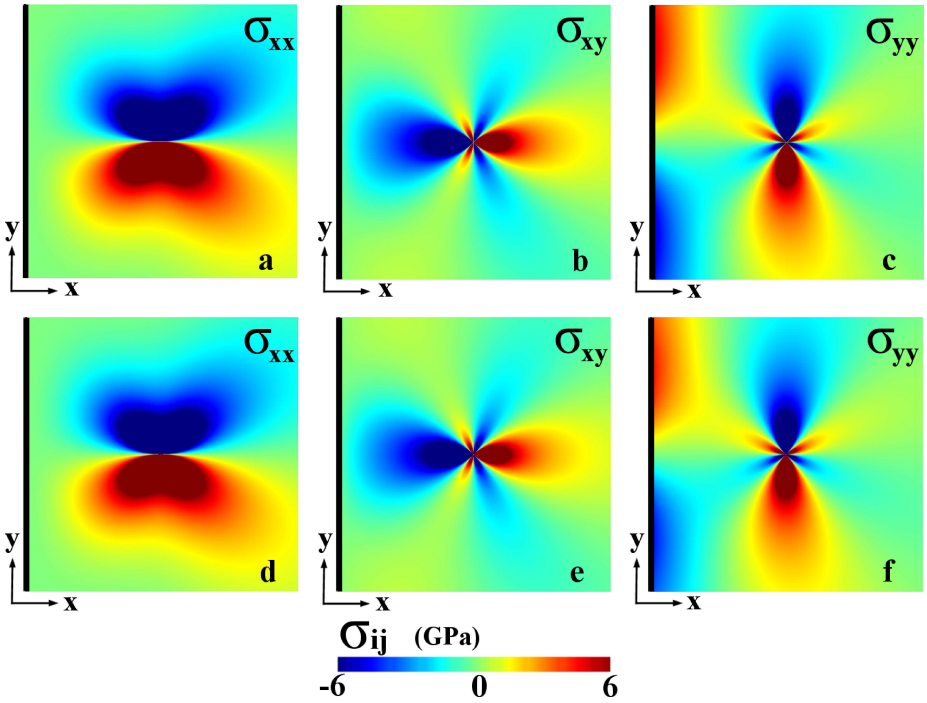

FIGURE 3.1: Panels (a), (b) and (c): various components of the edge dislocation stress field ($\vec{b} = [100], \vec{l} = [001]$) near a (100) surface (black line), calculated using the analytical solution by Heads [102].The dislocation is placed at a distance of 6 nm from the surface. Panels (d), (e) and (f): corresponding results obtained by direct solution of the elastic problem by FEM.

horizontal free surface (placed at x=0). While for pure screw character the exact solution is provided by a simple image method [98], it is more interesting to consider an edge dislocation. In this case, the problem is more complex, but it was nicely solved by Head [102], who supplied a solution valid for any distance d between the dislocation line and the surface, in the case of Burgers vectors perpendicular to the free surface. The Head solution, in terms of various components of the stress tensor is shown in the three upper panels of Fig. 3.1, while our results obtained by using FEM are displayed in the three lower ones. It is evident that a very good match is found. Outside the small cylinder around the dislocation line, indeed, the two solutions always differ by less than 0.1% of the stress value. Notice the stress field behavior close to the surface: while the σ_{xx} and σ_{xy} stress components (parallel to the normal $\vec{n}$) vanishes, σ_{yy} does not, at variance with the (wrong) result that one would obtain by using the approximated image method [98]. It is therefore clear that our method is suitable to handle dislocations in the presence of free surfaces. Due to the requirement in terms of mesh density, a significant computer memory (up to 8Gb for the results of Section 3 and 4) is needed to obtain stable results. Until a couple of years ago, this would have prevented similar calculations, so that smart attempts to circumvent the problem were proposed, avoiding to deal with the singularity directly in a FEM calculations. A particularly general and valid approach was introduced by Johnson and Freund (JF)[75], similar ideas being contained also in Ref.[96]. JF proposed to suitably split the elastic problem into two sub-problems. First, using the known analytical expression for σ_{ij}^{dislo}, tractions are computed at each free surfaces (components of the stress tensor normal to the surface itself). Then, a FEM calculation is performed for the system without dislocation, but using such tractions (opposite in sign) as boundary conditions. The bulk stress field

σ_{ij}^{dislo} is finally superimposed. In this way, the problem of using very dense meshes while solving the elastic problem is bypassed.
Recently, another possible approach has been presented [97, 100, 103]. With respect to the JF method, no explicit analytical expressions for σ_{ij}^{dislo} and no JF-like problem splitting are required. This *extended FEM* methodology seems very promising for treating systems containing several dislocations. However, some ad hoc technical FEM machinery needs to be implemented.
While the above methods are surely valid alternatives (we verified the perfect correspondence between our results and the JF approach for a simple test case), and might still prove to be essential for treating an elevated number of cores at the same time (a situation not encountered in this case [56]), our direct treatment of the dislocation field within FEM approach has some appealing features. First, it can be very easily implemented also within commercial FEM codes, where original sources are usually not available. A similar extension to use the method of Refs.[97, 100, 103] does not seem straightforward. With respect to the JF method, instead, one does not need to explicitly compute tractions. If their calculation poses no problems for simple geometries, for multifaceted heteroepitaxial islands one would need to carefully define the normal to each different exposed surface. In addition, if islands of different shapes need to be considered and compared, our direct approach allows one to move from one geometry to another very easily, particularly if the simple object-drawing features provided by most modern FEM packages are exploited.
In this Section we have demonstrated that an accurate, direct solution of the elastic problem posed by a straight dislocation segment in the presence of free surfaces can be obtained directly by FEM. Let us now apply this methodology to realistic heteroepitaxial System.

3.2 Dislocation engineering in patterned substrate

A first application to the developed method, is the study of dislocations in patterned substrate. We showed how by exploiting the inhomogeneous elastic field, produced in a trench patterned substrate is possible to achieve dislocation engineering.[1]

Dislocation engineering is the capability of governing the position and the shape of dislocations on a nanometric scale, i.e. controlling not only where the misfit segments (MS) are located, but also their extension and where their two ends are connected to a surface by threading arms (TA). For the epitaxial integration of different materials on Si(001), this achievement would allow for device positioning in sub-micrometer areas far from the detrimental TA. Defined access to the electrical conductivity of dislocations[104] and electroluminescence measurement[105, 106] are other fields that will benefit from dislocation engineering. However, this goal has always been out of hand, because heterogeneous nucleation of dislocation loops at unpredictable defects on the surface of the growing film and blocking of loops by pre-existing dislocations prevent any meaningful control. Recently, Ge[107] or GaAs[108] selective area deposition in oxide windows, or on small SiGe mesas,[109, 110] have allowed the blocking of TA. Still, the nucleation sites and the dislocation lengths are hard to control. In next paragraphs, we show that a turning point is the introduction of preferential nucleation sites at the interface between Si (001) and SiGe, which trap both the TA of dislocation lines running in one $\langle 110 \rangle$ direction, and the MS in the perpendicular direction. Guided by Finite Element Method (FEM) simulations, we

[1] This part of the work was made in collaboration with Francesca Boioli

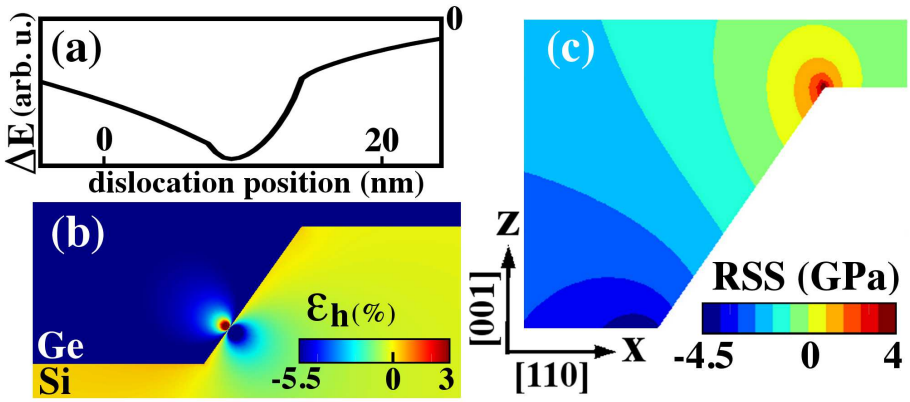

FIGURE 3.2: (a) Elastic energy of a 60° MS parallel to the $[\bar{1}10]$ direction with $\mathbf{b} = a_{Ge}[011]/2$ as a function of the x position along the Ge/Si interface. (b) Hydrostatic strain map of the dislocation in its energy minimum. Nucleation of such dislocations is favored at the upper edge of the $(\bar{1}\bar{1}1)$ plane, where RSS is maximum (c).

etched arrays of trenches with {111} facets of suitable spacing and width into Si (001), and showed by Atomic Force Microscopy (AFM) and Transmission Electron Microscopy (TEM) that efficient dislocation engineering is possible during mask-less heteroepitaxy of, here, $Si_{0.7}Ge_{0.3}$.

In the film growth-temperature regime, of SiGe on Si(001) a random network of 60° dislocations along the [110] and $[\bar{1}10]$ directions is observed, giving rise to a cross hatch morphology[111] that is readily observed by AFM. The lattice deformation induced by the MS of a 60° dislocation is composed of an expanded and a compressed lobe, which are mirror symmetric with respect to the {111} plane. It is easy to show by suitable FEM calculations[112] that the lowest elastic energy is obtained when the MS lies on a {111} interface between SiGe and Si. In Fig. 3.2(a), we report the elastic energy of a MS parallel to the $[\bar{1}10]$ direction, with Burgers vector $\mathbf{b} = a_{Ge}[011]/2$ (a_{Ge} is the germanium lattice parameter), as a function of the position x along the Ge/Si interface, patterned as shown in Fig. 3.2(b). The energy minimum corresponds to the MS in the $(\bar{1}\bar{1}1)$ interface plane. The map of the hydrostatic strain in such a position is shown in Fig. 3.2(b). In this configuration, the dislocation line generates an expansive lobe in the Ge film and a compressive one in the Si substrate. Both are perpendicular to the $(1\bar{1}1)$ interface, enhancing the total strain release. Fig. 3.2(c) maps the Resolved Shear Stress (RSS), which becomes maximum at the upper intersection between the $(\bar{1}\bar{1}1)$ and (001) planes. Here, dislocations will nucleate[98] and eventually glide within the $(\bar{1}\bar{1}1)$ interface plane to the energy minimum.

Let us consider now a substrate patterned with 350 nm wide trenches, periodically repeated along the [110] direction, and covered by a conformal, 160 nm thick $Si_{0.7}Ge_{0.3}$ film, as shown in Fig. 3.3. In our 2D geometry both the trenches and the MS are ideally infinite and parallel to the $[\bar{1}10]$ direction. We see from the FEM strain map in Fig. 3.3(a) that the presence of {111}-terminated trenches allows for a significant elastic relaxation of the ε_{xx} component in the epilayer even in the absence of dislocations. Therefore, we expect a reduced number of dislocation lines in the $[\bar{1}10]$ direction. From the calculation of the mean value of ε_{xx} in the epilayer, we found that in the coherent system the average residual strain ε_{xx} is $\sim$-6.7·10^{-3}, i.e. much lower than expected for a $Si_{0.7}Ge_{0.3}$ film grown on a flat Si(001) substrate ($\sim$-1.2·10^{-2}). Considering the same pattern geometry, we calculated the

equilibrium configuration of multiple dislocations in order to demonstrate that substrate patterning with {111} trenches is a suitable strategy for confining MS. In particular, for a given number of dislocations and their initial positions, we can calculate the force acting on each of them using the Peach and Kohehler equation[98]:

$$F = (\sigma(\mathbf{r}) \cdot \mathbf{b}) \times \ell(\mathbf{r}) \,, \tag{3.2}$$

where $\mathbf{b}$ and ℓ are the Burgers vector and the line vector of the dislocation, respectively, and $\mathbf{r} = (x, y, z)$ is the dislocation position. $\sigma(\mathbf{r}) = \sigma_{epi}(\mathbf{r}) + \sigma_{dsl}(\mathbf{r})$ is the position-dependent stress tensor consisting of the FEM-calculated epitaxial stress field σ_{epi} and the elastic field provided by all the dislocations in the system σ_{dsl}. The latter was calculated using the analytical formulation given in Ref. [113]. We computed the equilibrium configuration by using the steepest-descent algorithm. A random distribution of dislocations is generated, forces are calculated using eq. 3.2, and dislocations are moved along the force directions until the forces acting on each of them is zero. The equilibrium configuration is then obtained by repeating the elastic energy minimization for different initial dislocation positions and increasing their number up to the maximum allowed by the film thickness and trench periodicity. In the minimum energy configuration the dislocations are distributed exclusively in the {111} interfaces inside the trenches, as long as the trench period is $\leq$1.5 μm, (Fig. 3.3(b)). When the trench period exceeds 1.5 μm complete dislocation confinement in the trenches is lost. For a trench period of 1.8 μm, for instance, we predict that some dislocations are also located in the (001) interface between the trenches, as highlighted in the inset in Fig. 3.3(c). Thus, by varying both pattern geometry and Ge content it is possible to tune the range of trench periods where misfit dislocations become entirely confined inside the trenches.

To confirm our predictions, {111} faceted trenches were fabricated by a similar procedure as described in Ref. [114]. Regular arrays of trenches oriented along the [$\bar{1}$10] direction and with a spacing of 2 μm were defined by electron beam lithography on a Si (001) substrates covered with 70 nm of SiN_x. The pattern was transferred into the SiN_x layer via reactive ion etching to provide a hard mask for the subsequent anisotropic Si etching in Tetramethylammonium Hydroxide at 80 ° C. Since the etching rate in the Si <001> directions is $\sim$ 0.3 μm/min whereas the one for Si <111> is as small as $\sim$ 0.01 μm/min, trenches with well defined {111} side facets result.[115] The width and the depth of these trenches were defined by the size of the hard mask openings, here 350 nm and 250 nm, respectively, to match the model assumptions. The patterned substrates were then chemically pre-cleaned with a final dip in hydrofluoric acid and transferred to a Riber SIVA 45 solid source molecular beam epitaxy (MBE) system. After in-situ annealing at 700 ° C for 45 minutes, a 45 nm thick Si buffer layer was deposited at a rate of 0.6 Å/s at a temperature that was ramped up from 450 ° C to 550 ° C. An overcritical[9, 11] 160 nm thick $Si_{0.7}Ge_{0.3}$ layer was subsequently grown at T_{Ge}= 550 ° C, with rates of 0.18 Å/s and 0.41 Å/s for Ge and Si, respectively.

Fig. 3.4(a), shows an AFM image from the boundary region between the trench patterned area and the unprocessed surroundings. Evidently, most of the [$\bar{1}$10] oriented dislocations propagate as bundles from the sidewall areas of the trenches into the non-patterned area. Since the AFM measurements are only sensitive to the surface-footprint of several bunched dislocations, TEM investigations were carried out to identify individual dislocations and their TA. As in the case of the AFM image, we analyzed the region between the patterned and the non-patterned areas. Small apertures were used to improve the contrast,

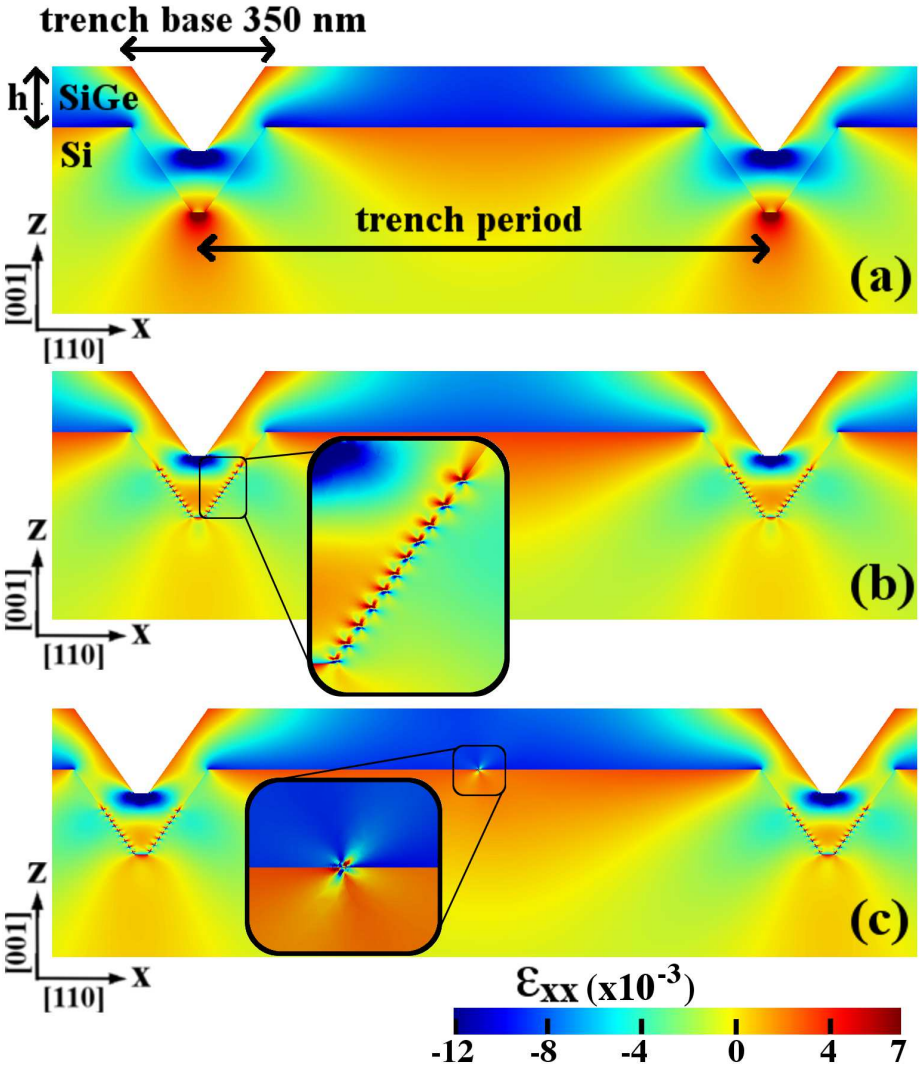

FIGURE 3.3: Map of the strain e_{xx} in the xz-plane for the coherent (a) and dislocated (b) system with a trench period of 1.5 μm and a film thickness h of 160 nm. Up to trench periods equal to 1.5 μm all dislocations are confined inside the trenches (b), while for larger periods (here: 1.8 μm), few dislocations are expected between the trenches (c).

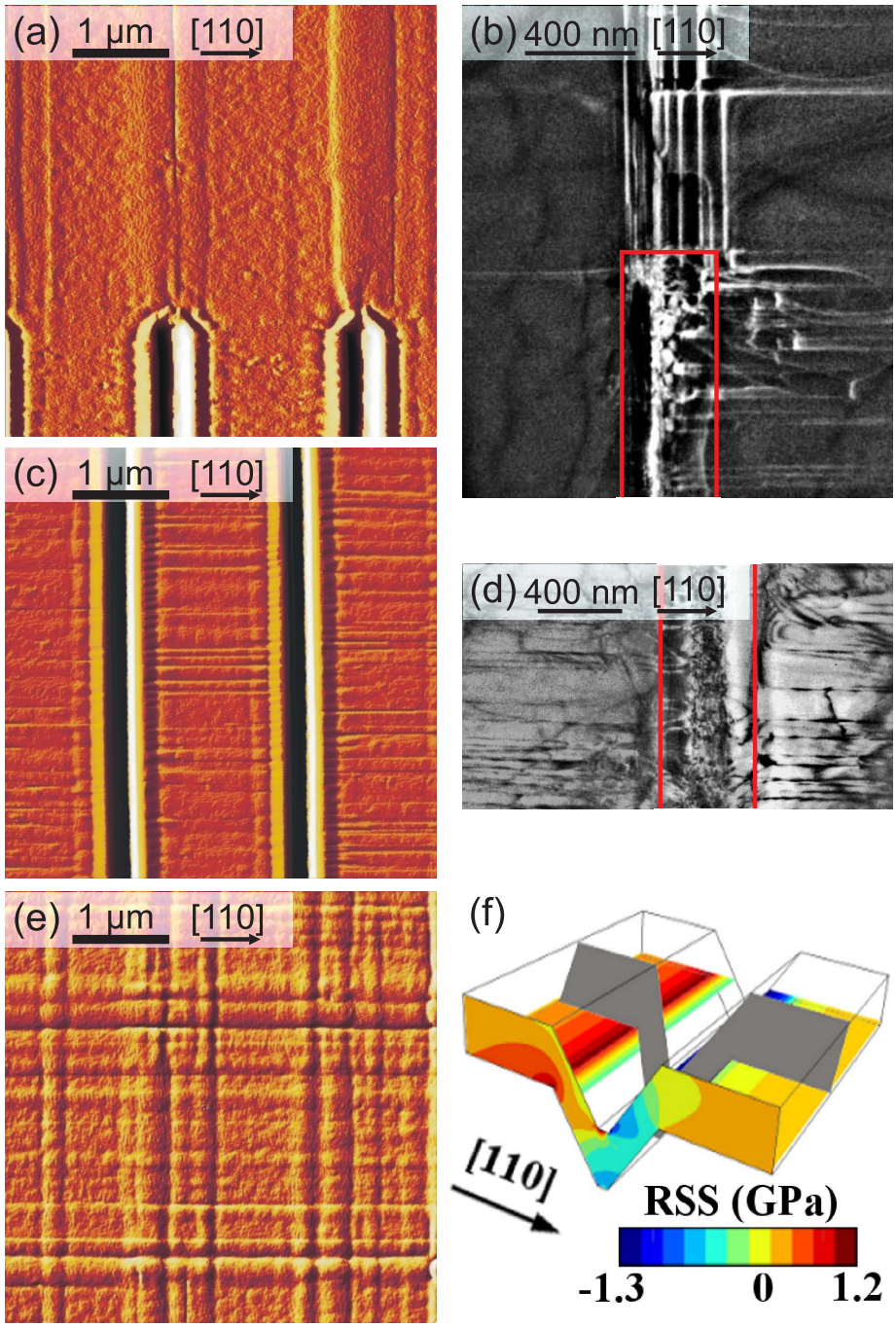

FIGURE 3.4: AFM images of the areas, where the {111} trench pattern ends (a), from the middle of the patterned (c) and non-patterned field (e), obtained after deposition of 160 nm $Si_{0.7}Ge_{0.3}$. Color coding corresponds to surface sensitive derivative. Plan view TEM images of the end of a trench (b), where dislocations are confined along the trench, and MS running from trench to trench (d). Trenches are outlined in red to guide eye. (f) RSS calculated for a 60° dislocation perpendicular to the trenches (parallel to the [110] with $\mathbf{b} = a_{SiGe}[0\bar{1}1]/2$ and $(1\bar{1}1)$ glide plane).

the specimen orientation was adjusted to get the highest dislocation contrast possible. Due to sample bending caused by residual strain and the presence of the trenches in the thin plan-view specimens, it was only possible to get good imaging condition in areas of about 0.5 μm^2. In Fig. 3.4(b) one can see that most dislocations parallel to the $[\bar{1}10]$ direction are confined along the trenches and extend into the non-patterned area, confirming both the model predictions and the AFM results. A few $[\bar{1}10]$ oriented dislocation lines are observed between trenches, because the experimental trench period of 2 μm exceeds the aforementioned limit of 1.5 μm for complete MS confinement in the trenches. Both the AFM and the TEM images also reveal that perpendicular to the trenches MS run from trench to trench as a dense network with narrow, rather regular distances, (Fig. 3.4(c) and (d)). TA can easily be identified in TEM images, because of their characteristic contrast modulation with a period that is related to the extinction length of the electrons employed for imaging. We find that most TA are located in the trenches, where they end on a sidewall surface. The area between the trenches has a much lower density of TA. Their occurrence is mainly associated with occasional stacking faults caused by not-yet optimized growth conditions on the 111 sidewalls of the trenches. In the non-patterned area, Fig. 3.4(e), an irregular network of bundled dislocations is observed, giving rise to a superficial cross hatch morphology associated with dislocations along the [110] and the $[\bar{1}10]$ directions. In contrast, the presence of trenches substantially affects dislocation formation: MS parallel to the trenches are confined inside them and the ones perpendicular to the trenches produce a rather uniform distribution. The latter finding is probably due to the high RSS at the upper trench edges, which provides preferential sites for homogeneous dislocation nucleation in the patterned area. In Fig. 3.4(f) the RSS calculated for a 60 ° straight dislocation parallel to the [110] direction (i.e. perpendicular to the trenches), with Burgers vector $\mathbf{b} = a_{SiGe}[011]/2$ (a_{SiGe} is the $Si_{0.7}Ge_{0.3}$ alloy lattice parameter), is plotted. Since the RSS reaches its maximum at the upper trench edge where it is much higher than in flat films, we expect dislocations to be more easily nucleated in films grown on such patterned substrates. This effect allows for the formation of a homogenous distribution of dislocations perpendicular to the trenches.

In conclusion, our model predictions and experimental results clearly suggest that substrate patterning with {111}-terminated trenches is an effective method for trapping misfit dislocations parallel to the trenches. Their density is low, since the relaxation of the strain component perpendicular to the trenches is mainly of elastic nature. In contrast, the strain component along the trench direction is plastically relaxed by a quite regular array of misfit segments that run from trench to trench. Their threading arms are effectively trapped on the open sidewalls of the trenches. It is therefore possible to fabricate relatively large film areas ($\sim$1 μm^2) free of threading dislocations, which demonstrates that our mask-less approach can provide efficient dislocation engineering.

4

Plastic relaxation onset in heteroepitaxial islands

This chapter effort is the study and understanding of the onset of plastic relaxation in heteroepitaxial SiGe islands. The plastic onset is determined making use of thermodynamic criteria, exploiting the method described in chapter 3. In fact, the onset of plastic relaxation occurs in small volumes, involves only single nucleation event, and misfit dislocations are the main actors in such process, threading segments can be neglected. The detailed stress field and the elastic energy of an island with a single 60◦ misfit dislocation is computed, determining the critical volume of injection of the first dislocation, finding a good agreement with experimental data.

4.1 Modeling of dislocated islands by FEM

As shown in chapter 2, before the onset of plastic relaxation, the elastic field in the island is completely determined by its shape and composition. This section is devoted to the study of stress field of the dislocated island case. We shall recall that the calculation of the complex elastic field in a dislocated dot is the actual goal of our FEM methodology, and that the results here reported allow for a complete description of stress and strain field in realistic shaped 3D islands.

In Ref. [56] it has been addressed that the onset of plastic relaxation in SiGe islands grown on a Si(001) substrates occurs in barn shaped islands, we followed this suggestion and addressed the dislocated dots to be a barn. Moreover as in Ref. [56], we focus on perfect straight 60° dislocation segments (typical of Si and Ge diamond structure). Different island composition and size have been considered, along with different dislocation position at the island-substrate interface (see Section).

In Chapter 2 we described the procedure to calculate via FEM the elastic field in a finite system where the stresses are originated only by the presence of a dislocation segment. In one dislocated island, instead, both the elastic field due to lattice misfit with the substrate and the one due to the dislocation are present. The superposition principle holding for linear system allows us to simply sum the two initial stress $\sigma^0_{ij}(u)$ for one unique BVP problem. Therefore in Eq.(2.2) $\sigma_{ij}(u)$ becomes $\sigma_{ij}(u) + \sigma^0_{ij}(u)$ $(i, j = 1, 2, 3)$ with:

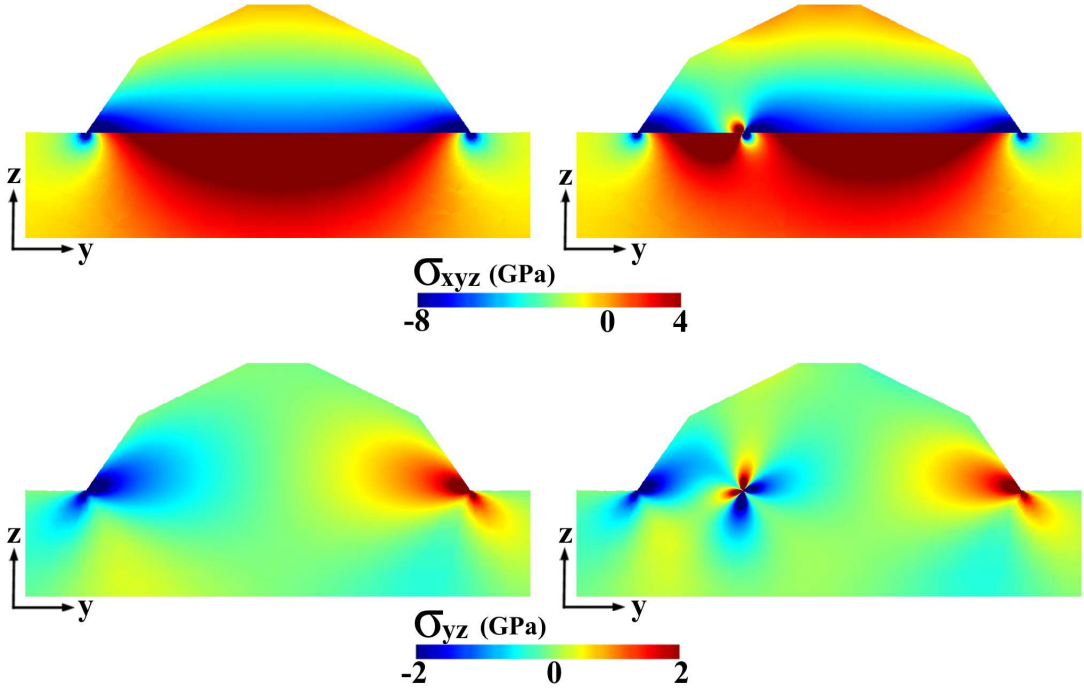

FIGURE 4.1: Hydrostatic (upper panels) and shear (bottom panels) stress components mapped in a central barn section. Left panels show the case of a coherent 35 nm based island, while the right panels show the same system when a 60° dislocation is introduced.

$$\begin{cases} \sigma_{ij} = \mathcal{C}_{ijkl}\,\epsilon_m + \sigma_{ij}^{dislo} & \text{island} \\ \sigma_{ij} = \sigma_{ij}^{dislo} & \text{substrate} \end{cases} \tag{4.1}$$

In particular, we chose to orient the dislocation line $\vec{l}$ along [110] direction (here and in the following the direction of the x axis, being z axis along [001] and y along ([$\bar{1}$10]) and we take the Burgers vector $\vec{b} = \frac{a_{Ge}}{2}$ [011]. Then the relative analytic stress tensor $\sigma_{ij}^{dislo}(u)$ is obtained as in Ref. 21 for a dislocation segment actually starting on one side of the island and ending at the opposite one. We neglect the presence of threading arms and we place the dislocation segment always at the interface with the substrate. Both simplifications find their physical reason in a realistic picture of the dislocation evolution after its nucleation: the misfit segment has to be elongated as much as possible, in order to maximize the strain release, so that the threading arms have to become as short as possible and the dislocation has to move towards the interface.

Results for a pure Ge dislocated barn are plotted in right panels of Fig. 4.1, allowing for a close comparison with the coherent case (left panels). The island base was realistically set to 35 nm [54, 56]. Notice the importance of specifying the islands dimensions. The coherent case is self-similar, so that the stress field can be scaled to represent any island of the same shape. This is not possible anymore when a dislocation is considered, since the Burgers vector introduces an intrinsic length scale. The dislocation was placed exactly at the interface at a relative distance of about 0.3 from the closest barn edge with respect to the island base, i.e. in the position that in Ref. [56] was indicated to be the lowest in total energy (as reported in the next section we found exact the same result).

Looking at the hydrostatic components σ_{xyz} (upper panels in the figure) it can be observed

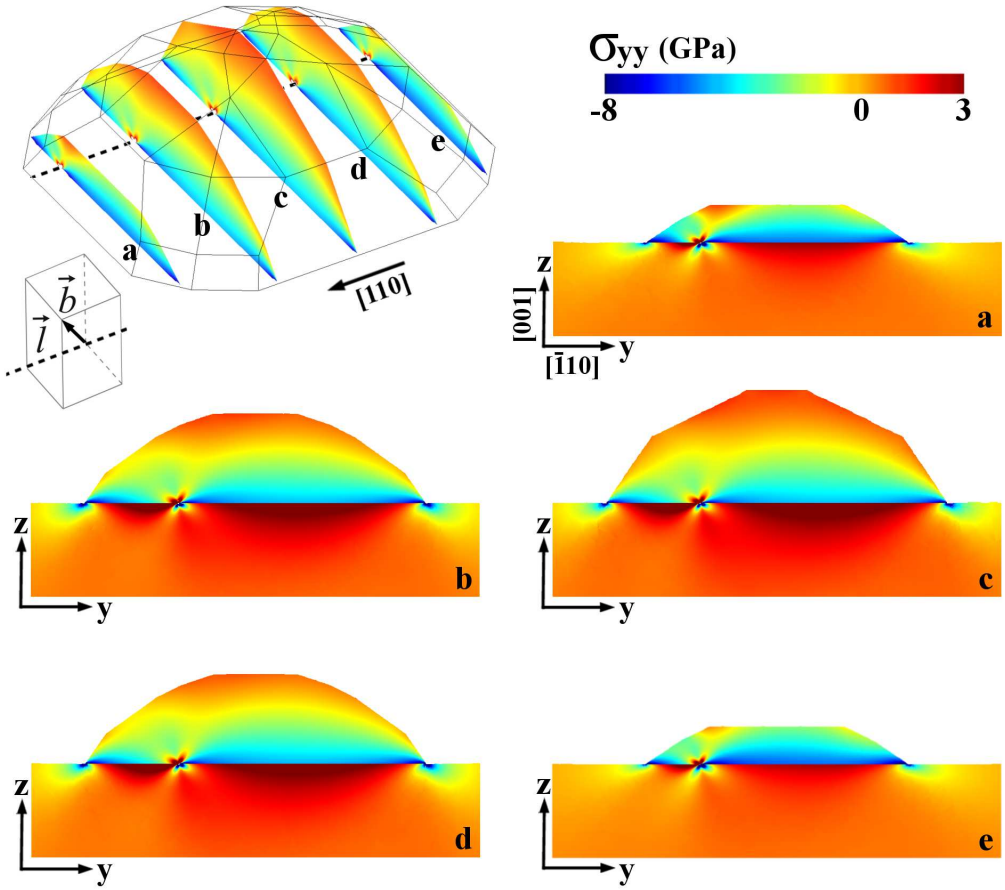

FIGURE 4.2: Elastic field in a 3D dislocated barn. Panels report color maps of the σ_{yy} component for different island cross sections, along the dislocation line. The cross sections in the island are shown in the top left panel, along with a sketch of dislocation line and Burgers vector orientation.

how the presence of the dislocation allows for a strong reduction of the compression at the island edge closer to the core, i.e. exactly where the elastic relaxation does not provide a good way for lowering the stress load arising from the lattice mismatch. The influence on the Si substrate is also interesting. Below the dislocation core, a compressive lobe is created. While this causes strong negative stress values right below the core, at larger distances it allows for a reduction of the tensile Si region. The components σ_{yz} illustrated in the bottom panels of Fig. 4.1 give an example on the local modification induced by the 60° dislocation segment in reducing the shear deformation.

Proceeding with the analysis of the dislocation-induced stress field in the barn, in Fig. 4.2 we show the σ_{yy} component of the stress field at different positions within the island.

We find the comparison between the various panels of Fig. 4.2 particularly appealing, since it clarifies the complex interaction between the dislocation and the various island facets, highlighting the importance of performing actual three-dimensional calculations. The overall stress field is determined by several factors. Beside the position-dependent lattice mismatch contribution, the relative position with respect to both the dislocation line and the free surfaces is important, together with the relative orientation of the Burgers

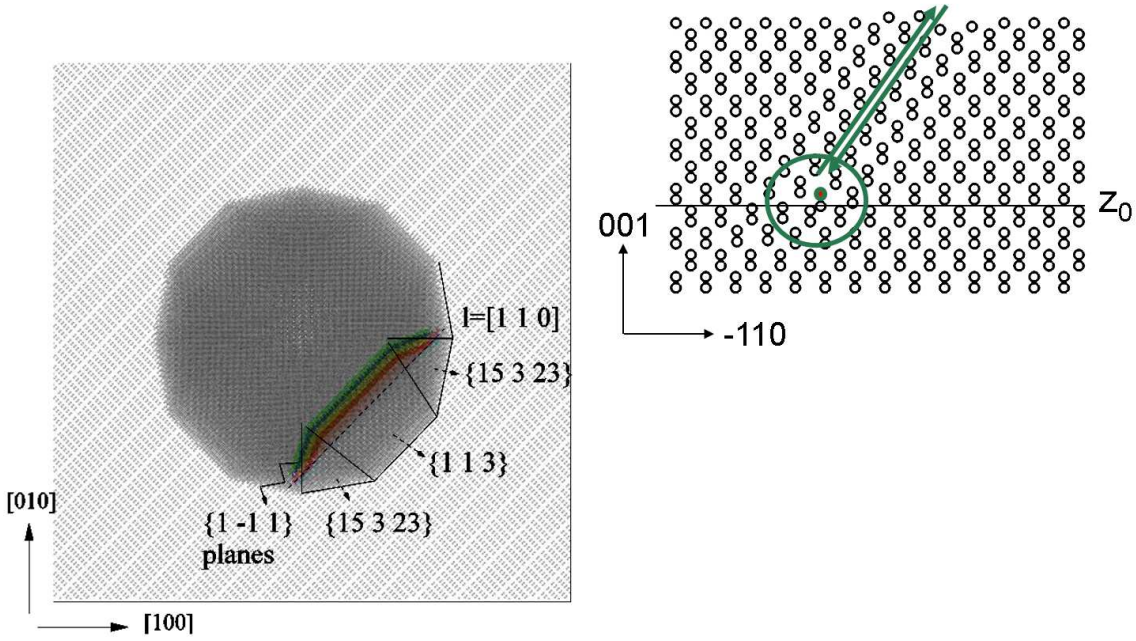

FIGURE 4.3: Left panel: dome island as built in MD code, the facets are indicated and the {111} planes mostly involved in the initial deformation have been highlighted in color. Right panel: sketch of the atomistic generation of the dislocation, z_0 being the interface level.

vector (shown separately in the figure) and of the normal to the closer facet. In the cross section of Fig. 4.2 (a), one observes a strong dislocation contribution reaching the free surface (upper left corner in the panel). In that region the dislocation core is very close to a free surface and, more importantly, the Burgers vector is almost normal to the facet. In cross section displayed in Fig. 4.2 (e), instead, the Burgers vector is parallel to the surface causing a weaker relaxation close to the surface (orange area). Finally, in the central sections of the island [panels (b), (c), (d)], the typical butterfly-shaped dislocation stress field is observed to become less significant while moving from the base to the top, where the elastic relaxation is maximum.

As a further confirmation of the method accuracy we chose to compare the elastic field of a dislocated island as found by our full FEM methodology with the same result calculated via atomistic simulations. We compare our results with Molecular Dynamics (MD) ones based on the Tersoff empirical potential [116, 50]. This comparison also allows for analyzing atomic-scale effects, which are not present in the continuum approach. Instead of a barn, we here consider a dome island [84] (see Fig. 4.3), since this allows us to reduce the number of atoms to be considered, still dealing with realistically sized and shaped islands. In order to introduce a 60° dislocation segment in the island analogous to the one previously treated by FEM, we applied the same procedure successfully used in Refs. [117, 118] for the simpler case of a flat film. In particular, we chose to induce the dislocation in the shuffle set (in elastic continuum calculations the dislocation setting is not relevant as no lattice is present). Briefly, a specific {111} glide plane is selected, together with the vertical position for the dislocation core. Suitably modulated rigid shears are applied above the core position: atoms on one side of the glide plane are sheared in the direction of the Burgers vector, while atoms at the other side are moved in the opposite one. In the left panel of Fig. 4.3 the island as

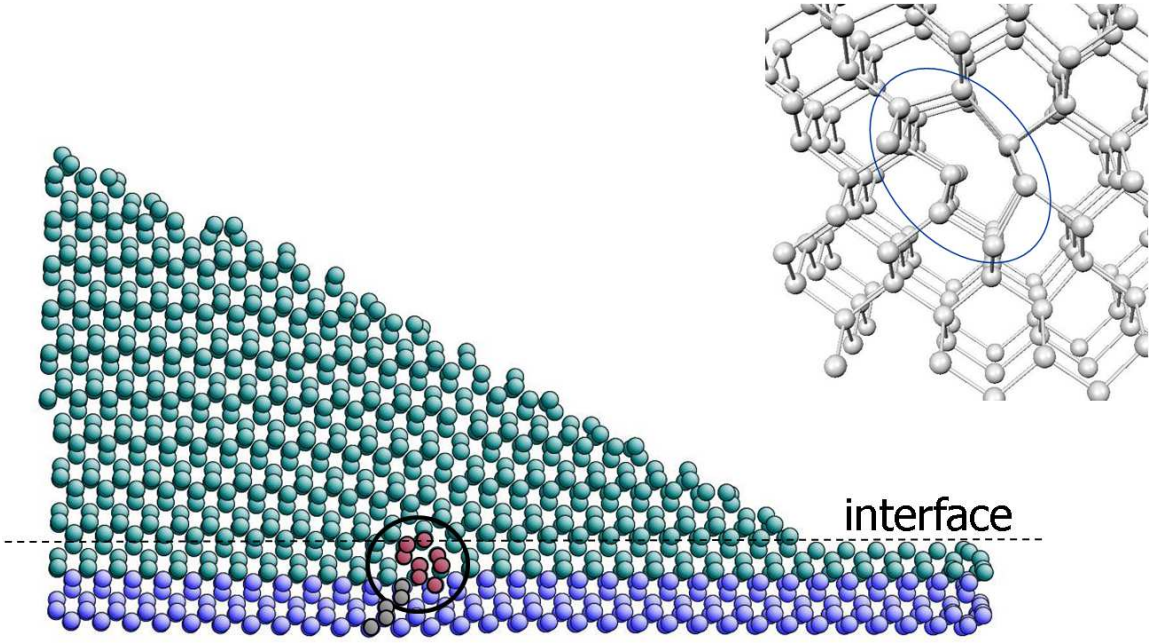

FIGURE 4.4: 60° dislocation in a dome island as obtained via atomistic simulation. The core position is encircled. Core atoms and the half extra plane are highlighted. The detailed atomistic configuration is shown in the right panel.

built up in the MD code is shown from a top view. The atomic planes mostly involved in the displacements are highlighted. The right panel of Fig. 4.3 , instead, contains a sketch of the procedure used to generate the dislocation.

After the preparation of the initial configuration, a simulated annealing procedure was run in order to minimize the total energy in the dislocated configuration, reaching a temperature of 400K before bringing the system down to zero temperature. The applied initial displacement is sufficient to guarantee that the minimization procedure causes only minor atoms arrangement around the induced dislocation core, avoiding the system to get back to the perfect crystal configuration. During the simulation, periodic boundary conditions were applied in the directions parallel to the substrate, and the bottom four layers of the supercell were kept frozen to bulk position. The total system was composed of $\approx 1.5 \times 10^6$ atoms. 58 layers were used to describe the Si substrate, each of them composed by ˜21600 atoms, completed by a 3ML Ge wetting layer and by the dome island, made of about 118000 Ge atoms.

Fig. 4.4 presents a portion of the final configuration, highlighting the presence of a 60° shuffle dislocation segment at the island base. The core structure is shown in the right panel.

The same dome island has been then constructed in the FEM code and a 60° dislocation has been introduced in the same position. In order to draw a closer comparison, we used the elastic constants predicted by the Tersoff potentials[116, 50]. Panels in Fig. 4.5 show the color maps of the hydrostatic strain resulting from the two approaches. It is evident the good qualitative and quantitative correspondence.

An obvious difference is seen close to the free surfaces, the steep dome facets being here stepped in their as-cut configuration. Each step is a source of alternating compressive and tensile regions, this effect being absent in the FEM calculation. Notice that the step-

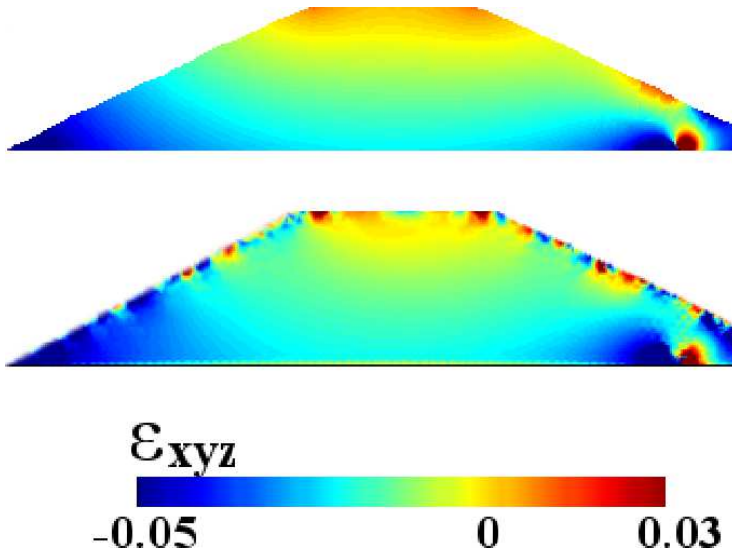

FIGURE 4.5: Color map of the hydrostatic strain in the central cross section of a 3D dome island (32 nm in base) as obtained by FEM calculations (upper panel) and Tersoff-potential MD (bottom panel).

induced effect seen in the MD results is doubtfully realistic since reconstructions (unknown for the high-index facets of a dome) are expected to change the surface stresses. Moreover, also the top (001) dome facet is built up in the MD code without introducing possible reconstruction, random rebonding in dimers occurs during the simulated annealing, giving rise to local stresses.
Overall, the FEM approach, while recovering the correct result, allowed for a two orders of magnitude saving in computational time for this prototypical case. Estimating the critical volume for plastic relaxation (particularly at low Ge contents, yielding larger islands) by MD is prohibitive, so that in the following we shall drop the atomistic approach.

4.2 Calculation of plastic onset and comparison with different approaches

In the previous section we have demonstrated that FEM calculations can yield a reliable description of the elastic field in a dislocated island. Before exploiting them to yield an accurate estimation of the critical volume for plastic relaxation onset, we find interesting to introduce two more approximated, still analytic, approaches, in order to compare the different predictions and to understand which are the key contributions determining the system behavior.
On general grounds, the total elastic energy stored in an heteroepitaxial island in the presence of a dislocation can be written as:

$$E_{tot} = E_{coh} + E_{gain} + E_{cost} \tag{4.2}$$

where E_{coh} is the elastic energy of the coherent dot, E_{gain} accounts for the energy lowering corresponding to the effective misfit reduction, provided by the dislocation, and E_{cost} the energy of the additional lattice deformation produced by the defect. Different approaches can yield an explicit expression for the three terms contained in Eq.(4.2), at different levels of approximation.

4.2.1 Peach-Koehler approach

A more detailed procedure has to take into consideration the actual (position dependent) interaction between the dislocation and the inhomogeneous elastic field of the island, before the onset of plastic relaxation. A combination of FEM calculations and dislocation theory provides a viable way.
The misfit reduction due to the presence of a dislocation can be viewed as the interaction between the strain field in the island and the dislocation Burgers vector: such an interaction depends, obviously, on the dislocation position. In details, the stress in the island $\hat{\sigma}\,(x, y, z)$ exerts a force (Peach-Koehler force) $d\vec{F} = \vec{b} \cdot \hat{\sigma}(x, y, z) \times d\vec{l}$ on each infinitesimal segment of the dislocation line $(d\vec{l})$, being $\vec{b}$ the relative Burgers vector, moving the dislocation segment to the position maximizing strain relaxation in the island. The position dependent energy gain term can be modeled as the work due to place a dislocation segment from outside the island into any position [119, 120].
Our results are referred to a 60° dislocation segment running along the x axis direction ([110]) and with $\vec{b} = \frac{a_{SiGe}}{2}$ [011]. The work performed by the Peach-Koehler force to place that segment from the outer of the island in any position (y_0, z_0) reads:

$$E_{gain}(y_0, z_0) = \left[b_y \int_{z_0}^{h(y_0,z_0)} \left(\int_{l(y_0,z)} \sigma_{yy} dx \right) dz + b_z \int_{z_0}^{h(y_0,z_0)} \left(\int_{l(y_0,z)} \sigma_{yz} dy \right) dz \right] \tag{4.3}$$

where $h\,(y_0, z_0)$ is the distance of the (y_0, z_0) position from the free surface along z, and $l\,(y_0, z)$ is the dislocation line length along x, which depends on z. Finally, b_y, b_z represent the components of the Burgers vector in the y ($[\bar{1}10]$) and in the z ([001]) directions, respectively. We recall that the integral of the Peach-Koehler force starting from the surface (energy $E = 0$) is path independent if the stress field is calculated at the equilibrium, so that it is possible and convenient to calculate E_{gain} along a straight vertical path, from the surface to the most favorable position in the island (always along the interface with the substrate).
Let us consider now the E_{cost} term, the analytical formulation is

$$E_{cost} = \lambda \frac{G(1 - \nu \cos^2 \beta) b^2}{4\pi(1 - \nu)} \ln \frac{\alpha R_{cutt-off}}{b} \tag{4.4}$$

where β is the angle between dislocation line and Burgers vector, α is the parameter which describes the energy of the dislocation, set equal to 2.7 as in Ref. [9], and b the length of the Burgers vector. For finite system, the role of the free surfaces in reducing the extension of the dislocation elastic field (see e.g. Fig. 3.1) is commonly enclosed in the analytical model using a suitable choice of $R_{cut-off}$ as a cut-off radius of the dislocation self field. $R_{cut-off}$ is a function of the dislocation position. In particular $R_{cut-off}$ is defined as the geometric average of the distances of the dislocation position from the base edge and the free surface above, as calculated in the middle cross section of the island. The limits of such approximation will be highlighted upon comparison with the full FEM results.

4.2.2 Comparison between different approaches

Figure 4.6 reports the three contributions E_{cost}, E_{gain} and E_{tot}, as calculated in the case of a pure Ge barn (basis L=35 nm) by the proposed full FEM methodology (Section 3.1) and by the Peach-Koehler approach (PKA) . Actually, E_{tot} is shown in the third panel of Fig. 4.6 after subtraction of the corresponding coherent energy E_{coh}, so that positive

(or negative) values indicate an overall energetic increase (or decrease) provided by the presence of the dislocation.
The calculation of the individual energy terms in the full FEM approach is done as follows. After the equilibrium condition is found, the FEM code provides the stress and strain fields, so that the total elastic energy in a volume V can be computed by the well-known relation:

$$E = \frac{1}{2}\int_V (\sigma_{xx}\varepsilon_{xx} + \sigma_{yy}\varepsilon_{yy} + \sigma_{zz}\varepsilon_{zz} + 2\sigma_{xy}\varepsilon_{xy} + 2\sigma_{xz}\varepsilon_{xz} + 2\sigma_{yz}\varepsilon_{yz})dV \qquad (4.5)$$

By integrating over the whole system volume, one would include in E the (wrong) contribution coming from the core region. We therefore integrate everywhere but for the small cylinder built around the core (see Section 3.1). This yields the total elastic energy E_{tot}. Following the definition, E_{cost} is actually given by the elastic energy in the zero-misfit island, when only the dislocation is present. So that, E_{gain} can be directly computed by subtraction.
The comparison of the E_{cost} terms shown in the first panel of Fig. 4.6 clearly reveals some limitations of the PKA treatment, where the influence of free surfaces on the dislocation field is described only by the introduction of a cut off radius R related to the island geometry. An immediate consequence is that the PKA curve is symmetric, merely reflecting the barn geometry, while the full FEM curve correctly shows a behavior determined by the dependence of the elastic field on the relative orientation of the different surfaces and the Burgers vector. Since at the two opposite island edges the facet normal is differently oriented, a different E_{cost} must be expected. The effect of the relative-orientation depending elastic field revealed by full FEM is particularly important in nanometric multifaceted island, where the dislocation line turns to be always close to a free surfaces, and it is here investigated in details for the first time.
In Fig. 4.7 the role played by the free surfaces (and the interface) is made clear by plotting the difference between the hydrostatic stress for the equilibrium solution when only the dislocation segment is present and the dislocation analytical bulk solution (reported in the upper panel) [98]; i.e. following the definitions of Section 3.1, Fig. 4.7 shows $\sigma^{tot}_{xyz}(u) - \sigma^{dislo}_{xyz}(u) = \sigma^{surf}_{xyz}(u) + \sigma^{int}_{xyz}(u)$. The middle panel displays the behavior obtained by placing the dislocation in the minimum of the E_{tot} curve and the lower one reports the data obtained when the dislocation is in a symmetric position on the other island side. Notice that the $\sigma^{surf}_{xyz}(u) + \sigma^{int}_{xyz}(u)$ actually reduces the dislocation field (upper panel) being opposite in sign. Indeed the E_{cost} found in the PKA approach results higher with respect to the full FEM one because of the too simple approximation used for the surface contribution that corresponds to a simple geometric cut off of the dislocation field. The comparison between the middle and the bottom panel highlights the dislocation position dependence of the surface terms that gives rise to the asymmetry in the full FEM E_{cost} curve. From Fig. 4.7 we conclude also that no significant effect seems to be present due to the Ge/Si interface at the bottom of the island ($\sigma^{int}_{xyz}(u)$, see Section 3.1), mainly because of the very similar values of the elastic constants of the two materials.
Let us now focus our attention on the E_{gain} term, reported in the central panel of Fig. 4.6. Actually, the Peach-Koehler force is shown to yield a good qualitative description of the interaction between the dislocation field and the epitaxial one. Indeed, the use of the FEM-computed elastic field in the island before the onset of the plastic relaxation in the PKA expressions guarantees a correct estimation of the energy reduction obtained when a dislocation is introduced. Very importantly, the PKA and full FEM curves present the

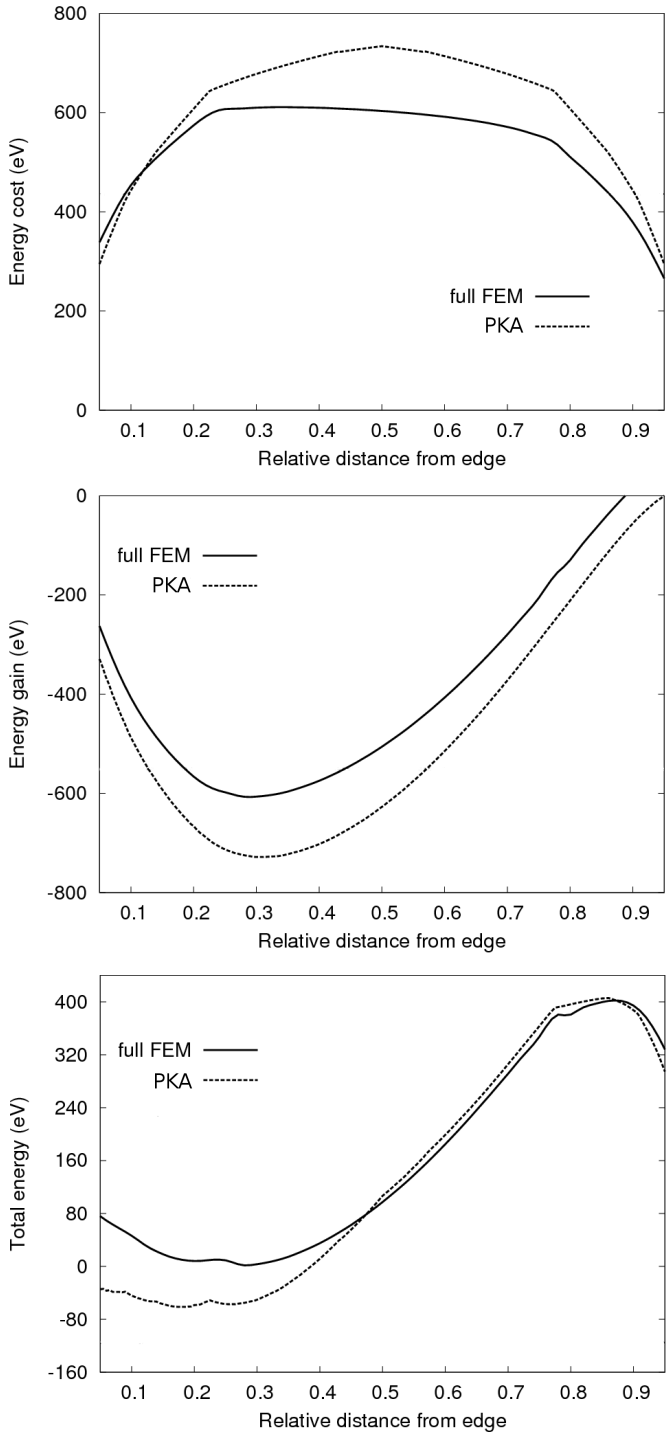

FIGURE 4.6: Comparison between full FEM, PKA results for a barn island with base L= 35 nm. First panel reports the values of E_{cost}, middle panel of E_{gain} and the bottom one of E_{tot}.

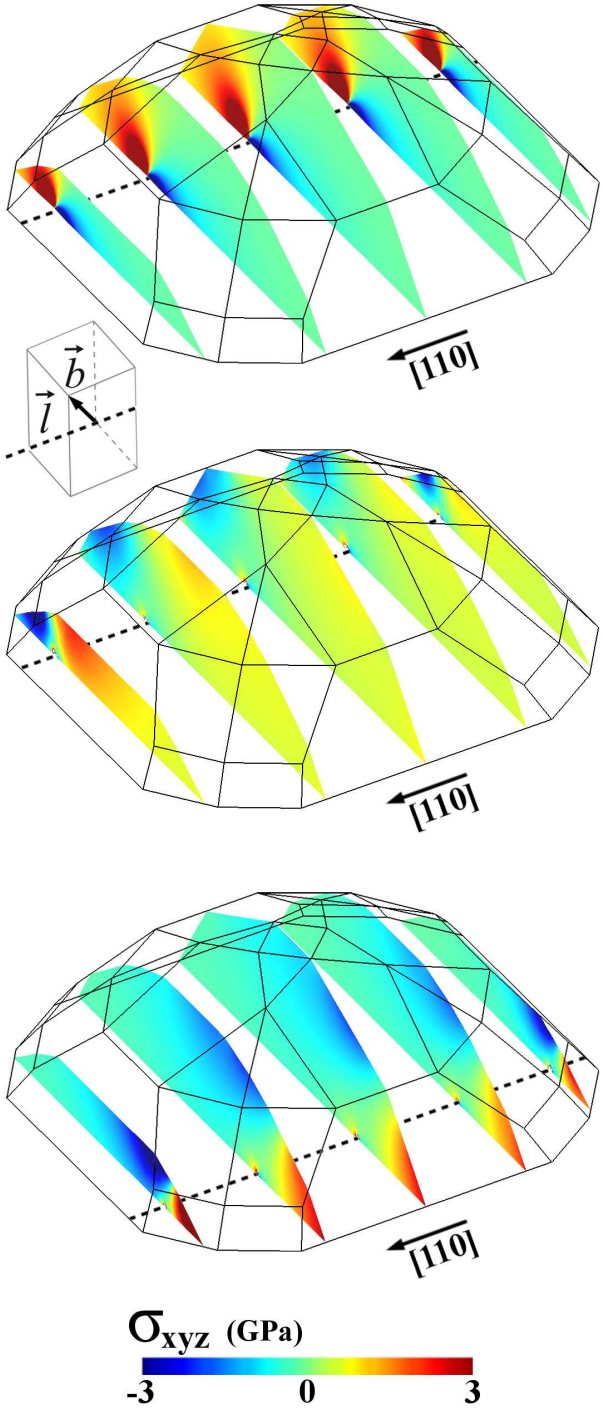

FIGURE 4.7: Color maps of the hydrostatic stress in different cross sections of the barn cut along the dislocation line ($\vec{l}$). In the upper panel it is shown the analytical dislocation segment bulk solution $\sigma^{dislo}_{xyz}(u)$ (cut following the barn shape), the defect is located in the position corresponding to the E_{tot} minimum. The central and the lower panel describe only the dislocation-surface interaction ($\sigma^{surf}_{xyz}(u) + \sigma^{int}_{xyz}(u)$): the former refers to the same position of the upper panel, the latter for a symmetric position on the other island side.

minimum at the same position along the interface ($\tilde{0}.3$), so the two models predict the same equilibrium dislocation position. It is important to notice that such position, maximum in the energy reduction, actually corresponds to a strong release of the island edge compression due to the expansive lobe of the dislocation field (see upper right panel in Fig. 4.1). From the quantitative point of view, instead, the energy gain seems to be overestimated by the PKA approach. Since the same behavior was found for E_{cost} (opposite in sign), the total energy curve is expected to benefit from this compensation. Indeed, by looking at the bottom panel of Fig. 4.1, one sees that full FEM and PK give very close results in the central region. It is evident, instead, the failure of the PK-based approach in regions where the dislocation is in the proximity of the island edge, closer to the optimal position. Notice that the minimum of E_{tot} (we recall that E_{coh} was subtracted) for the full FEM calculation corresponds to 0 eV. This is because the comparison reported in this Section was performed exactly at the full FEM critical volume for dislocation introduction. The Next Section is dedicated to a more detailed investigation of critical volumes, including a comparison to Ge concentration-dependent experimental data.

4.2.3 Prediction of the critical size vs experiments

A useful and interesting application of the methods described in 3 is the calculation of the critical island dimension for the onset of plastic relaxation. Such calculation has been already published in the Peach-Koehler framework for SiGe islands [56]. Here we compare the PKA results with the one obtained using the more accurate full FEM approach. Critical volumes V_C are defined as the smaller island dimensions where it exists at least one dislocation position where $E_{gain} = -E_{cost}$. Clearly, finding V_C requires calculating the two terms for different island sizes and for different dislocation positions along the interface. If in the previous sections we simply considered pure Ge islands, here we wish to carry out the calculations at realistic Ge compositions. We considered values ranging between 20% and 70% as determined in Ref. [56] by using different growth temperatures. In the FEM calculations, alloying can be tackled by considering a rescaled misfit stress $\sigma_m = -8.6x_{Ge}$ GPa where x_{Ge} is the Ge content and also linearly interpolated elastic constants ($C_{ij}^{SiGe}(x_{Ge}) = x_{Ge}C_{ij}^{Ge} + (1-x_{Ge})C_{ij}^{Si}$). Results, obtained by full FEM and PKA are displayed in Fig. 4.8, along with the experimental data of Ref. [56]. With respect to that work, here only the data where the concentration values were determined by independent and more accurate X-rays measurements are shown. In the plot, the vertical axis represent the barn critical island base, experimentally estimated by looking at the internal plateau regions revealed by selective etching [56]. Let us first focus on the two models.

While the two theoretical curves all capture the essential physics (higher Ge concentrations determine larger elastic-energy accumulation, and, therefore, smaller critical volumes), a closer comparison reveals once again the different levels of approximation, full FEM yielding a virtually exact description. The sizeable underestimation of the E_{gain} term in the PKA approach, as expected, yields too small critical sizes. Interestingly, despite the approximations discussed in the previous Section, critical islands dimensions predicted by the PKA method do not deviate substantially from the full FEM results, particularly if one takes into account the large experimental uncertainties on the actual Ge content. However, it is well visible that the most accurate full FEM approach better recovers the data. Overall, the agreement between the latter and experiments is very satisfactory and reinforces the main conclusion of Ref.[56]: dislocation injection in nanometric island is not kinetically

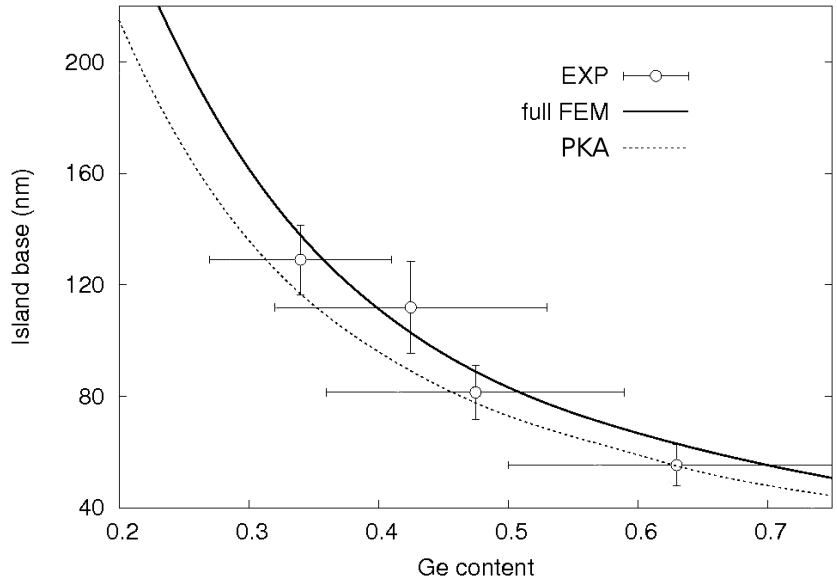

FIGURE 4.8: Critical island bases as calculated by the two different method (fullFEM,PKA), and compared with the experimental data of Ref. [56]

limited all along the concentration (and, thus, the temperature) range, at variance to the flat film case.

As a final investigation, we carried out a comparison between the thermodynamic critical height in islands and in flat films. Using only the FEM approach, the critical height h_c determining dislocation injection in films have been determined for the same concentration values previously considered for the barns, together with the pure Ge case. It may appear of limited interest to investigate the very Ge-rich case, where flat films can be grown only by freezing the surface atomistic diffusion (i.e. using a high H concentration in PECVD growth). Still, in this case h_c is very small, and the role of the surfaces is much larger, the one of threading arms much smaller. In Fig. 4.9, h_c is compared with the corresponding height of barn islands at the critical volume. It is evident that, from the thermodynamic point of view, higher structures can be reached before the onset of plastic relaxation in a three dimensional growth with respect to the two-dimensional one, the effect being particularly pronounced at low misfit values. However, at variance with islands, measured values for critical films seem much higher than the thermodynamic predictions,[101, 14] highlighting a key role of the kinetic barriers opposing to dislocation nucleation in films.

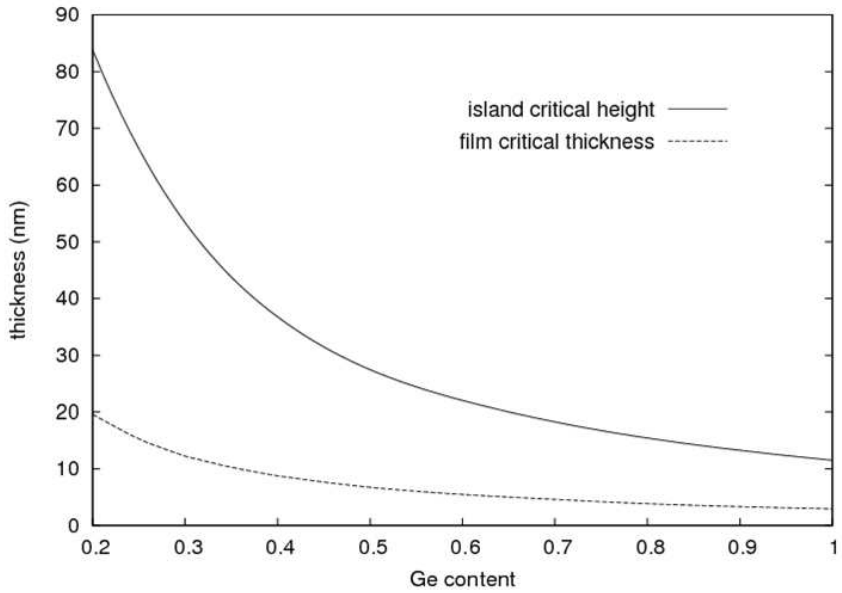

FIGURE 4.9: Critical thickness for flat films (dashed line), as compared to the barn island height (solid line), both calculated by full FEM.

5

Beyond plastic relaxation: Late stage of cyclic growth.

This chapter is devoted to the understanding of late stage of cyclic growth. When the onset of plastic relaxation is bypassed, islands volumes become larger and a cyclic growth mechanism is observed [52]. The method used in Chapter 3 is computational demanding and cannot be exploited to study multi dislocated island. A simple analytical was successfully used to determine the critical volumes and the periodic spacing between dislocations (called *ring width* in the next sections) observed during the cyclic growth. Finally to study the feature of pattern formed by dislocations at the SiGe/Si interface it was exploited the capabilities of dislocation dynamics, properly adapted to run simulation in nanostructures.

5.1 Circular dislocations in SiGe/Si(001) islands

Here we introduce a simple analtycal model that is able to predict correctly the spacing between tree-rings structures measured by AFM . Except for the nucleation of the first few dislocations, which are strongly influenced by the island shape, the model predicts self-ordering of dislocations inside SiGe islands in a regularly spaced network. The model presented here can be used as a non destructive tool, with respect to selective etching techniques, to give estimates of the number of dislocations contained in SiGe islands, on the basis of the experimental island volume, when the Ge content is known.

5.1.1 Tree-rings measurement

In order to analyze the composition and the periodicity of plastic events in multiply dislocated islands with increasing amount of deposited Ge, a more straightforward method, rather than X-ray diffraction and TEM, is to map the footprints of the islands in the Si substrate, after selective etching of all the SiGe material [120, 40, 121]. Ad Hoc sample growth was carried out by solid source MBE depositing of 15 ML Ge, at a substrate temperature of either 620°C or 740°C. With these growth parameters both coherent and plastically relaxed islands are observed on the surface [54, 122]. After etching selectively SiGe islands,Such etc The surface morphology was then imaged by Atomic Force Microscopy (AFM), revealing stepped-ring structures left below plastically relaxed islands. Such observed structures are produced during the island cyclic growth, as mentioned in Sec 1.6. As the increase of

strain in the island proceeds with Ge deposition by accumulation of material at the top, a progressively deeper trench in the Si substrate at the perimeter of the island base is carved. After selective SiGe etching, this stage corresponds to a short steep profile in the AFM scan of the Si substrate. As the critical conditions for one dislocation nucleation are met, sudden lateral expansion of the island has been observed [52], providing a full coverage of the trench bottom line. This stage corresponds to a small plateau in the etched samples. Periodic repetition of these two stages gives rise to a clear stepped profile in the Si substrate, which appears in form of concentric grooves in the AFM images [54]. Since it is well known that AFM measurements may be affected by artifacts due to the finite size of the probe [123, 124], the sample with islands grown at high temperature was also imaged by a Carl Zeiss Orion PlusTM helium-ion microscope (HeIM).

A representative HeIM scan and an AFM image of the tree-ring structure below dislocated islands in the sample grown at 740°C are shown in Fig. 5.1 (a) and 5.1 1(b), respectively. As described above, the footprints left on the surface consist of a central Si plateau surrounded by a staircase of several nearly concentric rings. From the microscopy images, we measured the distances between subsequent rings (ring width), starting from the central plateau and moving towards the periphery of the islands along two orthogonal directions. The first value of ring width corresponds to the lateral expansion of the island base after the introduction of the first dislocation, so that we expect some variation in size and in symmetry (off-centered ring [54, 125]) related to the different conditions occurring at the very first plastic event (see below). Figures 5.1 (c) and 5.1 (d) display the average ring width measured over many islands for two different growth temperatures. The AFM results are shown in black circles, while the values obtained by HeIM are shown in red squares. The two independent measurement techniques (see Fig. 5.1 1(d)) yield fully consistent results. It can be concluded that, within our growth conditions, the ring width shows a slight decrease from the island center to the island borders, in the range of ∼20 to ∼10 nm for the sample grown at 620°C and between ∼30 and ∼20 nm for the sample grown at 740°C, converging to an almost constant value, 15 and 22 nm, respectively, for the two samples. The average island Ge composition determined using AFM is X ∼0.36 and X ∼0.48 at 740 °C and 620°C, respectively.

5.1.2 Modeling of circular dislocations

In order to interpret the experimental findings of the previous section , we exploited an analytical approach to the study of multiply dislocated islands. This simple approach fully captures the essential features of the system, providing a fast tool to calculate, with a thermodynamic criterium, the critical island size at different stage of cyclic growth. Closed circular dislocations were approximated by the sum of 60° type misfit segments in [110] and in the [$\bar{1}$10] direction (for high growth temperatures, as used here, commonly observed dislocations are of 60° character [52, 126]). The dislocation is supposed to nucleate right at the perimeter of the growing island. While the real dislocation microstructure (60° misfit segments along the [110] and the [1$\bar{1}$0] direction and their threading arms which together form a regular pattern of concentric circles) is more complex, our geometrical simplification seems to reproduce the main features of the dislocation network analyzed in Ref [55].
By considering a $Si_{1-X}Ge_X$ island with an aspect ratio ρ, estimated as in Ref [40], an analytical expression for the misfit strain energy stored in the island and in the substrate can be formulated in a similar way as for the case of a continuous film [112, 127]:

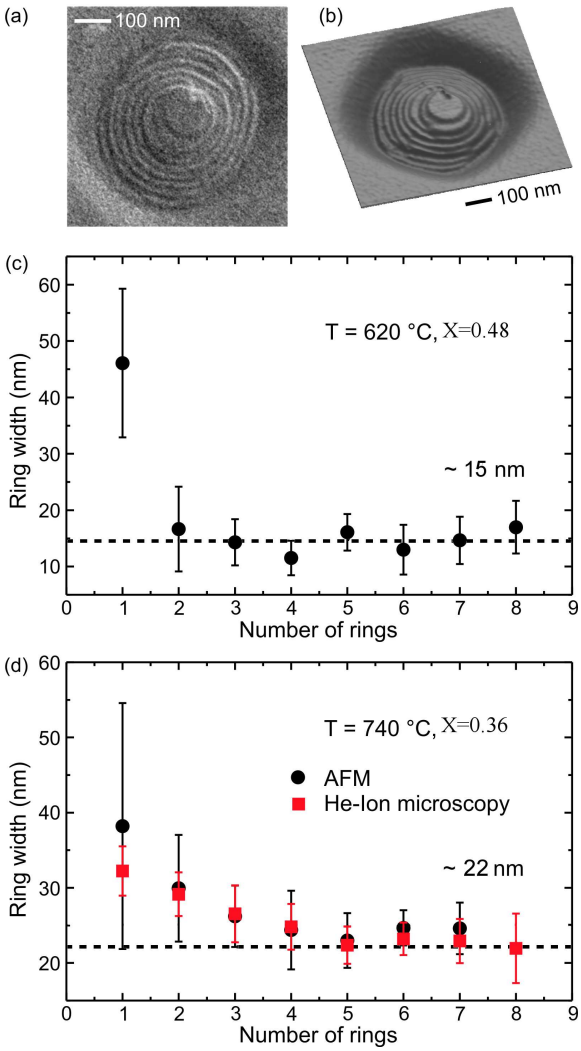

FIGURE 5.1: He-ion image of the Si surface obtained after removal of a dislocated SiGe island grown at 740°C showing a characteristic ring structure. (b) 3D view of an AFM image of a similar ring structure (the depth of the trench around the tree-ring is about 16 nm). (c), (d) Statistical analysis of the ring width as a function of number of rings obtained from AFM and He-ion microscopy images of several islands growth at 620°C (c) and 740°C (d). The average Ge content was estimated to be X=0.36 at T=740°C and X=0.48 at T=620°C, using AFM

TABLE 5.1: Model parameters for three different island shapes and aspect ratio ρ. The quantities a(ρ) and b(ρ) determine the relaxation function F(ρ, X) in Eq. 5.2, while the coefficient B(ρ) is defined as the ratio V/r^3, where V and r are the island volume and base radius, respectively.

	ρ	a(ρ)	b(ρ)	B(ρ)
Dome	0.2	0.505	0.0388	0.5229
Barn	0.3	0.317	0.0297	0.8362

$$W_0 = \frac{G}{1-\nu} F(\rho, X)(\varepsilon_{xx}^2 + 2\nu\varepsilon_{xx}\varepsilon_{yy} + \varepsilon_{yy}^2)V \tag{5.1}$$

where G is the shear modulus, ν is the Poisson ratio, ε_{xx}, ε_{yy} are the in-plane strain tensor components, V is the island volume, and $F(\rho, X)$ is the reduction factor of the elastic energy stored in the three-dimensional (3D) island and substrate, as compared to the flat film case. Here $F(r, X)$ was numerically evaluated for different island shapes and compositions by Finite Element Method (FEM). In particular, $F(\rho, X)$ is given by the ratio between the elastic energy stored in island and substrate divided by the island volume and the elastic energy density in a biaxially strained two-dimensional layer. $F(\rho, X)$ decreases significantly when ρ increases. It also depends on the Ge content X, because we linearly interpolate Si and Ge isotropic elastic properties to compute the elastic constants of $Si_{1-X}Ge_X$ alloys:

$$F(\rho, X) = a(\rho) \ + b(\rho)\ X. \tag{5.2}$$

The values of $a(\rho)$ and $b(\rho)$ evaluated for islands with different shape and aspect ratio, are given in Tab. 5.1. Notice that in this analytical model islands are approximated by,as show in Fig. 5.2, a cylinder with equal base area and volume

The realistic geometries are used to define the relaxation function $F(\rho, X)$ and the ratio V/r^3, where V and r are the island volume and base radius, respectively. The decrease in energy (E_{gain}) due to the misfit strain reduction provided by a new n-th dislocation is $E_{gain}^{(n)} = W_{n-1} - W_n$, where

$$W_n = \frac{G}{1-\nu} F(\rho, X) \left(\varepsilon_{yy}^2(n) + 2\nu\varepsilon_{xx}(n)\varepsilon_{yy}(n) + \varepsilon_{yy}^2(n)\right) V \tag{5.3}$$

is the elastic energy stored in an island when n dislocations are present. We considered the x and y axis parallel to the [110] and the [-110] directions, respectively, and $\varepsilon_{xx}(n) = \varepsilon_{yy}(n) = (f - \varepsilon_{disl}(n))$ are the in-plane strain components corresponding to the lattice misfit f, as reduced by the presence of n circular dislocations by $\varepsilon_{disl}(n)$. Due to the circular shape of the dislocations in our simplified model, each dislocation segment can be interpreted as relieving $b_{eff}/2$ on the average, along the two orthogonal strain components, multiplied by an effective linear density of dislocations $\left(\sum_{i=1}^{n} \frac{\lambda_i}{\pi R^2}\right)$, where $\lambda_i = 2\pi R_i$ is the length of each dislocation nucleated at a different island base radius R_i. This simply means that, on the average, half dislocation length is parallel to the [110] direction and reduce the ε_{yy} strain tensor component, while half dislocation length is parallel to the $[\bar{1}10]$ direction and relax the ε_{xx} component.

R is the actual island base radius, $b_{eff} = b\cos(\pi/3)$ is the effective Burgers vector for a 60° misfit dislocation with Burgers vector $b = a_{SiGe}\sqrt{2}/2$ and λi is the length of each dislocation. Thus, the island misfit is reduced by $\varepsilon_{disl}(n) = \left(\frac{b_{eff}}{2} \sum_{i=1}^{n} \lambda_i/(\pi\ R^2)\right)$ in

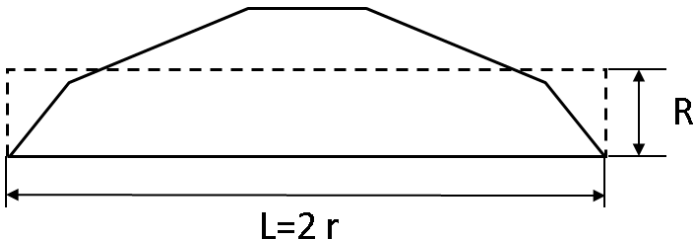

FIGURE 5.2: Schematic representation of a barn-like island (solid line), which is approximated in the analytical model by a cylinder (dashed line) of equal base size $L = 2r$ and volume. The cylinder height is chosen as the cut off radius R.

presence of n circular dislocations. A second contribution to the total energy is the cost related to the lattice distortion provided by the dislocation itself. $E_{self}^{(n)}$ can be analytically calculated as for the case of a flat film [9], by considering again that each segment of the circular loop is decomposed into two components, along the x and the y directions. In this case

$$E_{self}^{(n)} = \lambda_i G \frac{(1 - \nu \cos^2 \beta) b^2}{4\pi(1-\nu)} \ln \frac{\alpha R_{cut-off}}{b} \tag{5.4}$$

where β is the constant angle between each dislocation component and b, α is the parameter taking into account the atomistic core energy (usually set to 2.7[22]). $R_{cut-off}$ is the cut-off radius is the cut-off radius of the dislocation strain field, i.e. the average distance of the dislocation line from the free surface, taken as the height of a cylinder equal in volume and in base area to the island [112],as shown in Fig. 5.2 (d):

$$R_{cut-off} = V/(\pi \cdot R^2) \tag{5.5}$$

But for the first dislocation, an additional increase in energy due to dislocation formation is also given by the interaction energy between the n-th dislocation and the other $(n-1)$ dislocations already present in the island, here taken as the sum of the well established pair-interaction energies between straight dislocation segments located near a free surface [128]:

$$E_{int}^{(n)} = \sum_{j=1}^{n-1} \frac{(\lambda_n + \lambda_j)}{2} E_I(d_{n,j}) \tag{5.6}$$

where

$$\begin{aligned} E_I(d_{ij}) = \frac{G\, b^2 \sin^2\beta\, \sin^2\varphi}{4\pi(1-\nu)} \left(\ln(4\mathrm{a}^2+1) - \frac{4\mathrm{a}^2(12a^2+1)}{(4\mathrm{a}^2+1)^2} \right) + \\ + \frac{G\, b^2 \sin^2\beta\, \cos^2\varphi}{4\pi(1-\nu)} \left(\ln(4\mathrm{a}^2+1) + \frac{4\mathrm{a}^2(4\mathrm{a}^2+3)}{(4\mathrm{a}^2+1)^2} \right) + \\ + \frac{G\, b^2\, \cos^2\beta}{4\pi(1-\nu)} \ln(4\mathrm{a}^2+1) \end{aligned} \tag{5.7}$$

Here d_{ij} is the separation distance between dislocations, $a = \frac{R_{cut-off}}{d_{ij}}$, and j is the angle between the glide plane of either the two components of the misfit segment and the vertical

[001] direction. Therefore, by summing the last two contribution into one "energy cost" term,

$$E_{cost}^{(n)} = E_{self}^{(n)} + E_{int}^{(n)} \tag{5.8}$$

the estimation of the critical island dimension for the nucleation of the n-th circular dislocation is obtained by numerically scanning the island base radius R until $E_{cost}^{(n)}$ is equal to $E_{gain}^{(n)}$. It should be noted that the change in the average Ge composition X of the island affects both the misfit f and the elastic constants entering the two terms of Eq. 5.8. Since we assume that all the circular dislocations nucleate exactly at the island edge, the ring spacing (and the dislocation spacing) as a function of the number of dislocations in the island is obtained directly by subtracting subsequent critical base radii. In order to clarify the role of composition and aspect ratio, an analytical form of the ring width without the repulsive contribution (essentially a shift to higher values, see the following Sections) can be also obtained. In this case we first rewrite the gain components as:

$$\begin{aligned}\varepsilon_{disl}(n) - \varepsilon_{disl}(n-1) &= \frac{b_{eff}}{R}\left(\sum_{i=1}^{n}\frac{R_i}{R} - \sum_{i=1}^{n-1}\frac{R_i}{R}\right) = \\ &= \frac{b_{eff}}{R_n}\left(\frac{R_n}{R_n} + \sum_{i=1}^{n-1}\frac{R_i}{R_n} - \sum_{i=1}^{n-1}\frac{R_i}{R_n}\right) = \frac{b_{eff}}{R_n}\end{aligned} \tag{5.9}$$

and

$$\begin{aligned}\varepsilon_{\mathrm{disl}}^2(n) - \varepsilon_{\mathrm{disl}}^2(n-1) &= \frac{b_{eff}^2}{R^2}\left\{\left(\sum_{i=1}^{n-1}\frac{R_i}{R}\right)^2 - \left(\sum_{i=1}^{n}\frac{R_i}{R}\right)^2\right\} = \\ = \frac{b_{eff}^2}{R_n^2}\left\{\left(\sum_{i=1}^{n}\frac{R_i}{R_n} - 1\right)^2 - \left(\sum_{i=1}^{n}\frac{R_i}{R_n}\right)^2\right\} &= \frac{b_{eff}^2}{R_n^2}\left\{1 - 2\sum_{i=1}^{n}\frac{R_i}{R_n}\right\}\end{aligned} \tag{5.10}$$

By using a simplified functional expression for the island volume $V = BR^3$ (where B is given in Tab. 5.1) for islands with different aspect ratios, 0.2 (domes), 0.3 (barns)), we can rewrite equations (5.3) and (5.4) as follows:

$$E_{gain}(n) = 2G\frac{1+\nu}{1-\nu}F(\rho,X)B\left(2f\, b_{eff}R_n^2 + b_{eff}^2 R_n\left\{1 - 2\sum_{i=1}^{n}\frac{R_i}{R_n}\right\}\right) \tag{5.11}$$

$$E_{cost}(n) = 2\pi R_n G\frac{(1-\nu\cos^2\beta)b^2}{4\pi(1-\nu)}\ln\left(\frac{\alpha B}{b\pi}R_n\right) \tag{5.12}$$

The critical condition for the nucleation of a new dislocation is then $E_{gain}(n) = E_{cost}(n)$ and the critical island radius for n-th dislocation formation is:

$$R_n = \frac{b_{eff}}{f}\sum_{i=1}^{n}\frac{R_i}{R_n} - \frac{b_{eff}}{2f} + \frac{(1-\nu\cos^2\beta)}{8(1+\nu)F(\rho,X)Bfb_{eff}}b^2\ln\left(\frac{\alpha B}{b\pi}R_n\right) \tag{5.13}$$

Therefore, the ring width reads :

$$\begin{aligned}w_{n-1} = R_n - R_{n-1} = \frac{b_{eff}}{f}&\left(\sum_{i=1}^{n}\frac{R_i}{R_n} - \sum_{i=1}^{n-1}\frac{R_i}{R_{n-1}}\right) + \\ &+\frac{(1-\nu\cos^2\beta)}{8(1+\nu)\,F(\rho,X)Bfb_{eff}}b^2\ln\left(\frac{R_n}{R_{n-1}}\right)\end{aligned} \tag{5.14}$$

For sufficiently large n values, as we verified numerically,

$$\left(\sum_{i=1}^{n}\frac{R_i}{R_n}-\sum_{i=1}^{n-1}\frac{R_i}{R_{n-1}}\right)\rightarrow\frac{1}{2}$$

and $R_n/R_{n-1}\rightarrow 1$, so that the ring width converges to $b_{eff}/(2f)$and all information concerning the island is lost. Such a result is not unexpected. In fact, in the continuous film case, the equilibrium density fully balancing the misfit along the [110] or the [-110] direction is f/b_{eff}, which corresponds to a dislocation spacing of b_{eff}/f. In our model, each dislocation segment relieves $b_{eff}/2$ along the two orthogonal directions [110] and [-110], so that the dislocation distance in the limit of very large islands corresponds to $(b_{eff}/2)/f$.

5.1.3 Model prediction vs. experiment

Following the previous analysis of Ref. [56], we shall assume a barn shape for the dislocated islands, thus fixing the aspect ratio to ρ=0.3, in agreement with the average value indicated by AFM measurements [40]. In particular, we report in Fig. 3(a) how the critical condition, Eq. 5.8 is periodically satisfied by increasing the dislocation number and island base radius for a barn with X=0.36 (black arrows), corresponding to the average value experimentally determined for samples grown at T=740°C.

From the left to the right in Fig. 5.3 (a), the solid curves (blue online) give the E_{gain} terms calculated increasing the number of dislocations from 1 to 5 as a function of the island radius. Similarly, the dashed curves (red online) give the E_{cost} terms obtained varying the dislocation number from 2 to 5 (from left to right), while the dotted line (green online) represents the E_{self} term. This curve increases monotonically because E_{self}, (see Eq. (4)), depends just on the last dislocation length λ_n and on the cut-off radius $R_{cut-off}$, which in our model are both directly proportional to the island radius R. The first dislocation is nucleated when $E^{(1)}_{self}$ (dotted line) is equal to $E^{(1)}_{\rm gain}$ (first solid line left), while all the others are nucleated when $E^{(n)}_{\rm cost}$ (dashed lines), including both the self energy and the repulsive term, crosses $E^{(n)}_{\rm gain}$ (solid lines). We note that the radial spacing between dislocations decreases to a nearly constant value, and that the repulsive term contributes significantly to the spacing. These issues are better seen in Fig.5.3 (b), where we report the ring width between two plastic events vs the increasing number of rings for the same system, calculated with (solid line with boxes) and without (dashed line with circles) the interaction term. We see that the solid curve correctly reproduces the experimental trend observed at 740°C, as reported in Fig. 5.1(d), and converges to the ring width value of 22 nm, which is the experimental indication. The dashed curve obtained neglecting the repulsive term is shifted by a nearly constant value far below this experimental data, outside the relative error bar (grey band in Fig. 5.3 (b)). The results in Fig. 5.3 show that the ring width initially decreases with the dislocation number, but after the nucleation of the very first dislocations the spacing between two subsequent circular dislocations becomes almost constant. The shape and the size of the island clearly affect the early plastic events, dislocations interact with free surfaces and with each other in small volumes, so the spacing between loops is larger than the value provided by the theory for continuous film case [9]. Increasing the island radius the size effect is lost and the plastic relaxation events occur periodically. With or without the dislocation interaction, the calculation gives qualitatively the same behavior, but quantitatively different results, as highlighted in Fig. 5.3(b). Hence

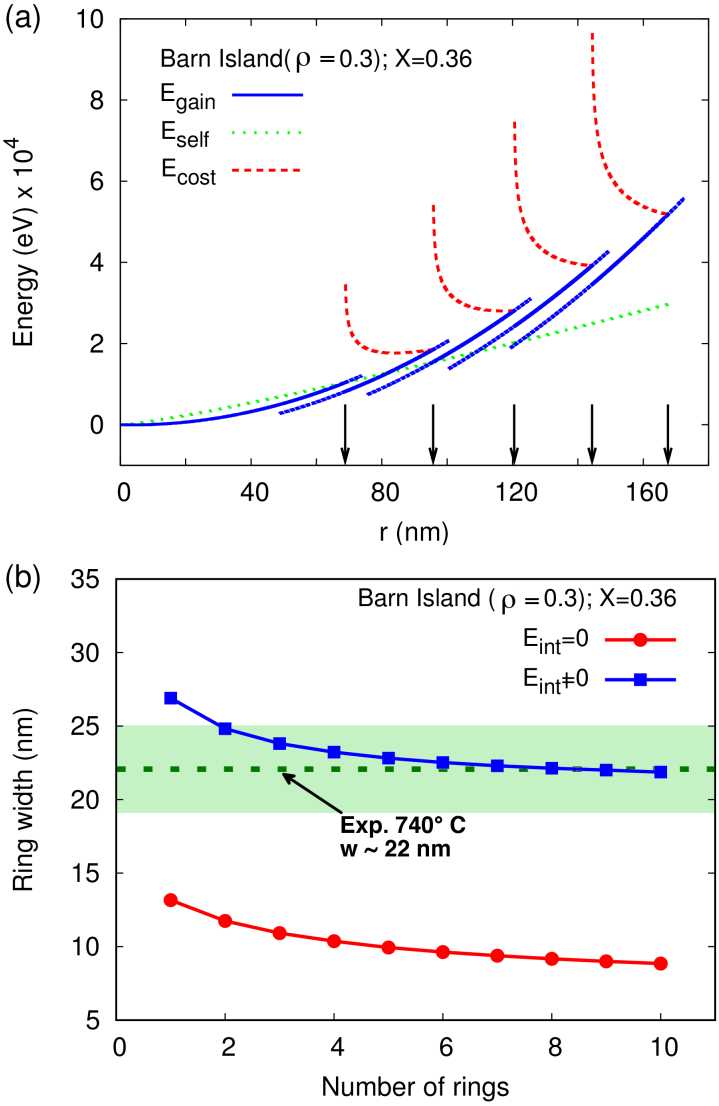

FIGURE 5.3: Results for barn-shaped islands (ρ=0.3), and Ge concentration X=0.36, corresponding to the experimental data at T=740Â°C. (a) Critical radii (arrows) for dislocations nucleation. The first critical radius is determined by the intersection of E_{gain} (solid, blue curve) and E_{self} (dotted, green curve), which is the only energy-cost term. Subsequent critical radii are also influenced by dislocation-dislocation interaction (E_{int}). Plastic relaxation therefore occurs at the intersection between E_{gain} and the total energy cost E_{cost} (dashed, red curve), i.e. the sum of E_{self} and E_{int}. (b) Distance between dislocations (ring width) versus the number of rings, with (full boxes, blue) and without (full circles, red) including the E_{int} term. The ring width saturation value at T=740°C is reported using a dashed line within a shaded rectangle representing error bars

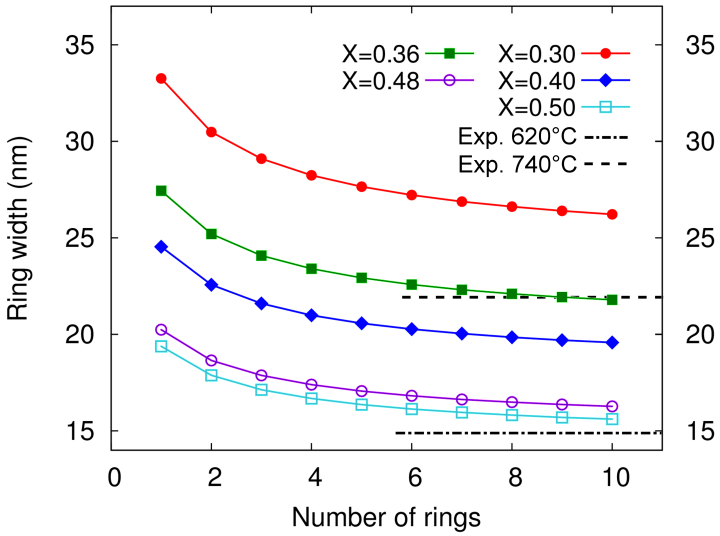

FIGURE 5.4: Rings width at different Ge content for a barn island (ρ=0.3). Experimental results at both 740°C and 620°C are nicely predicted, considering uncertainties in both concentration estimates and ring widths (see text)

the dislocation interaction cannot be neglected in the thermodynamic balance if we want an accurate prediction of the critical island radii and dislocation spacing.

As one should expect, increasing the Ge content inside the island the elastic energy stored in the system is also increased and the dislocation spacing becomes smaller with the increasing misfit. In fact, by tuning the island Ge content X from 0.3 to 0.5, as reported in Fig.5.4 , a downward shift and flattening of the ring width curve is obtained, in agreement with the experimental trend observed by decreasing the growth temperature, outlined by Fig. 5.1(c) and 5.1(d). In particular, we observe that at any Ge concentration the ring width quickly converges to a nearly constant value, which is lower for higher island Ge content. Together with the theoretical calculations at different island Ge concentrations we plotted in Fig. 5.4 the saturation ring width values (dashed lines) for the two growth temperature examined in this work. Comparing the experimental ring width values with the theoretical curves in Fig. 5.4, we see a good agreement between the ring width measured at 740° and 620° and the curve obtained for X=0.36 and X=0.48, respectively. The predicted value for X=0.48 is slightly larger than the experimental one, but still in the error bar range shown in Fig. (c).

Notice that the variation in the ring width saturation values with the island Ge content becomes larger when the Ge composition is low, while at high Ge content we observed small changes between the different predicted values. For instance, changing the island composition from X=0.3 to X=0.4 leads to a decrease in the converged ring width value of about 7 nm, while the ring width variation obtained by changing X between 0.4 and 0.5 is only 4 nm. We can conclude, by looking at the critical radius differences, that the model is more sensitive in describing diluted SiGe islands. Our agreement between the experiments and the model predictions makes the latter of direct use for estimating the number of dislocations in the islands without performing selective etching, whenever the average composition is known. In Fig. 5.5, the critical island volumes for the introduction of the n-th dislocation is plotted as a function of the dislocation number for different concentration values.

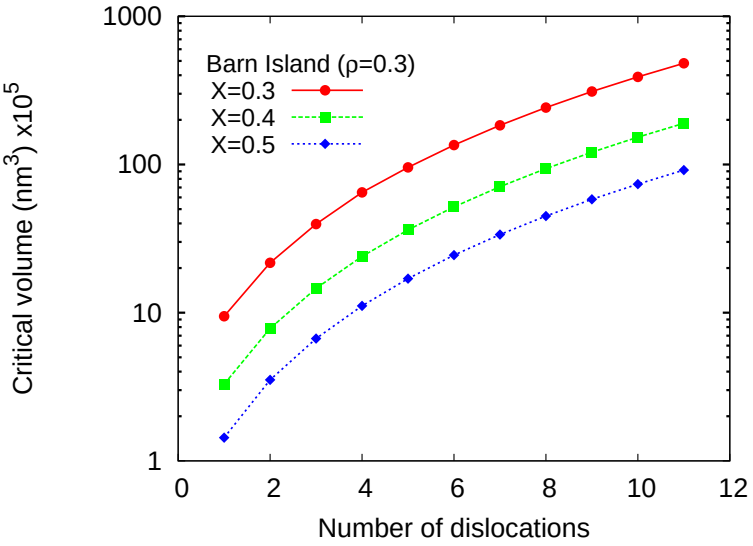

FIGURE 5.5: Critical volume estimation for island of different Ge content (X=0.3, X=0.4, X=0.5)

At variance with the ring width, the predicted critical volumes significantly increases with the dislocation number. Thus, the critical volume for plastic relaxation events is a sensitive parameter that can be exploited for estimation of the dislocation number contained in islands. Moreover, the predicted critical volumes can be directly compared with barn volumes measured by AFM allowing dislocation number estimation with no need to perform selective etching, which is a destructive technique.

5.2 Dislocation Dynamics in 3D nanostructures

Experimental observation has revealed the formation of dislocation patterns at the interface between island and substrate during relaxation. While the method developed and described in sec. 4.2 allows for the analysis of static configuration of 3D misfit dislocations, to determine the pattern formation at the $Si_{1-x}Ge_x$ interface a dislocation dynamics (DD) code is needed. DD is necessary to take into account interactions and reactions that occur during dislocation propagation. We chose a DD code originally developed at the LEM [1] laboratory, called microMegas (mM). The code is a powerful tool to study the final microstructure formed by dislocation motion in bulk material, in the following we described howwe adapt microMegas to tackle nanostructures.

5.2.1 Brief overview of microMegas

microMegas is an open source DD code to study plastic behavior of crystalline materials using the classical theory of dislocation. The peculiarity of the code is that both time and space are discretized. The time is discretized as in usual molecular dynamics simulation. The space is discretized into a lattice that is homothetical with respect to the lattice of the crystalline material (hcp,fcc,bcc,..).

[1] Laboratoire d'Etudes des Microstructures, CNRS-ONERA, 92322 Chatillon cedex,France

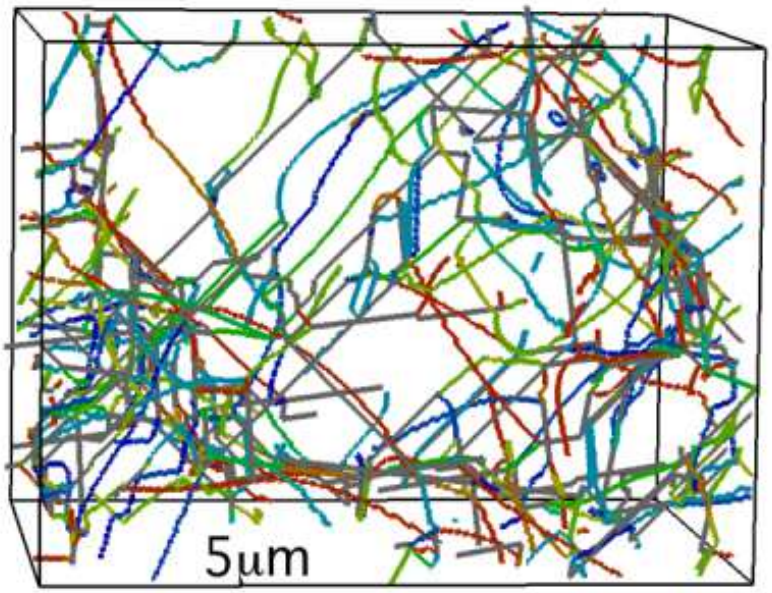

FIGURE 5.6: Example of microMegas output: dislocation microstructure in bulk system.

By scaling the simulation lattice it is possible to describe systems in the nanometer-micrometer range. For a given distribution of dislocations the code simulates the propagation and the reaction of the line defects due only to the glide phenomenon, in Fig 5.6 an example of a typical output of simulation is shown. In this section we describe the main feature of the code, focusing our attention on fcc lattice, used to run simulation with Silicon and Germanium.

5.2.2 Dislocation line discretization

Continuum dislocation lines are described as the sum of elementary straight segments (see 5.7). There are 8 elementary segments (two screw,two edge and four $\pm 60^\circ$ character in fcc) for each slip system (three slip systems per glide planes) of the chosen crystalline structure, as it is shown in Fig.5.7 (a). The lenght of elementary segments depends on the dimension of the parameter of the simulation lattice. In the code, when the elementary cell has exactly the size of the real lattice a the lenght of the elementary screw dislocation is exactly the modulus of the Burgers vector. Fig.5.7 (b) highlights how the combination of elementary segments provides a description of a continuum dislocation line (orange line). Scaling down the elementary cell of the simulation lattice the discrete description of the dislocation line converges to the continuum one.

Force and displacement

DD simulation as molecular dynamics simulation are driven by the rules of classical mechanics. To compute the displacement of each dislocation segment we need to know the effective force τ_{eff} acting on it. As in the classical dislocation theory [98], the forces acting on a straight segment i is given by the sum of two contribution: Peach and Koehler (PK) force F^{PK} and a local line tension correction τ_L. the former, PK force, is the force acting

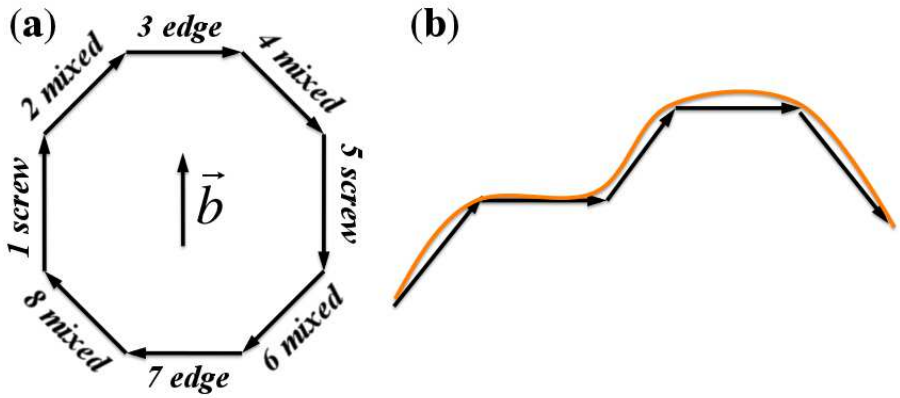

i

FIGURE 5.7: Elementary dislocation segments used to discretize a real dislocation line (a). There are 8 elementary segments for each glide plane of the chosen structure (fcc,bcp, hcp..). In panel (b) sketch of how the sum of elementary segments approximates a continuum dislocation line.

on a dislocation segment due to external stress field. The source of the external stress field is of two characters. The first one is σ_{app}, the stress applied to the system. In our case, it is the stress field computed by FEM inside the analyzed nanostructure. The second one σ_{int} is the stress acting on segment i due to the presence of the other dislocations in the crystals. In particular in microMegas it is calculated with the formulation given in ref. [129]. Once we defined the two quantities the expression of PK force becomes:

$$F^{PK} = (\sigma_{app} + \sigma_{int}) \cdot \vec{b} \times \vec{l} \tag{5.15}$$

where $\vec{b}$ and $\vec{l}$ are respectively the Burgers vector and the dislocation line direction of straight segment i. The vector F^{PK} usually does not necessary belong to the glide plane of the segment i. In order to compute the component of force (F^{PK}_{eff}) really effective on dislocation displacement the F^{PK} has to be projected on the segment glide plane. The latter term, the local line tension correction, comes from the fact that during discretization process curved dislocations line sections are locally replaced by straight segments. Hence, an additional force on straight segments must be added in the simulations to account for such decrease of the elastic energy imposed by discretization process. This correction is made thank to the usual concept of line tension[98]. In the result shown in 5.2.5 we used the expression of line tension derived by Foreman [130]. The total effective force acting on the straight segment i in the glide plane is:

$$\tau_{eff} = F^{PK}_{eff} + \tau_L \tag{5.16}$$

Once computed τ_{eff} it is possible to calculate the dislocation velocity using a simple mobility law:

$$v = \frac{\tau_{eff} b}{B} \tag{5.17}$$

where B is the viscosity coefficient. Expression 5.17 is a simple velocity equation commonly used in DD simulations to account for the dislocation-phonon interactions that take

place during dislocation glide and at the origin of dissipation phenomena. Neglecting inertial effects (dislocation mass is small and the line energy very large), the updated position associated to segment i is calculated with the explicit Euler forward method:

$$x_i(t) = x_i(t - \Delta t) + v\Delta t \tag{5.18}$$

where $x_i(t)$ is the position at the time t and Δt is the time step chosen to run the simulation. No lattice friction (resolved shear stress needed to initiate the motion of dislocation) was considered in the present simulation, because in fcc materials, and in SiGe system when the applied stress is larger than 1 GPa, its contribution is negligible. In the following simulations the time step was set to about $1 \times 10^{-}14$ s. The glide motion of dislocations, because of the large applied stress level in the island, is very quick, so small time step is needed to observe the propagation and interactions of gliding dislocations.

Interactions between dislocations

An important part of microMegas is devoted to search any possible reaction between a gliding segment and other segments or obstacles. In fact if during its motion a segment encounter other segments or obstacles, the displacement $v\Delta t$ predicted by Eq. 5.18 is reduced to the collusion distance. Special criteria called *local rules* are applied in order to account for the possible reaction between the line defects (formation of junctions, collinear annihilation, self annihilation, Hirth lock).

Cross-slip

Cross-slip is a mechanism who allowing screw dislocations to change glide plane. In fact to cross-slip dislocation line must belong both the primary glide plane (the glide plane in which dislocation is moving) and the called cross-slip plane (the plane in which dislocation will move after the cross-slip event); only screw segments have this properties. This mechanism is usually driven by dislocation core properties, not by elasticity, and it is modeled in microMegas using a stochastic rule [131]. As explained in more details in section 5.2.4 in case of SiGe islands because of high stress, cross-slip is mostly mechanically activated.

5.2.3 How to adjust mM to tackle heteroepitaxial nanostructures

mM is a robust tool to study evolution of plasticity in bulk system, as listed in previous sections, it could manage all the physical interactions occurring to dislocations during their motion. The heteroepitaxial nanostructures treated in this work (thin film and 3D islands) are objects with several free surfaces, threading arms cannot be neglected in studying dislocations propagation. To adapt the code to face our problem, we addressed the possibility of describing the motion of threading arms (dislocations terminating on a free surface). The problem of calculating elastic field of dislocation touching free surfaces, and the force acting on it, is out of hand using the classical elasticity theory. To reach this goal we introduced a physical approximation firstly described in Ref. [98] and then applied in Ref. [132].

Two terms concur to determine dislocation-surface interaction. The first contribution is arising from image construction and try to turn the segment normal to the surface. The second one is, as in bulk system, the tendency of a dislocation to rotate into screw direction. Taking into account both term, the force acting on segment touching a free surface (sketched in Fig. 5.8) is:

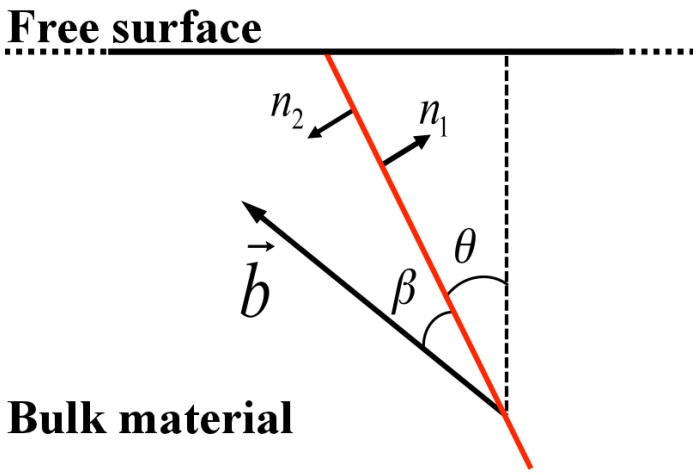

FIGURE 5.8: Projection on glide plane of dislocation segment (red line) touching free surface (black horizontal line). Two force terms act on a segment touching the surface. The first one, arising from images force and depending on θ, tries to rotate the dislocation to be normal to the surface, The second one, depending on β, tries to rotate the segment to be parallel to the Burgers vector.

$$\tau^{fs} = \frac{1}{\lambda}\frac{\mu b^2}{4\pi(1-\nu)}[\hat{n}_1|(1-\nu\cos^2\beta)\tan\theta| + \hat{n}_2|(2\nu\cos\beta\sin\beta)| \tag{5.19}$$

where, as described above, the first term in the parentheses acts to rotate the line so that it is normal to the surface (in the glide plane), while the second term acts to align the dislocation with the Burgers vector. Here λ is the distance from the point at which the force is applied and the point at which the line intersects the surface (the solution of elastic field is diverging exactly at the intersections between dislocation segment an the surface), and it is a parameter to be tuned in the simulation. We run simulation to set λ in order to reproduce the critical thickness of flat films as calculated in Ref [9]. In the expression defining th force acting on a straight segment touching the surface the line tension correction is replaced by Eq. 5.19.

5.2.4 Cross-slip criterium at high stress

Cross slip as described in Sec. 5.2.2 is a thermally activated process. In semiconductor as Si and Ge, the Peierls stress (stress needed to move dislocations at 0 K) is about 1 GPa [133]. When the applied stress σ_{app} is larger than the Peierls stress some process as cross-slip can be considered athermal [134], depending only on the effective stress acting on dislocations. In areas close to the interface and the corners of the SiGe islands the stress field exceeds the Peierls stress. To take into account this effect in the simulation, we introduce a local rule for cross slip event: if the effective stress is larger than 1GPa and the effective stress in the cross-slip plane τ_{eff}^{CS} is larger than the effective stress τ_{eff} in the glide plane, cross slip can take place (mechanical activation). In order to avoid ineffective cross slip event (segments moving back and forth between cross slip plane and glide plane without any real effect on dislocations microstructure), we added a critical stress criterium depending on the lenght of segment, as described in Ref. [130]:

$$\tau_c = \frac{\mu b}{2\pi} \log\left(\frac{L}{b}\right) \tag{5.20}$$

where L is the lenght of the dislocation screw segment involved in the cross slip event. Summarizing the rule for having mechanical activated cross slip is:

$$\begin{cases} \sigma_{app} > 1GPa \\ \tau_{eff}^{CS} > \tau_{eff} \\ \tau_{eff}^{CS} > \tau_c \end{cases} \tag{5.21}$$

5.2.5 Results

The ad-hoc modifications introduced on the mM simulation code allow for handling the motion of threading dislocations and for studying cross-slip event at high stress (> 1 GPa) in nanostructure. Hence the code is suitable to study the time evolution and interaction of dislocations. Still we have to define where nucleation events occur in nano islands. In fact DD code can study dislocation propagation, starting from given dislocations sources. FEM analysis can be exploited (once again) to identify the nucleation sites, computing the resolved shear stress (RSS) in the system.

Island shape and elastic properties

We modeled the onset of plastic relaxation (dislocation nucleation) in barn shaped islands. After the first plastic event, cyclic growth is observed, island changes from barn (ρ=0.3) to superdome (ρ=0.25) shape. To address the behavior of dislocations beyond the plastic relaxation onset we run simulations using the Superdome geometry 5.9. Superdome islands (shown in Fig. 5.9) have the same set of exposed facets than domes. The different extension of facets causes the difference in aspect ratio. Chosen the Reuss average isotropic elastic constants [98] for Si and Ge (they were used both in DD code and in FEM calculations to be consistent) we decided to study (as described in the following sections), island with Ge content of 40 %, to fit the condition of experimental TEM observation (islands grown at about 650° C). In DD simulation cell, only superdome is reproduced, because only the determination of the applied stress inside the island is needed to describe the dynamic of dislocations. The substrate influence is considered in FEM calculations to determine the elastic field in the nanostructure, then the stress field solution determined in the island with finite element calculation is applied to the DD simulation. In the latter simulations the SiGe/Si(001) interface is modeled as a barrier (dislocations can not cross it) at which, in our case, dislocations can deposit. The segments deposited at the interface are 60° misfit segment.

Nucleation sites analysis

Nucleation sites are important to determine the distribution of dislocation sources in the system. Different source distributions generate different patterns, in particular when small volumes are considered. For instance in infinite flat films, dislocation multiplication is observed. New sources are generated by self interaction of running threading arms, so the final dislocation microstructure is not only related to the initial source distribution. On the contrary in small volumes threading arms are shorter and the dislocation mean free

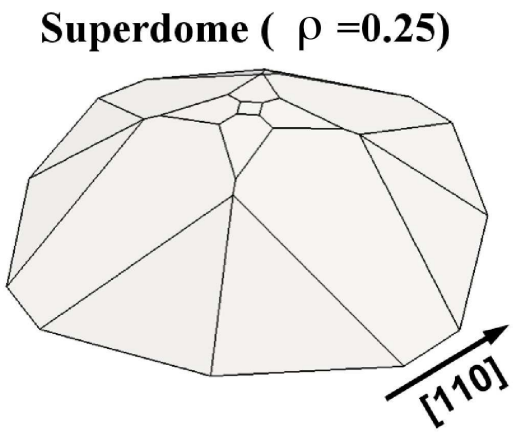

FIGURE 5.9: Sketch of the Superdome island (ρ=0.25) geometry used in the simulation.

TABLE 5.2: Slip system used to compute resolved shear stress and to run DD simulations in SiGe islands.

$\vec{b}$	Glide plane
$a/2[011]$	$(1\bar{1}1)$
$a/2[011]$	$(\bar{1}\bar{1}1)$
$a/2[0\bar{1}1]$	$(\bar{1}11)$
$a/2[0\bar{1}1]$	(111)

path is smaller. Then, interactions between line defects are less probable. A useful tool for determining sites of homogeneous nucleation is the RSS analysis on a given slip system. In diamond lattice, there are twelve activated slip systems (see App. B). In islands, the four slip systems with $\vec{b}$ in the (001) interface are not expected to be active, because they do not relax heteroepitaxial stress. The eight slip systems with Burgers vector out of the interface plane are symmetric by pairs with respect to the generated elastic field. For instance, using as a reference Fig. 5.10 (a), the slip system with $\vec{b} = a/2[011]$ and glide plane $(1\bar{1}1)$ is equivalent to the slip system with the same glide plane but with $\vec{b} = a/2[\bar{1}01]$. This rule of symmetry allows us for reducing at four the number of slip systems to be used in DD simulations (see Tab. 5.2).

Once determined the stress field of $Si_{0.6}Ge_{0.4}$ Superdome island using FEM, as depicted in sec. 2, the RSS associated to each of the four chosen slip systems can be calculated. As case study we started analyzing the RSS of the slip system reported in the first row of Tab. 5.2 and in panel (a) of Fig. 5.10. In panel (b) the RSS map is plotted on a cross-section parallel to the interface. Hence the upper right corner of the island shows the maximum values (dark red color). High value of RSS means, not only high effective applied stress but also high probability of homogeneous dislocation nucleation [98]. The upper right corner of the superdome is the most favorable site for dislocation loop nucleation of slip system drawn in Fig 5.10.

In addition, the RSS analysis allows for addressing the probability of observing mechanically activated cross slip. Fig. 5.11 shows the previously analyzed slip system (red plane) and its cross slip system (blue plane). Notice that both have the same Burgers vector. Let us call RSSgp the resolved shear stress for the primary system (red) and RSScs the resolved

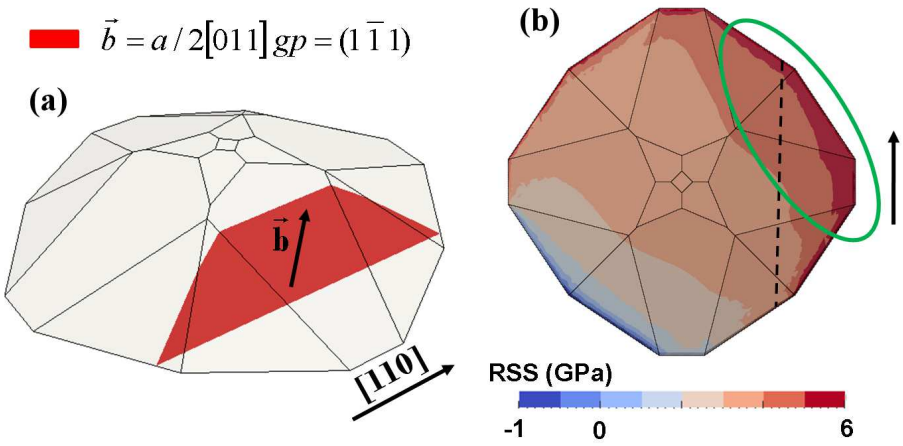

FIGURE 5.10: (a) Slip system with Burgers vector $\vec{b} = a/2[011]$ and glide plane $(1\bar{1}1)$ and its correspondent RSS (b). Due to the stress field of the island (computed by FEM) the resolved shear stress has maximum in the upper left corner of the superdome island (green elipse). This corner can act as site of homogeneous nucleation of dislocations.

shear stress for the cross slip one (blue). RSSgp and RSScs by itself give the effective applied force acting on line defects belonging to the red and blue plane respectively. The difference between them (RSSgp-RSScs) depicts the domain where mechanical activated cross slip events are expected to take place. In region where RSSgp is larger than RSScs, dislocation segment in the primary glide plane in Fig. 5.11 (b) can evolve from top to bottom following, for instance, the red dashed line. When the segment approaches the border where the color map changes from red to blue region, RSScs is larger than RSSgp. The propagation of dislocation segment is now favored in the cross slip plane. If the dislocation has screw character and fits all the requirement of Eq. 5.21 cross slip event ideally takes place if the lenght and curvature of threading dislocation is favorable. This last points are dependent on dislocation dynamics and must be investigated with DD simulations.

Dynamics of a single dislocation in SiGe islands

We tested the evolution of a dislocation loop belonging to the slip system analyzed in the previous section (sketched in Fig. 5.10). We chose a loop with a critical initial perimeter of total lenght of about 10 nm. The critical resolved shear stress to expand such loop is about 3.5 Gpa (stress needed to increase the diameter of the loop). The evolution of the dislocation loop is tested moving the starting position in the islands. The base of the island is 140 nm (just overcritical for Ge content of 40 %) and FEM stress field of the analyzed is used as source of applied stress. The result of the test is summarized in Fig. 5.12.

Panel (a) and (b) show the top view of a superdome island. In particular panel (b) highlights the behavior of the test loop in the island (moving the starting point of the loop, it should evolve running parallel to the black dashed line). In light blue region the tested seed loop does not evolve, the resolved shear stress in this region is not large enough to expand the loop so that the loop shrinks, annihilating itself. In the green area, even if the resolved shear stress has the maximum values, the seed loop is in this area systematically annihilated due to the strong dislocation-surface interaction. When the loop is placed close

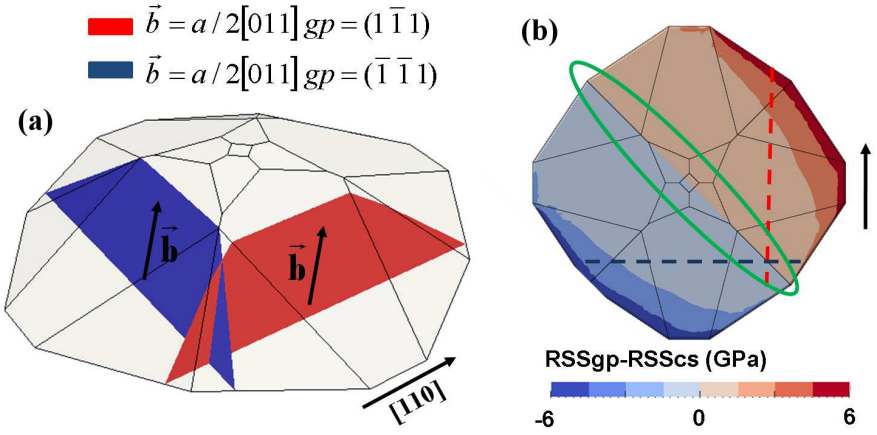

FIGURE 5.11: (a) Dislocation Primary glide system (red) and cross slip system (blue). (b) Probability to observe mechanically activated cross slip event in the system. When the difference between the resolved shear stress in the primary glide plane (RSSgp) and the resolved shear stress in the cross slip plane (RSScs) in the cross slip plane is smaller than zero, cross slip event could be observed.

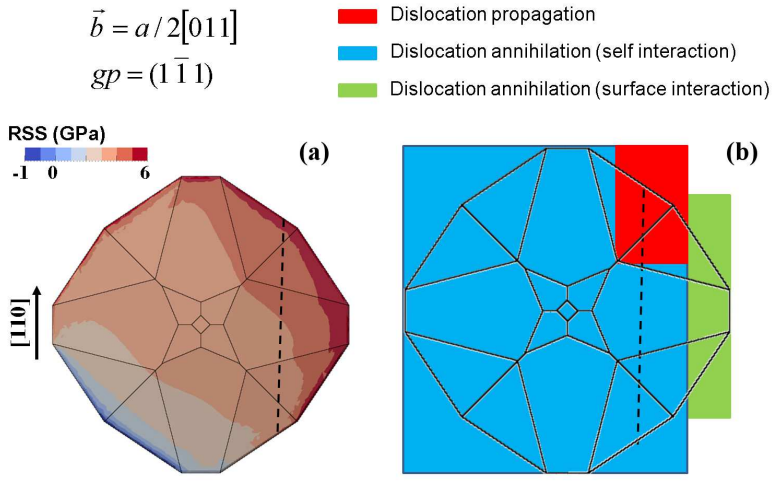

FIGURE 5.12: Map of propagation of a seed loop (size 10 nm) in a superdome island with base equal to 140 nm an Ge content of 40 %. (a) slip system of the tested loops. (b) Behavior of the dislocation loop for the four different slip system when placed in different initial position of the island.

to the island bottom edges, surface effect is still very strong due to the small dislocation-surface distance, and the dislocation loop is attracted to the surface without depositing misfit segment.

In the red area, dislocation seed loops are found to expand and to propagate in the island system, depositing a misfit segment parallel to the black dashed line. Placing the test loop in the red area its propagation is highlighted in Fig. 5.13 from panel (a) to panel (f). The dislocation starts to expand in the island, panel (a), touching the free surfaces (b). Threading arms are created and a 60° misfit segment is deposited at the bottom interface (001 oriented). Threading arms evolve following the contact surface force. In fact, comparing panel (c) and (d) the direction of the segment touching the surface changes when the superdome facet orientation change. In panel (f) the final equilibrium position is depicted: the misfit segment is deposited and the two threading arms point out from superdome facets. In such simulations no cross-slip events are detected: even if the left threading arm in panel (e) is oriented in the screw direction and the stress field in that region is favorable to cross slip event activation. Detailed analysis of the DD simulation results shows that cross-slip is not possible in the present case since, the lenght of threading segment is too short and con not be curved in the cross-slip plane. Finally we can notice how the final shape and position of a single dislocation, predicted by our dislocation dynamics simulation, are in agrrement with the results of Sec. 4.2. Figure 5.14 (a) shows the top view of the final result of dynamics depicted in 5.13 (e), while figure 5.14 (b) shows the 60 ° dislocation equilibrium position calculated using the thermodynamic criterion. The basis of the superdome island in panel (b) was set equal to 140 nm, as in DD simulations. By comparing Fig. 5.14 (a) with Fig. 5.14 (b) it is clear how the two different approaches lead to the same final equilbrium position. In particular we can highlight how the assumption made in Sec. 4.2 (to calculate the onset of plastic relaxation introducing a 60° straight dislocation segment in the island) was correct. In fact, the shape of the dislocations in panel (a) and (b) are similar, both of them show a long 60° straight segment deposited at the SiGe/si interface.

First stage of cyclic growth

The analysis performed in the two previous sections can be extended to the four active slip system. The result is shown in Fig. 5.15. By calculating the RSS and testing the propagation of different seed loops, we were able to define two active corners in the island (highlighted by different color in figure 5.15). Placing four loops (one for each active glide plane) in the two different active corner, we studied the general solution when plastic relaxation is expected to appear on several slip system.

We considered an island 160 nm large (larger island is needed to carry four dislocations) and Ge content of 40%. The steps to reach the final dislocation microstructure are described in the following. As illustrated in Fig. 5.16. The four loops expand, touch free surfaces and interact with each other,(panel (a)-(c)). Misfit segments are deposited and the final dislocation configuration is formed. Notice that, during their propagation dislocations are found in simulations to strongly interact, but no formation of junctions is observed. This, once again, is due to the fact that threading segments are too short, and junctions can not zip.

The final dislocation pattern provided by DD simulations looks like a square, with edges in $\langle 110 \rangle$ directions. The lenght of misfit segments are still predominant with respect to

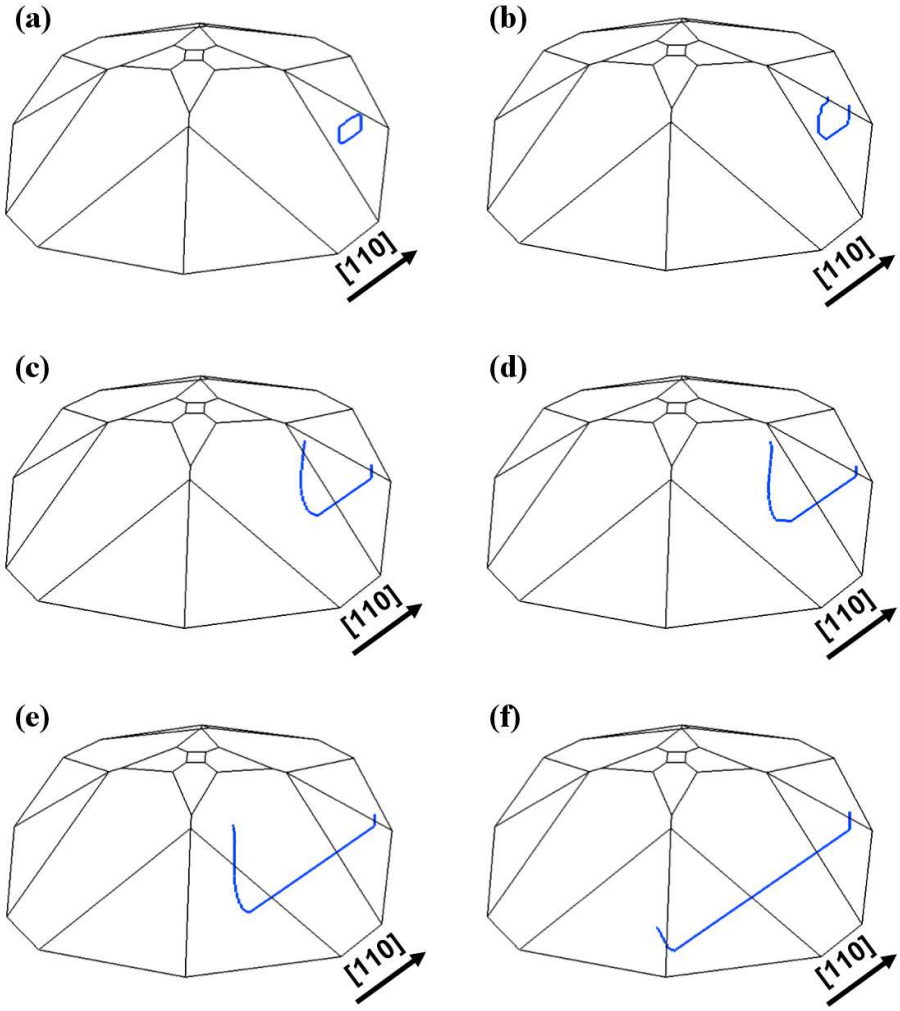

FIGURE 5.13: Evolution of a dislocation loop placed in the active corner of the island. the loop starts to expand (a), touching the free surfaces (b) threading arms are created and misfit segment initiate to be deposited. Threading arms evolution is driven by surface force and the direction of the segment in contact with the surface is modified changing facet orientation between panel (c) e (d). (f) final equilibrium position of dislocation, misfit is deposited and threading arms are pointing out from island free surfaces. No cross-slip events are detected: even if the left threading arm in panel (e) is oriented in the screw direction and the stress field in that region is favorable to observe cross slip, the lenght of the segment is to short to allow for changing glide plane.

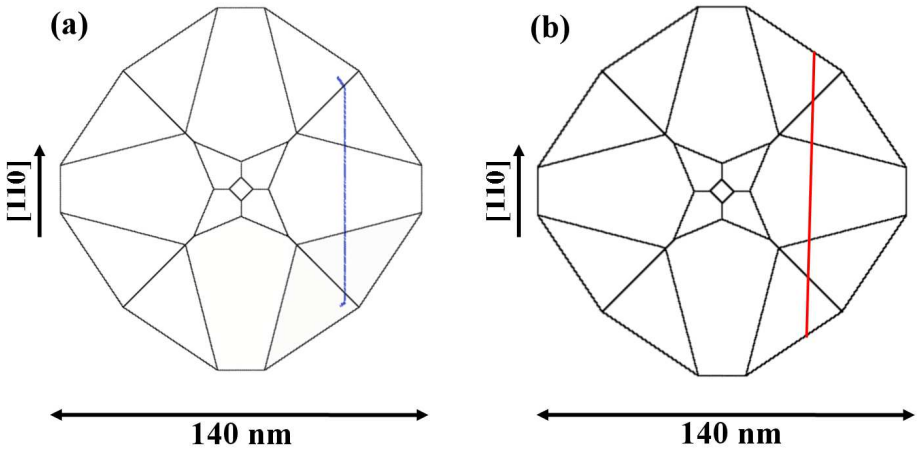

FIGURE 5.14: (a) Top view of the final shape and position of the first dislocation inside a superdome island as predicted by DD. (b) Thermodynamics equilibrium position of a 60^{circ} dislocation segment inside a superdome island, calculated as in Sec. 4.2. Both results show a long 60^{circ} straight segment deposited at the interface.

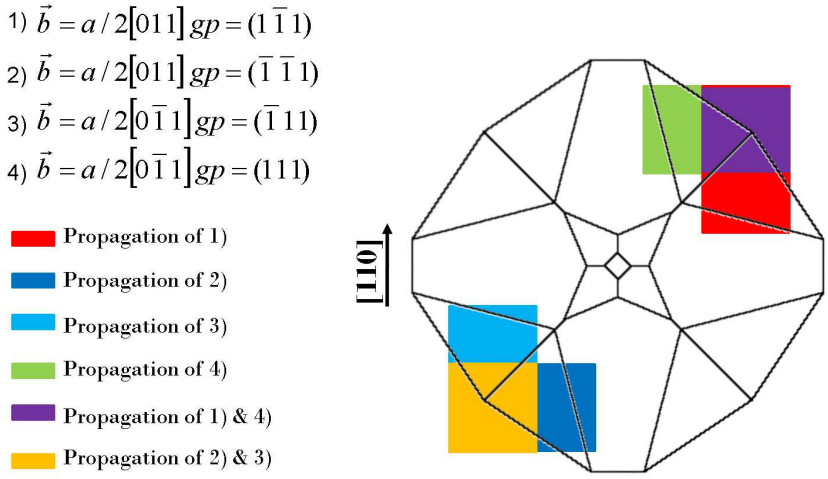

FIGURE 5.15: Map of propagation of a test loop (size 10 nm) in a superdome island with base equal to 140 nm an Ge content of 40 %. (a) slip system of the test loop. (b) behavior of the dislocation loop in the system when it is placed in different initial position of the island.

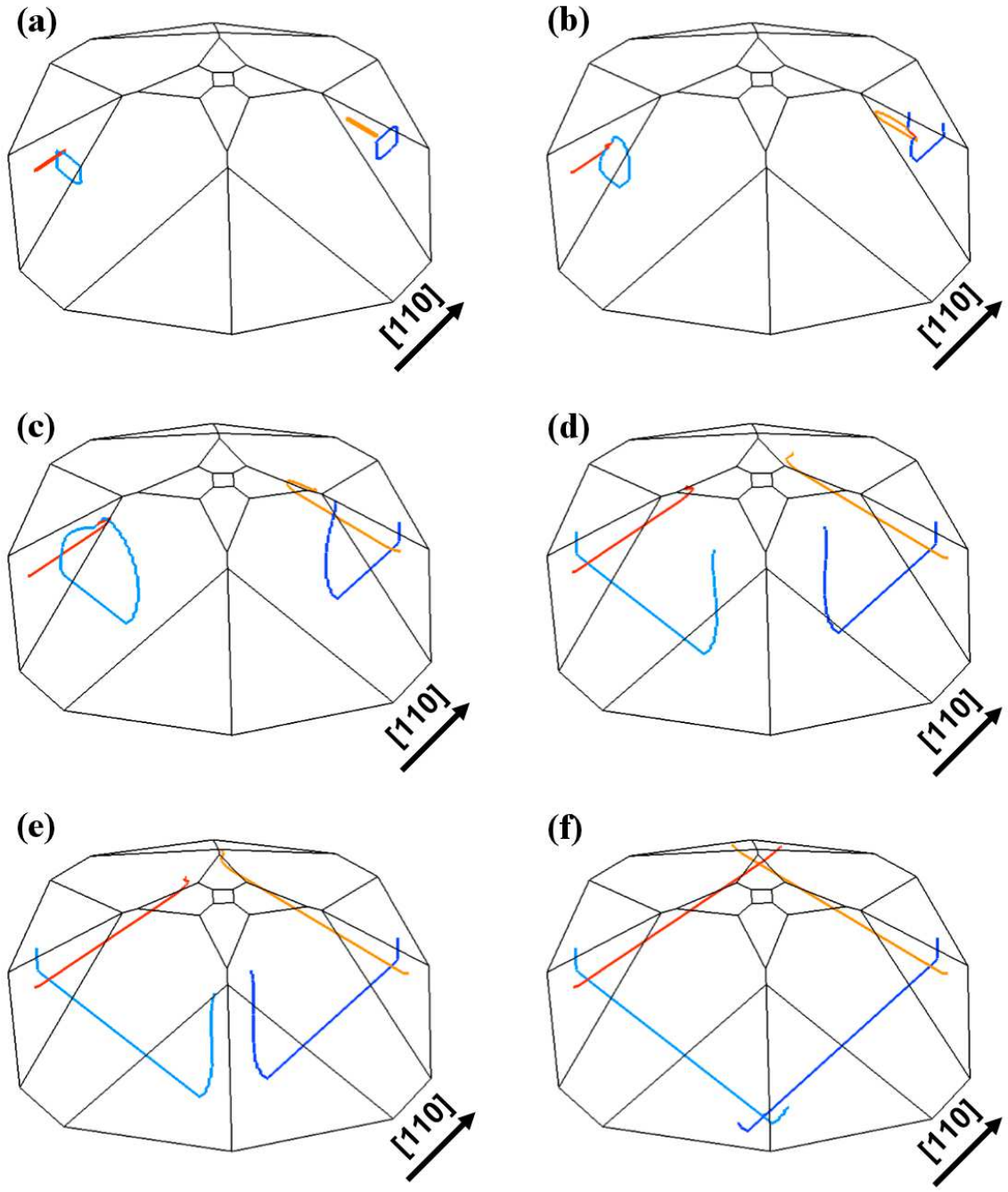

FIGURE 5.16: Evolution of four dislocation loops placed in the two active corners of the island, (see Fig. 5.15). The four loops starts to expand (a), touching the free surfaces and interacting each other (b)-(c). Misfit segment is deposited and the final microstructure is formed (d)-(f). Notice that no junctions formation is observed and even in this case, no cross-slip events are detected. Different color of dislocations means different slip system.

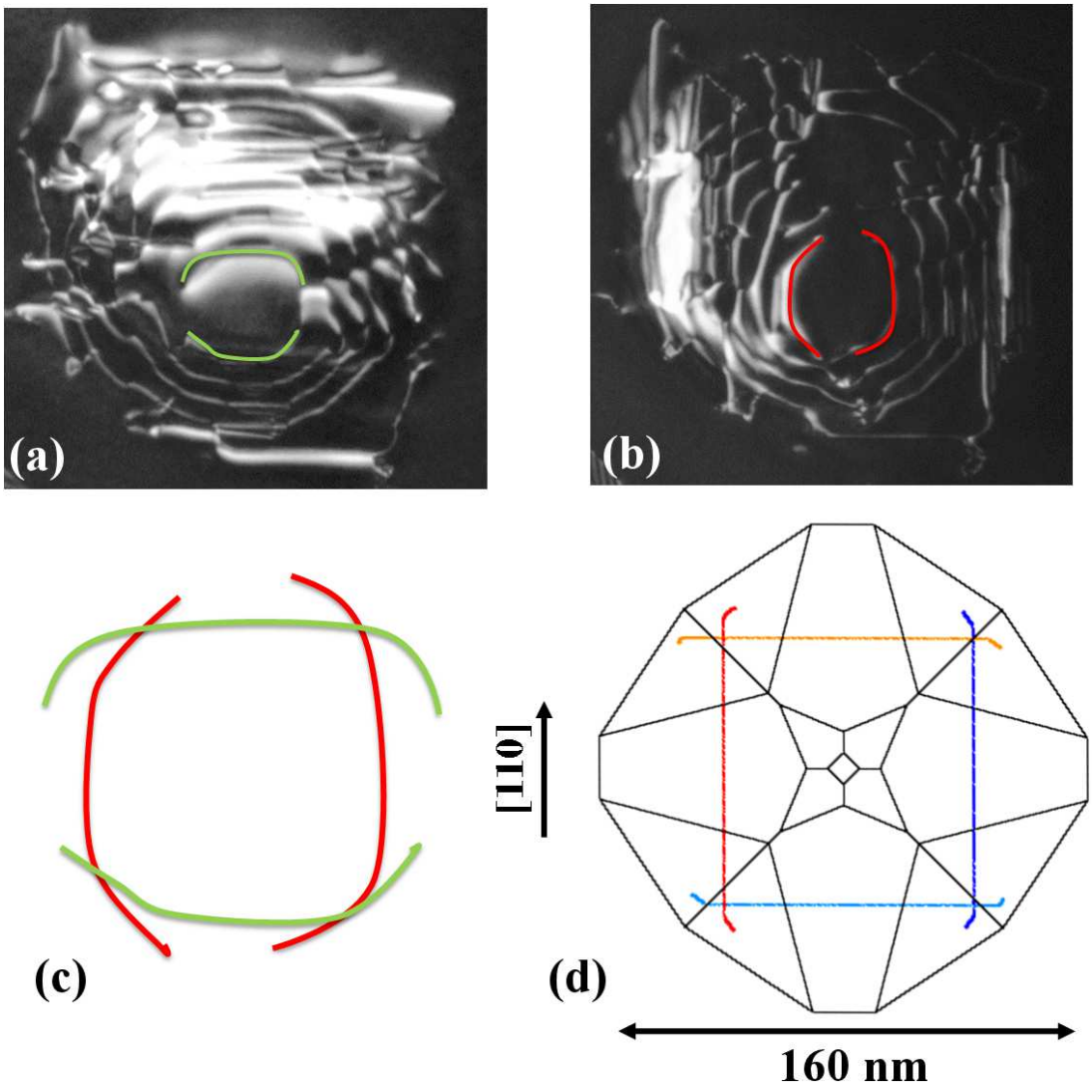

FIGURE 5.17: Comparison between TEM images and DD simulation results. (a) and (b) TEM images obtained with different reciprocal lattice vector $\vec{g}$. The TEM images reveals more details about the shape of dislocation with respect to their superposition shown in 1.11. The resulting dislocation pattern is shown in panel (c). Comparing panel (d) , where our predicted simulation pattern is reported (in top view with respect the island), and panel (c), it is clear that the simulation captures the main feature of the experimental data. We checked that the contrast in images (a) and (b) is compatible with slip system used in the simulations (d).

threading arms. Experimental TEM image [55] reported in Fig. 1.11 shows the dislocation pattern at the interface of an island of a multidislocated island and can be compared directly to our simulations. We can assign the inner round structure as the sign of the first stage of cyclic growth. The image is the superimposition of two different TEM images obtained with two different reciprocal lattice vector $\vec{g}$, and so some details are missed (see Fig. 5.17 panel (a) and (b)) because of different contrast. Analyzing separately the two images it appears the pattern showed in Fig. 5.17 (c). Comparing panel (d) , where our predicted simulation pattern is reported (in top view with respect the island), and panel (c), it is clear that the simulation captures the main feature of the experimental data. Misfit dislocations form a pattern similar to a square (more rounded in the experiment) in both cases, the arms appearing out of the square shape could be ascribed to threading arms. By the way the experimental pattern in panel (b) appears more bend. This morphology is due to the fact that in our simulation the interface between island and substrate is perfectly flat, while in the experiments it is curved, thus so the deposited segments do not appear as straight lines.

Mechanical cross slip in superdome islands

In all the simulation we discussed, no cross slip events were observed. We ascribed this behavior to the short lenght of threading segments in the screw direction due to small island size. What we expect is to observe cross slip events by increasing the volume of the island, to enhance the threading dislocation lenght and therefore the cross slip probability. We run simulations increasing island base size, studying the propagation of a single dislocation loop. We noticed cross slip event for superdomes with base equal to 200 nm, and in Fig. 5.18 the dynamics is reported. The dislocation has the same evolution as in panel (a)-(d) of Fig 5.13. When the dislocation reaches the area in which cross slip is favored, Fig 5.18 (a) the lenght of the screw segment is larger and in panel (b) the onset of cross slip is observed (light blue segment appears). Dislocation bows out in the cross slip direction, panel (c). Because the RSSgp and RSScs in this region are comparable (see Fig. 5.11 their difference is close to zero), during the cross slip event the local stress field is modified, and in panel (d) we observed dislocation double cross slip phenomenon [98]. At the interface small misfit segments are deposited for both slip systems (zig-zag shape, panel (e)). Finally, in panel (e) the dislocation reaches a region where RSScs is larger than RSSgp, and the misfit segment is deposited in the cross slip direction.

At this stage, we can notice that TEM observation made at late stages of cyclic growth are revealing the zig-zag features in the dislocation pattern (Fig. 5.19(a)), that compare very well with the results of simulations in Fig. 5.19 (b).

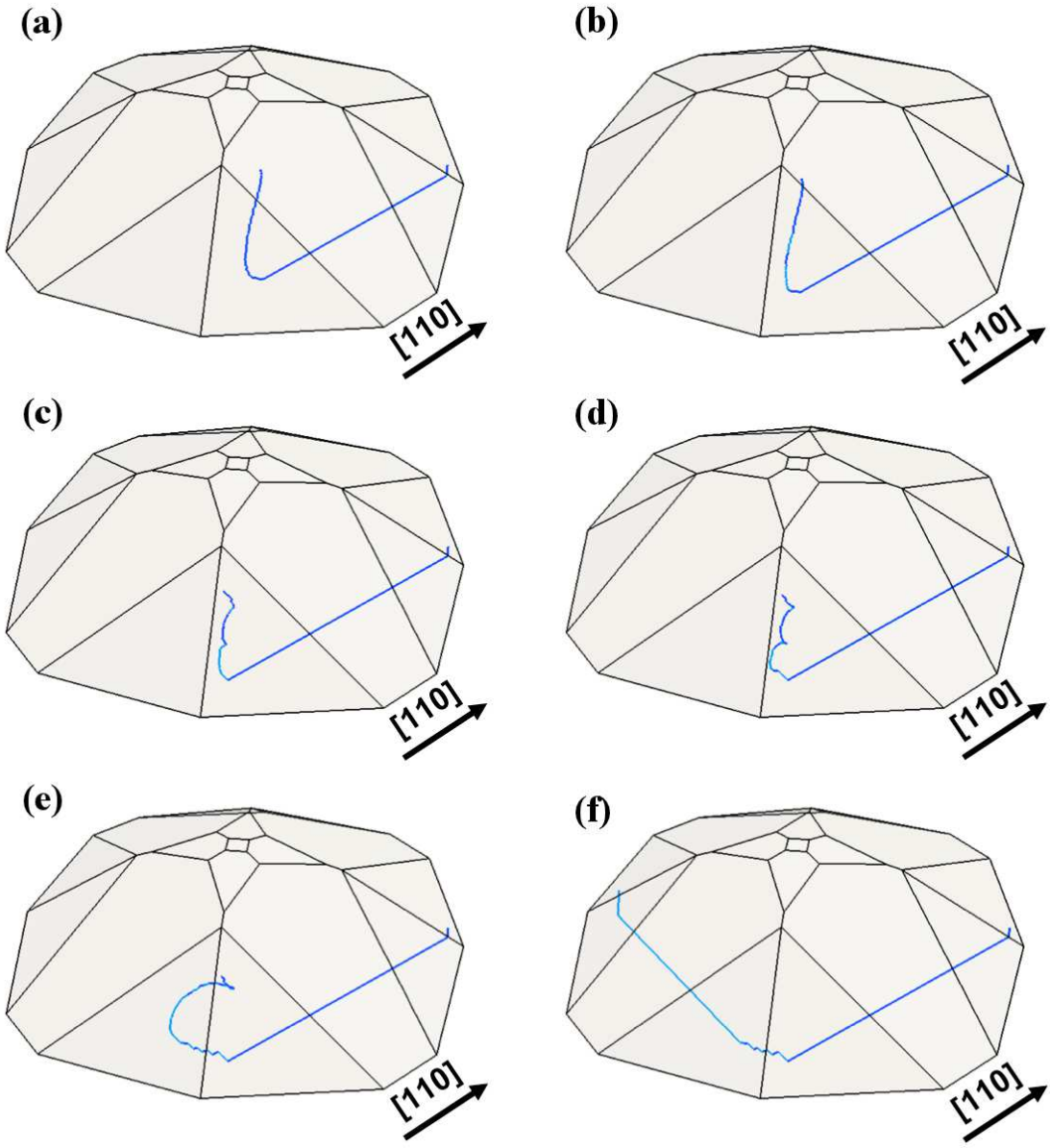

FIGURE 5.18: Cross slip events in $Si_{0.6}Ge_{0.4}$ island. The base of the island is 200 nm. Dislocation threading arm is aligned in the screw direction (a). In panel (b) is highlighted the onset of cross slip phenomenon and in panel (c) dislocation bows out in the cross slip direction. Because the RSSgp and RSScs in that region are comparable (see Fig. 5.11 their difference is close to zero), during the cross slip event the local stress field is modified, and in panel (d) we observed dislocation double cross slip phenomenon. At the interface small misfit segments are deposited for both slip systems (e). In panel (f) dislocation reaches a region where RSScs is larger than RSSgp, and the misfit segment is deposited in the cross slip direction.

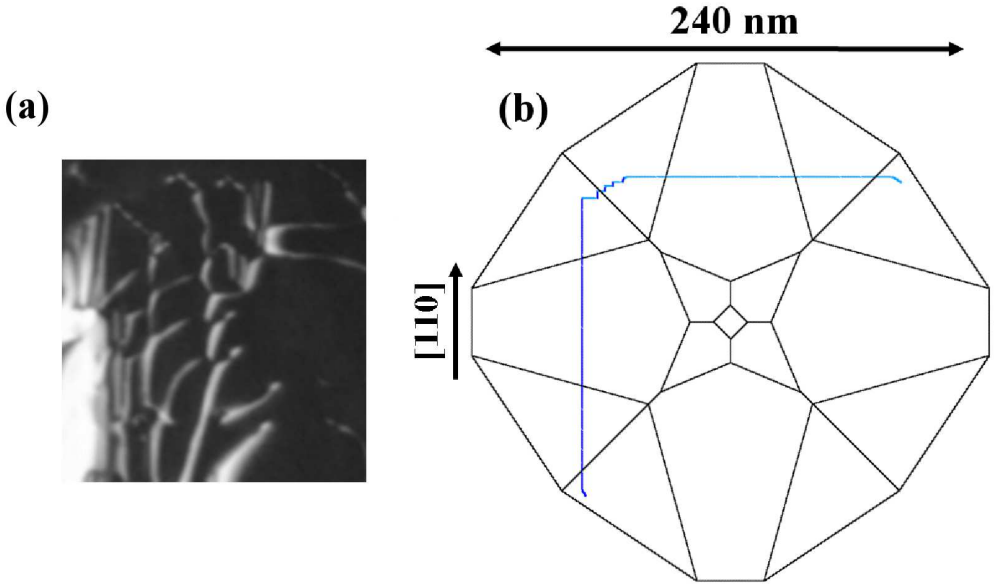

FIGURE 5.19: Comparison between experimental dislocation pattern and simulation results. The zig-zag features in panel (a) can be ascribed to a series of double cross slip events

Conclusions

My Ph. D. work led to the development of numerical methods devoted to the study of elastic and plastic relaxation in SiGe/Si (001) heteroepitaxial nanostructures. The methods were successfully applied to the study of self-assembled nanostructures arising from the heteroepitaxial growth of Ge (or SiGe alloys) on Si substrate (three dimensional islands and thin films). First of all, I studied the mechanisms allowing for elastic relaxation. Tuning the initial condition, it was possible to calculate with Finite Element Method the elastic field in SiGe islands. Then the variation of compositional profile, observed during the three dimensional growth, were determined by an ad hoc Monte Carlo algorithm coupled with FEM. My main contributions, however, were in the field of plastic relaxation and the study of dislocations in nanostructures. First I developed a novel approach to handle misfit dislocation in nanostructures in the FEM framework. The developed method allows for determining the elastic field of dislocations in small size object, where the extended defects deeply interact with free surfaces and interfaces. It was shown how my novel computational strategy can be applied to the study of the plastic relaxation onset (introduction of the first dislocations) in Ge/Si islands, finding an excellent agreement with experimental data. Furthermore we depicted how by proper patterning of the Si (001) substrate it is possible to predict dislocation confinement, as confirmed experimentally by AFM and TEM analysis, in prescribed areas of the heteroepitaxial system, opening a viable path for dislocation engineering. Then, I adapted the microMegas dislocation dynamics (DD) code to dislocation propagation in nanostructures. The DD code was originally designed to study the time evolution of extended defects in bulk system. I therefore introduced suitable modifications for treating free surfaces and for handling the propagation of threading arms (dislocation touching free surfaces) in the system. Simulations performed in overgrown islands, predict a dislocation pattern at the SiGe island extremely similar to the experimentally observed dislocation microstructure.

A

Elasticity theory equations used in this work

This brief appendix is intended to give some very basic concepts that were often recalled in this work.

A.1 Strain tensor

Under external applied forces, any elastic medium undergoes a deformation from its equilibrium (external force-free) configuration. By denoting with $\mathbf{r}$ the position of a given point inside the medium prior of the deformation, and with $\mathbf{r'}$ its position in the deformed medium, it is possible to define the displacement field $\mathbf{u} = \mathbf{r'} - \mathbf{r}$ at every point. Elastic deformation is completely known when $\mathbf{u}(\mathbf{r})$ is known for every $\mathbf{r}$. Given a small deformation $\delta\mathbf{r}$, it can be written

$$u_i(\mathbf{r} + \delta\mathbf{r}) = \mathbf{u_i}(\mathbf{r}) + \frac{\partial \mathbf{u_i}(\mathbf{r})}{\partial \mathbf{x_k}} \delta \mathbf{x_k}.$$

where the derivatives $\partial_k u_i$ defines the components of a rank 2 tensor γ_{ik}, which can be decomposed into a symmetric and an anti-symmetric part:

$$\varepsilon_{ik} = \frac{1}{2}\left(\frac{\partial u_i}{\partial x_k} + \frac{\partial u_k}{\partial x_i}\right) \qquad and \qquad \omega_{ik} = \frac{1}{2}\left(\frac{\partial u_i}{\partial x_k} - \frac{\partial u_k}{\partial x_i}\right).$$

In other words, any possible deformation of the elastic body is decomposed into one rotation, described by the tensor ω_{ik}, and one distortion, which is described by ε_{ik}. The tensor ε_{ik} is the strain tensor. As it is clear from its definition, ε is symmetric: $\varepsilon_{ik} = \varepsilon_{ki}$. Figure. A.1 is intended to show the physical meaning of each strain tensor component.

If $\mathrm{d}V$ the volume of a small portion of the solid before the deformation and $\mathrm{d}V'$ is the volume of the same portion after the deformation, those quantities are linked by the relation [57]

$$dV' = dV(1 + Tr(\varepsilon)).$$

This means that the trace of the strain tensor is the relative volume change with deformation $(dV' - dV)/dV$.

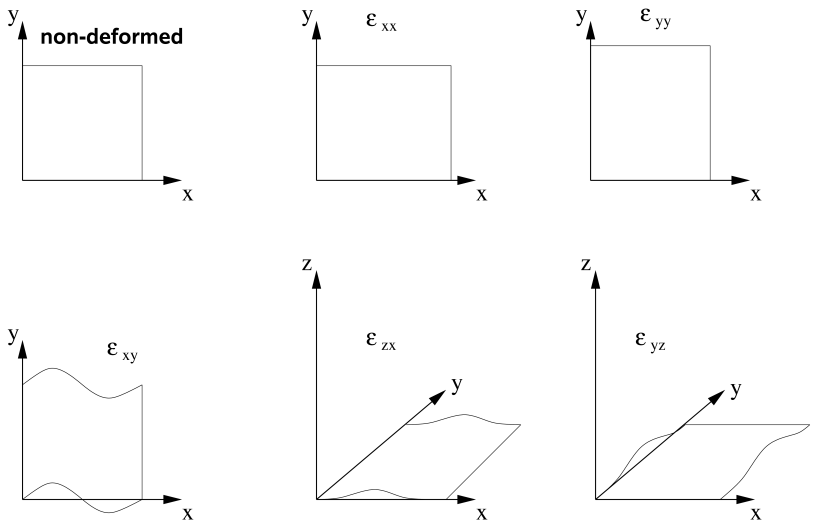

FIGURE A.1: Illustration of the physical meaning of each strain tensor component.

A.2 Equations of elasticity theory

The elastic response of a medium under applied external forces is completely described by the stiffness tensor c_{ijkl}. This tensor links stress to strain tensor, since it holds

$$\sigma_{ij} = c_{ijkl}\varepsilon_{kl}.$$

The tensor c_{ijkl} have several symmetries. The symmetry of the stress tensor implies that $c_{ijkl} = c_{jikl}$, while the symmetry of the strain tensor implies $c_{ijkl} = c_{ijlk}$. Finally, from thermodynamic arguments it is possible to demonstrate that $c_{ijkl} = c_{klij}$. Since both σ and ε are symmetric tensors, this means that each one has six independent coefficients. It is thus useful to use Voigt indexes, to simplify the notation. Making the following statements: $xx \to 1$, $yy \to 2$, $zz \to 3$, $xy \to 4$, $yz \to 5$, $xz \to 6$ it is possible to explicit c_{ijkl} with only two indexes; this way the stress-strain relaxation can be written as

$$\begin{aligned}
\sigma_{xx} &= c_{11}\varepsilon_{xx} + c_{12}\varepsilon_{yy} + c_{13}\varepsilon_{zz} + c_{14}\varepsilon_{yz} + c_{15}\varepsilon_{zx} + c_{16}\varepsilon_{xy} \\
\sigma_{yy} &= c_{21}\varepsilon_{xx} + c_{22}\varepsilon_{yy} + c_{23}\varepsilon_{zz} + c_{24}\varepsilon_{yz} + c_{25}\varepsilon_{zx} + c_{26}\varepsilon_{xy} \\
\sigma_{zz} &= c_{31}\varepsilon_{xx} + c_{32}\varepsilon_{yy} + c_{33}\varepsilon_{zz} + c_{34}\varepsilon_{yz} + c_{35}\varepsilon_{zx} + c_{36}\varepsilon_{xy} \\
\sigma_{yz} &= c_{41}\varepsilon_{xx} + c_{42}\varepsilon_{yy} + c_{43}\varepsilon_{zz} + c_{44}\varepsilon_{yz} + c_{45}\varepsilon_{zx} + c_{46}\varepsilon_{xy} \\
\sigma_{zx} &= c_{51}\varepsilon_{xx} + c_{52}\varepsilon_{yy} + c_{53}\varepsilon_{zz} + c_{54}\varepsilon_{yz} + c_{55}\varepsilon_{zx} + c_{56}\varepsilon_{xy} \\
\sigma_{xy} &= c_{61}\varepsilon_{xx} + c_{62}\varepsilon_{yy} + c_{63}\varepsilon_{zz} + c_{64}\varepsilon_{yz} + c_{65}\varepsilon_{zx} + c_{66}\varepsilon_{xy}
\end{aligned} \tag{A.1}$$

In addition to that, the symmetry of the crystal imposes further reduction to the independent coefficient in the stiffness tensor. Depending on the type of crystal, there are 21 independent components in the case of the triclinic crystal, 13 for the monoclinic, 9 for the orthorhombic and 3 for the cubic. The latter ones are usually mentioned as c_{11}, c_{12} and c_{44}.

One relevant case is the omogeneous and isotropic medium. Here, only two stiffness tensor components are independent, and are called Lamé constants λ and μ. The parameter λ is the shear modulus; it holds

$$\begin{aligned} \lambda &= c_{12} \\ \mu &= c_{44} = \frac{1}{2}\left(c_{11} - c_{12}\right) \end{aligned}$$

and the link with Young modulus Y and Poisson ratio ν is

$$\begin{aligned} \lambda &= \frac{\nu Y}{(1+\nu)(1-2\nu)} \\ \mu &= \frac{Y}{2(1+\nu)}. \end{aligned}$$

To deform the medium, external forces must do work, which must equal the elastic energy stored by the medium in consequence of the applied forces. The correspondent elastic energy density is

$$E = \frac{1}{2} c_{ijkl} \varepsilon_{ij} \varepsilon_{kl}.$$

B

Introduction to dislocations

This appendix is devoted to introduce the concept of dislocation, in particular focusing on dislocations appearing in Silicon-Germanium heteroepitaxy.

B.1 Burgers vector and dislocation line

Dislocations are line defects that introduce plastic deformation in a perfect crystal. So Their more appropriate description has to be referred to the atomic crystal structure [135].

In particular each dislocation is individuate both in type and position using two important vectors: the *Burgers vector* and the *dislocation line*.

A simple explanation can be provided using fig. B.1. In the middle a perfect undeformed crystal is represented (we choose a simple cubic crystal in order to make easy the description but all the definitions remain valid for a general crystal). Around the image of the perfect crystal the three different possible dislocation geometry are reported. One have to imagine to cut the structure along the planes shown in the three empty cubes. The atoms above and below the selected planes are moved as shown by the arrows by an half lattice parameter.

The new deformed lattices are shown in the external figures. They are perfect in all the structure but in the neighborhood of the AA lines. These lines are the *dislocation lines*. If the atoms around the cutting plane are displaced in the perpendicular directions to the line AA, the dislocation is called *edge*; if instead the same atoms are displaced in the parallel direction to the line AA a *screw dislocation is formed*; if finally they are displaced in a general direction with respect to the line AA the dislocation is called *mixed dislocation*. In particular in the last case the dislocation is characterized by the angle between the dislocation line and the direction of the deformation and it is named by this angle, for instance an important dislocation in the diamond structure is the 60° one. If a 60° dislocation is present in a crystal the defect is characterized by a dislocation line and direction of the deformation forming a 60° angle. A simple description of the edge dislocation is the following: if in a crystal an edge dislocation is present, in the deformed region an extra half lattice plane is inserted (see fig. B.2). In this case the dislocation line is simply the edge of the extra plane.

Instead, if in a crystal a screw dislocation is present, the lattice plane perpendicular to the dislocation line are rotated along the dislocation line as shown in fig. B.1 along the

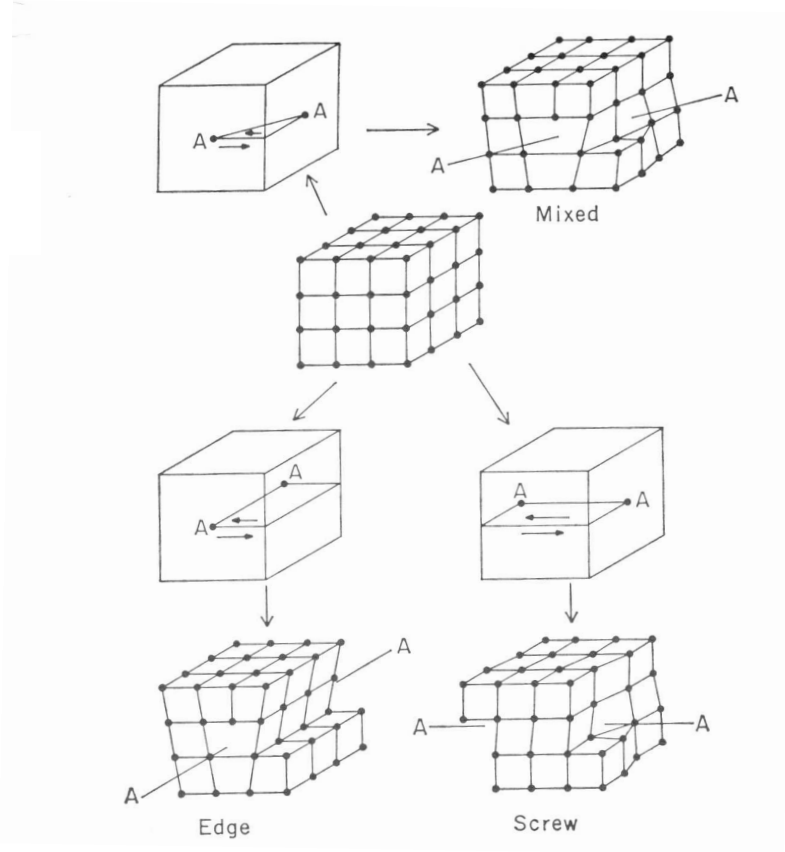

FIGURE B.1: The introduction of edge, screw and mixed dislocations in a perfect crystal [135].

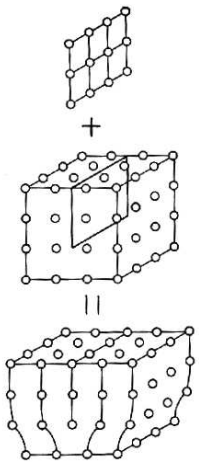

FIGURE B.2: Edge dislocation:an half extra plane in a crystal.

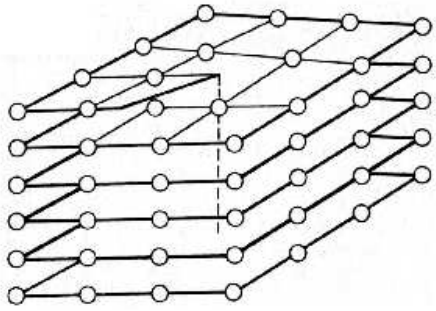

FIGURE B.3: Screw dislocation: planes screw around the dislocation line (dashed in the figure) [135]

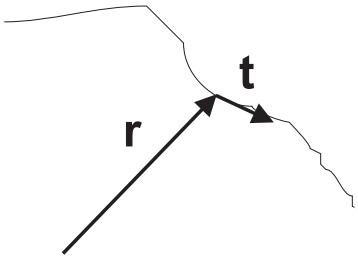

FIGURE B.4: The tangent vector $\vec{t}$ of a dislocation line in a point individuated by $\vec{r}$

AA line. In particular they screw along that line as clearly shown in fig. B.3 where the dislocation line is the dashed one.

The atoms around the dislocation line are called *core atoms*, and in general the ensemble of that atom are called *core*.

In order to give a precise description of dislocations in a crystal, their position and the consequent displacement have to be indicated.

The dislocation position is simply identified by the dislocation line position in each point. So we have to introduce a vectorial field $\vec{r}$ that individuates the position of an infinitesimal dislocation line segment in the crystal. In fig. B.4 an example is reported, $\vec{t}$ is the infinitesimal dislocation line segment (tangent to the line by definition) ,$\vec{t} = \frac{d\vec{r}}{dr}$).

In order to define the actual atoms displacement due to the dislocation, as already mentioned, another very important vector is introduced: the *Burgers vector*.

In fig. B.5 two different loops in a crystal are drawn: on the left it is around a dislocation line, on the right it is in a perfect crystal. Both begin in the site label M and finish in the site Q. Each loops segments (vertical and horizontal ones) are composed by the same number of lattice parameters. However, in the loop on the left the point labeled Q and the point labeled M are the same lattice site, instead in the dislocated crystal Q and M correspond to different lattice site. The vector $Q\vec{M}$ in the loop on the right is the Burgers vector of the dislocation involved. This definition is valid for each dislocation type (the simple one used in fig. B.5 is an edge dislocation).

In fig. B.6 the same definition is used in the case of a screw dislocation.

It should be now clear that Burgers vector and dislocation line of an edge dislocation are perpendicular by definition, instead for a screw dislocation they are always parallel. In the case of a mixed dislocation Burgers vector and dislocation line form an arbitrary angle. So it is possible to divide the Burgers vector in its edge component (the component perpendicular to the dislocation line) and its screw component (the parallel one). The

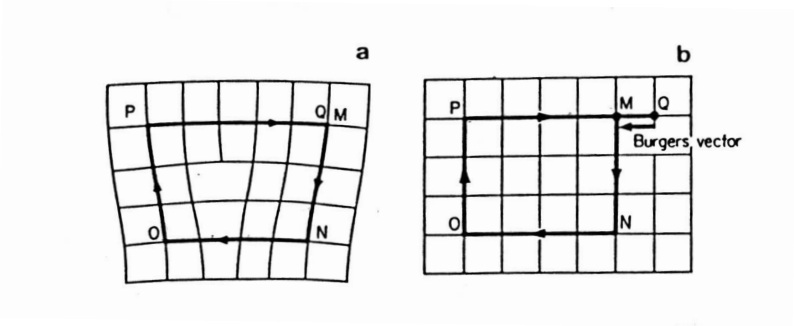

FIGURE B.5: Burgers vector definition: the difference vector between the two loops in the figure ($Q\vec{M}$), the left loop encircles the dislocation, the right one is in a perfect crystal[136]

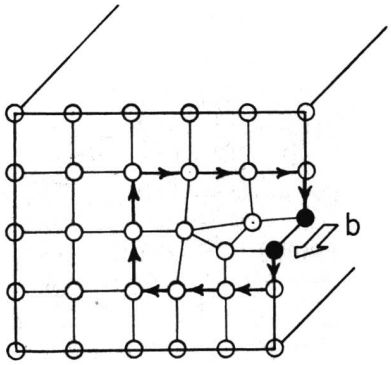

FIGURE B.6: Burgers vector for a screw dislocation [135]

actual atoms displacement, in this case, is obtained equally moving the atoms directly as imposed by the total Burgers vector or first by one component and then by another.

It is important to notice that the Burgers vector definition has some arbitrary aspects. In particular changing the direction going through in the dislocation loop, the Burgers vector changes its direction. It is a convention to chose first the direction of the dislocation line and then to individuate the Burgers vector going around the loop in clock wise observing it along the positive direction of the dislocation line.

Up to now, we have always taken under consideration dislocation characterized by a Burgers vector of the same length of a lattice parameter, such dislocations are called *perfect dislocation*. It is otherwise possible that a dislocation presents a Burgers vector less then a lattice parameter long. In this case the dislocation is called *partial dislocation*.

B.2 The dislocation motion

As we said the studies about dislocations gave rise from studies about materials plasticity. When a solid is subjected to an external force the dislocations already present as a defect in the crystal or nucleated subsequently that force, move until they reach the free surface where they cause the macroscopic deformation.

The dislocation motion can be classified in two different types: *glide motion* e *climb motion*.

The dislocation can move into the plane containing both the dislocation line and the Burgers vector, in this case the motion is called glide motion, or changing the dislocation plane, the climb motion.

The glide motion is more energetically favored, it is the first activated and the more observed. Therefore the plane containing the dislocation line and the Burgers vector is called *glide plane*.

The climb motion can be activated only at sufficiently high temperature: a dislocation can change plane only if atoms can be removed.

It is assumed that dislocation glide involves the thermal creation and migration of *kinks*. Let us consider a dislocations where segments have been displaced within the glide plane, keeping the same dislocation line direction. The connection between the segments are called dislocations kinks (see fig. B.7). So the glide motion can be pictured as the formation of two symmetric kinks (a right step and a left one along the dislocation line) and their migration in two opposite directions, resulting in the progressive glide of the dislocation line into the glide plane.

During the motion dislocations can approach each other, they can interact. The interaction between dislocations is a very complex item. Many different action can be subsequent to dislocation interaction, the simpler examples are their repulsion and attraction. The whole interaction mechanisms is already unclear, they depends from the particular geometries of the dislocations, their elastic fields and their glide planes. Other known phenomenon linked to dislocations interaction are the formation of new dislocations in the crossing points (*pinning*) or the deviation of dislocation to another equivalent glide plane (*Jog*) as shown in fig. B.7, this is the case of a developed climb motion of dislocations, jogs for the climb motion are the analogous of kinks for the glide one.

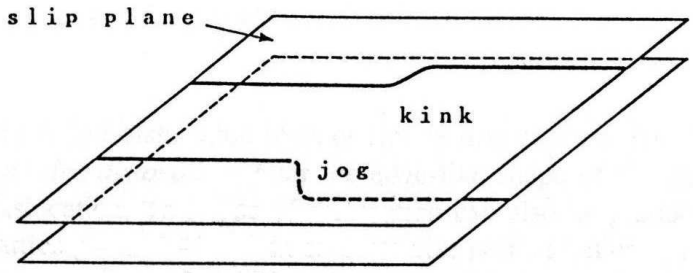

FIGURE B.7: Examples of jogs and kinks

B.3 Dislocations in linear elasticity theory

Linear elasticity theory, as already explained, turns to be a very useful tool to describe the elastic field (in particular the long range) due to dislocations.

Here we want report the results concerning an isolated straight dislocation, that is the subject of this thesis.

Two items are mainly important: the elastic energy and the interaction forces between two straight dislocations.

It is also important to notice that from the equilibrium equations A considering static conditions, the exact expressions of the displacements around a dislocation can be obtained, imposing that, considering a close loop around the dislocation, the displacement of the final point with respect to the initial one has to be equal to the Burgers vector length. From the displacement expressions it is easy to obtain stress and strain terms.

If the dislocation line is parallel to the z axis, in the case of a screw dislocation the Burgers vector will be in the same direction ($\vec{b} = b\vec{k}$) while for an edge dislocation it will be in one of the perpendicular directions, let us consider it in the x direction ($\vec{b} = b\vec{i}$). In the first case strain and stress have the following expressions:

$$\begin{aligned} \epsilon_{xz} &= \frac{\partial u}{\partial z} + \frac{\partial w}{\partial x} = \frac{b}{2\pi}\frac{y}{x^2+y^2} \\ \epsilon_{yz} &= \frac{\partial v}{\partial z} + \frac{\partial w}{\partial y} = -\frac{b}{2\pi}\frac{x}{x^2+y^2} \\ \epsilon_{xx} &= \epsilon_{yy} = \epsilon_{zz} = \epsilon_{xy} = 0 \end{aligned} \tag{B.1}$$

$$\begin{aligned} \sigma_{xz} &= \frac{\mu b}{2\pi}\frac{y}{x^2+y^2} \\ \sigma_{yz} &= -\frac{\mu b}{2\pi}\frac{x}{x^2+y^2} \\ \sigma_{xx} &= \sigma_{yy} = \sigma_{zz} = \sigma_{xy} = 0 \end{aligned} \tag{B.2}$$

Instead for the edge dislocation the results are:

$$\begin{aligned}
\epsilon_{xx} &= \frac{by}{2\pi}\frac{\mu y^2 + (2\lambda+3\mu)x^2}{(\lambda+2\mu)(x^2+y^2)^2} \\
\epsilon_{yy} &= \frac{by}{2\pi}\frac{(2\lambda+\mu)x^2 - \mu y^2}{(\lambda+2\mu)(x^2+y^2)^2} \\
\epsilon_{xy} &= \frac{b}{2\pi(1-\nu)}\frac{x(x^2-y^2)}{(x^2+y^2)^2} \\
\epsilon_{zz} &= \epsilon_{xz} = \epsilon_{yz} = 0
\end{aligned} \tag{B.3}$$

e

$$\begin{aligned}
\sigma_{xx} &= \frac{\mu b}{2\pi(1-\nu)}\frac{y(3x^2+y^2)}{(x^2+y^2)^2} \\
\sigma_{yy} &= -\frac{\mu b}{2\pi(1-\nu)}\frac{y(x^2-y^2)}{(x^2+y^2)^2} \\
\sigma_{zz} &= \nu(\sigma_{xx}+\sigma_{yy}) = \frac{\mu\nu by}{\pi(1-\nu)(x^2+y^2)}
\end{aligned} \tag{B.4}$$

It is interesting to notice that directly from the mathematical form of strain and stresses we can derive the dislocation theory limit: they have an unresolved value in the origin in correspondence to the core of the dislocation. In fact in this area the stresses are too large in order to be predicted by the linear elasticity equations. In that region the atomistic nature of solids can not be neglected, it is needed to consider the actual atoms positions, an atomistic treatment is needed.

For mixed dislocations the previous solutions remain valid for the edge and screw components separately (i.e. using as Burgers vectors the edge and screw components respectively) and the expressions of stresses and strain of the mixed dislocation will be the sum of the component's solution.

B.3.1 Elastic energy

When a solid is subject to a deformation, it accumulates energy used afterwards to return at the equilibrium status (shape and volume). This potential energy is called *elastic energy*. As in a general definition energy is the integration of the product force times displacements, the elastic energy is the integration of the product stress times strain. Obviously this integration is not always simple, it depends on the tensor's form of strain and stress. The energy accumulated in a solid due to a dislocation deformation field is called *self energy*.

We have already described the stress and strain forms for different dislocation. Their integration in order to find the elastic energy is not simple but it can be actually done analytically (see for instance [98]).

It is found that the energy per unit length contained in a cylinder of radius r and length L of an infinite straight dislocation, in an otherwise perfect crystal can be written:

$$\frac{E_{self}}{L} = \frac{K(\beta)}{4\pi}b^2 \ln\frac{r}{r_c} + \frac{E_c}{L}\,, \tag{B.5}$$

where $K(\beta)$ is called energy coefficient and depends on the angle β between the dislocation line and the Burgers vector and on the crystal properties, b is the Burgers vector length, r_c is a parameter called core radius and E_c is the core energy. The meaning of these two last quantities will be more clear in the following.

The logarithmic term in eq. B.5 diverges for both the limits $R \to 0$ and $R \to \infty$. The first divergence show another time the linear elasticity theory limit and the one of a continuum description. In the core region, characterized by breaking and stretched bonds, stresses are high and a discrete model is needed being at distance similar to the bonds length.

As a result it exist a critical value of r, called core radius (r_c), below it eq. B.5 does not give a good description of the elastic energy. In other words the region below r_c is the minimum region which cannot be described by elasticity theory. The elastic energy inside this region is called core energy (E_c).

Eq. B.5 also diverges for $R \to \infty$. In consequence, in an infinite crystal we cannot evaluate a finite total elastic energy of a dislocation (real crystal have a finite extension), however the important physical quantities are the energy coefficient $K(\beta)$, the core radius r_c and the core energy E_c.

B.3.2 Resolved shear stress

In this paragraph we want to describe shortly the last aspects for our interests, the interaction force between an external field and a dislocation. When an elastic field σ is acting on a dislocation with Burgers vector $\vec{b}$, it develops a force given (per unit length of the dislocation line) by:

$$F_{res} = \tau_{res} b = |\mathbf{S} : \sigma|\, b \,, \tag{B.6}$$

where $\mathbf{S}$ is called *Schmidt tensor* and $|\mathbf{S} : \sigma|$ is called the *resolved shear stress* (τ_{res}).

If $\vec{n}$ is the vector normal to the glide plane, then $\mathbf{S}$ is defined by:

$$\mathbf{S} = \frac{\vec{b}}{b} \otimes \vec{n} \,. \tag{B.7}$$

In the Schmidt tensor expression are summarized all the main characteristics of the dislocation taken under consideration: $\vec{b}$, the Burgers vector, is composed with $\vec{n}$, the geometric label for the glide plane. The resolved shear stress, then, composes these dislocation geometries with the external field. The resolve shear stress, together with the temperature, determines the dislocation motion. Large resolve shear stress means high probability of dislocation nucleation [98].

B.4 Dislocations in the diamond structure

Following the equation B.5 we learn that low energy dislocations are those with a minimum Burgers vector and we know, by the definition, that Burgers vectors are always a linear combination of lattice vectors. Thus, if the lattice vector is known, one can already specify possible low energy types of dislocations and also their glide plane, it will be the plane containing the minimum lattice translation vectors. In the diamond structure the planes with the highest lattice site density are the $\{111\}$ ones so they are preferred glide planes. In these planes the minimum lattice vectors are in the $\langle 110 \rangle$ directions. Since the dislocation line, at least locally, is also given by lattice translations, three possible dislocation types are favored in the diamond structure depending on the combination of dislocation line and Burgers vector. Fig. B.8 shows the case for [110] and $[1\bar{1}0]$ dislocations line ($\vec{j}$). For each

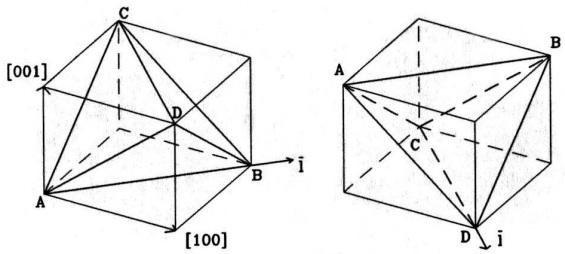

FIGURE B.8: Dislocation line in the directions [110] (left) and $[1\bar{1}0]$ (right). The other diagonal lines represented in the figure are the possible Burgers vector direction [137].

line six possible Burgers vectors (shown in the figure) exist [137].

Let us consider the left cube in fig. B.8 in which a [110] line dislocation is presented. As said three dislocation can be introduced:

- **screw dislocation**. If also the Burgers vector is in the [110] direction (segment AB in the figure), Burgers vector and dislocation line are parallel giving rise to a screw dislocation in the crystal.
- **edge dislocation**. If the Burgers vector is in the $[1\bar{1}0]$ direction (segment CD in the figure), Burgers vector and dislocation line are perpendicular developing an edge dislocation in the crystal.
- **60° dislocation**. If the Burgers vector is in one of the other four $\langle 110 \rangle$ directions (segments AC, AD, BC or BD), Burgers vector and dislocation line form a 60° angle, the dislocation is therefore a mixed dislocation with both screw and edge component.

Obviously the same observations hold for all the other dislocation line directions (e.g. for the right cube).

We will see in the next section that the most important dislocations in the heteroepitaxial Si-Ge structure are the 60° ones.

B.5 Introduction to the strain relaxation in the epitaxial structure

B.5.1 The 60° dislocation

While in general, for example in bulk metallic materials, dislocations are extended defects that degrade the quality of the solid, in epitaxy, as already explained in the first section, dislocations have a key role in the strain relaxation being therefore necessary if a relaxed layer has to be obtained. This simple consideration gives also another indication about the dislocation type population in epitaxial film. In the previous section we individuated three different dislocation type (screw, edge and 60°) energetically favored in diamond structures, here we will see their efficiency in strain relaxation.

Let see the figure B.9. There an heteroepitaxial structure with an edge or a screw dislocation at the interface is pictured. The epilayer has a bigger lattice parameter with

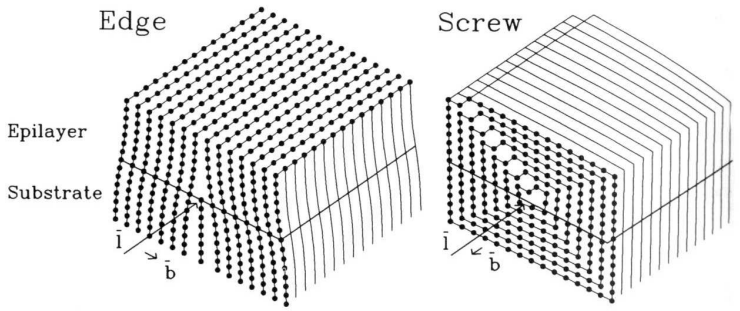

FIGURE B.9: Edge and screw dislocations at the interface of an heteroepitaxial structure [137].

respect to the substrate. We know that, in this case, during the growth an elastic field in the epitaxial layer is developed, in particular it is characterized by a compression in the growth plane and an expansion in the perpendicular direction (the pseudomorphic structure).

An important difference in the strain relaxation efficiency between the two dislocations in the figure is evident: the edge dislocation allows the epitaxial layer to release the compression, restoring its own lattice parameter (the edge dislocation is characterized by an half missing plane in the epitaxial layer), the screw dislocation instead doesn't change the in-plane lattice parameter of the epitaxial layer, it doesn't release the in-plane compression. An important observation is needed. The efficiency of the edge dislocation in the figure is closely linked to the Burgers vector direction: it is in the growth plane, if the Burgers vector would be perpendicular to the dislocation line but out the plane of the growth it doesn't relieve any strain (the half missing plane would be parallel to the growth plane). Therefore also in the case of a 60° dislocation only the edge component and, in particular, the component of it lying in the growth plane releases the compression. [137].

The heteroepitaxial Si-Ge structures for technological applications are mainly (001) oriented, i.e. the free surface is a (001) surface so also the interface is (001) oriented. Therefore the glide plane, being a {111} plane, is inclinated with respect to the interface. Burgers vector and dislocation line lie on the glide plane, in particular dislocations that can release more strain have dislocation line in the intersection between the glide plane and a plane parallel to the interface (the so called *misfit dislocations*). In this geometry an edge dislocation does not have Burgers vector in the ⟨110⟩ favored direction. Now it is clear that the most diffuse dislocation in heteroepitaxial Si-Ge films is the 60° dislocation characterized by $\vec{b} = \frac{a}{2}\langle 110\rangle$, dislocation line ⟨110⟩ and glide plane {111} [137].

B.5.2 Misfit dislocations and threading arms

In the previous section we learn that the 60° dislocation is the real subject of the strain relaxation in Si-Ge (001) heteroepitaxial structures. In order to play this role each 60° dislocation have to introduce a *missed* half-plane in the compressed epitaxial layer (an extra half-plane in the substrate). This means that for each 60° dislocation line only two of the four possible Burgers vectors can be present, the ones pointing towards the free surface. Hence in the films the deformation will appear at the surface. The deformation induced by the components of these Burgers vectors in the (001) direction causes a step at the surface. Typically an array of steps along [110] directions can be observed at the surface of Si-Ge epitaxial layers in correspondence to the 60° dislocations inside the layers.

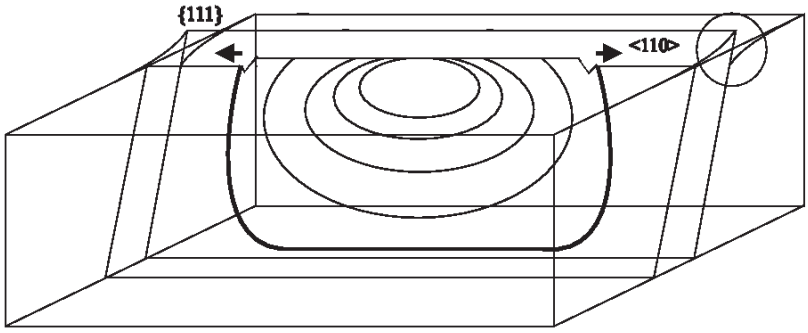

FIGURE B.10: Evolution of loop dislocations in epitaxial films

The ending points of these steps are called *pits*. They corresponds to the ending points of the 60° straight dislocation in the inner part of the crystal. An example is shown in figure B.10.

Dislocations in heteroepitaxial films nucleate mainly as loop dislocations as shown in the figure. After the nucleation the epitaxial elastic field acts on each part of the dislocations, consequently they increase their radius until they reach the interface, then they become a semiloop composed by a straight segment parallel to the interface (called *misfit segment*) and two *threading arms* reaching the surface. While when the dislocation line is a curve it is too difficult to describe in the microscopic geometry, in the second phase it can be easily described dividing the dislocation in three segments: the misfit segment and the two threading arms. The misfit segment will be (because energetically favored) a 60° straight dislocation relieving strain at the interface. The two threading arms turn to be mainly screw dislocations. The pits hence are the intersection between the threading arms and the free surface.

Pits and steps obviously degrade the morphological quality of the surface and, in consequence, degrade the performances of the devices eventually grown at the top of the structure. In fact this epitaxial layer are mainly used as buffer layers (bases of the microelectronic devices). The misfit segment, on the other hand, is absolutely necessary for the strain relaxation (the epitaxial layers has to be on their own lattice parameter for the technological application). Instead the threading arms, being screw dislocations, do not release strain and their presence causes only the structure degradation. So a very important goal is to individuate the growth conditions that minimized the threading arms density, increasing the misfit segment length (e.g. in fig. B.11 the condition of the misfit line A is favored with respect to misfit line B) [138]. An important part of my work has this target.

In the next we will briefly enumerate the main nucleation mechanisms in the epitaxial structures.

The elasticity theory, as mentioned, predicts the critical thickness necessary for the nucleation of the first dislocation, however the experimental values are much more high than the predicted ones. The reason is that the calculated value are the results of a thermodynamic calculation that does not take into consideration the kinetic activation barrier [101]. Until the layer reaches the critical experimental thickness, but reached the theoretical one the system is in the so called *metastable regime*. The extension in thickness of this regime depends on the growth conditions [101]. The kinetic processes characteristic of the barriers are, for example [101]:

1. **Homogeneous nucleation**. If the strain in the layer becomes sufficiently high (misfit

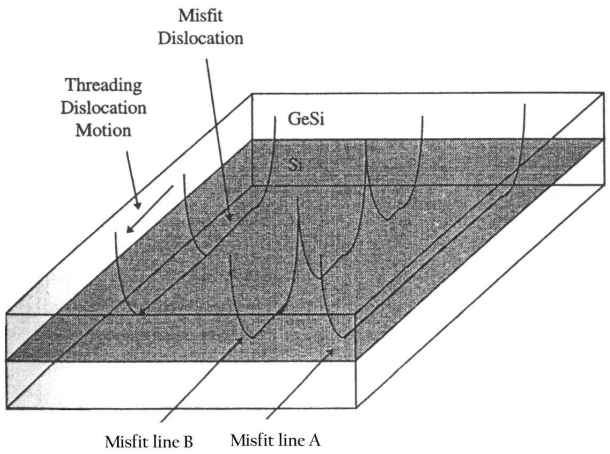

FIGURE B.11: Two different possible configurations of dislocation loops in epitaxial structure. The case denoted with line A is the ideal one being characterized by a long misfit segment and only two threading arms [138]

.

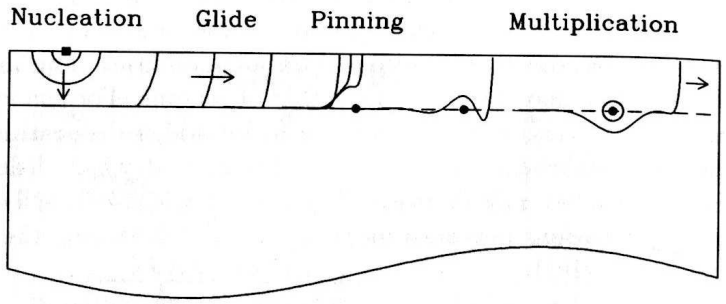

FIGURE B.12: Possible dislocations nucleation processes in epitaxial layer [137].

of about 6-8%) the nucleation can also spontaneously happen. It is a very rare case.

2. **Heterogeneous nucleation**. The nucleation mainly happens in a high-strain localized zone. It means where in the sample a superimposed strain field is already present. Typically where some point defects are present as vacancies or interstitials but also at surfaces and interfaces and points where dislocations arrive from the substrate at the interface. In this case we assist at the *pinning* mechanism: a dislocation of the substrate nucleate many dislocations in the epitaxial layer. The heterogeneous nucleation is the most diffuse nucleation process.

3. **Multiplication**. The intersection between dislocations can be a nucleation site for other dislocations. This happens mainly in low strained layer (e.g. $\epsilon = 0.005$). This mechanism is very complex, the nucleation sites are called *Frank-Read* sources [139].

4. **Islands**. Around the islands a strain accumulation occurs and dislocation can there nucleate.

Figure B.12 summerizes some of the possible nucleation processes [137].

Bibliography

[1] G. B. Stringfellow. *Rep. Prog. Phys.*, 45:469, 1982.

[2] V. A. Shchukin and D. Bimberg. *Rev. Mod. Phys.*, 71:1125, 1999.

[3] N. W. Ashcroft and N.D. Mermin. *Solid State Physics*. Saunders College Publishing, Forth Worth, 1976.

[4] P. Yu and M. Cardona. *Fundamentals of semiconductor*. Springler-Verlag, Berlin, 2004.

[5] In D. R. Lide, editor, *Handbook of chemistry and physics*. CRC PRESS, U.S.A, 1998.

[6] V. T. Bubelik, S. S. Gorelik, A. A. Zaitsev, and Polyakov A Y. *Phys. Status Solidi b*, 66:427, 1974.

[7] E. A. Steinman, V. I. Vdovin, T. G. Yugova, V. S. Avrutink, and N. F. Izyumskayak. *Semicond. Sci. Technol.*, 14:582, 1999.

[8] J. H. Van der Merwe. *J. Appl. Phys.*, 34:123, 1963.

[9] J. W. Matthews and A. E. Blakeslee. Defects in epitaxial multilayers: I. misfit dislocations. *Journal of Crystal growth*, 27:118–125, 1974.

[10] R. People and J. C. Bean. *Appl. Phys. Lett.*, 47:322, 1985.

[11] R. People and J. C. Bean. *Appl. Phys. Lett.*, 49:229, 1986.

[12] B. W. Dodson and J. Y. Tsao. *Appl. Phys. Lett.*, 51:1325, 1987.

[13] J. Y. Tsao, B. W. Dodson, S. T. Picraux, and D. M. Cornelison. *Phys. Rev. Lett.*, 59:2455, 1987.

[14] D. C. Houghton, D. D. Perovic, J-M. Baribeau, B. W. Dodson, and G. C. Weatherly. *J. Appl. Phys.*, 67:1850, 1990.

[15] D. J. Eaglesham and M. Cerullo. *Phys. Rev. Lett.*, 64:1943, 1990.

[16] M. Brehm, M. Grydlik, H. Lichtenberger, T. Fromherz, N. Hrauda, W. Jantsch, F. Schaffler, and G. Bauer. *Appl. Phys. Lett.*, 93:121901, 2008.

[17] R.J. Wagner and E. Gulari. *Phys. Rev. B*, 69:195312, 2004.

[18] L. Nurminen, F. Tavazza, D.P. Landau, A. Kuronen, and K. Kaski. *Phys. Rev. B*, 68:085326, 2003.

[19] J. Tersoff, B.J. Spencer, A. Rastelli, and H. von Kanel. *Phys. Rev. Lett.*, 89:196104, 2002.

[20] A. Rastelli, H. von Kanel, B.J. Spencer, and J. Tersoff. *Phys. Rev. B*, 68:115301, 2003.

[21] Z. Gai, W.S. Yang, R.G. Zhao, and T. Sakurai. *Phys. Rev. B*, 59:15230, 1999.

[22] J. Tersoff and R. M. Tromp. *Phys. Rev. Lett.*, 70:2782, 1993.

[23] G. Capellini, M. De Seta, and F. Evangelisti. *J. Appl. Phys.*, 93:291, 2003.

[24] D.B. Migas, S. Cereda, F. Montalenti, and L. Miglio. *Surf. Sci.*, 556:121, 2004.

[25] A.A. Stekolnikov, J. Furthmuller, and F. Bechstedt. *Phys. Rev. B*, 65:115318, 2002.

[26] P. Raiteri, D.B. Migas, L. Miglio, A. Rastelli, and H. von Kanel. *Phys. Rev. Lett.*, 88:256103, 2002.

[27] F. Liu G.-H. Lu. *Phys. Rev. Lett.*, 94:176103, 2005.

[28] C.M. Retford, M. Asta, M.J. Miksis, P.W. Voorhees, and E.B. Webb III. *Phys. Rev. B*, 75:075311, 2007.

[29] F. M. Ross, R. M. Tromp, and M. C. Reuter. *Science*, 286:1931, 1999.

[30] A.-L. Barabási I. Daruka, J. Tersoff. *Phys. Rev. Lett.*, 82:2753, 1999.

[31] R. Stanley Williams, G. Medeiros-Ribeiro, T.I. Kamins, and D.A.A. Ohlberg. *Annu. Rev. Phys. Chem.*, 51:527, 2000.

[32] M. De Seta, G. Capellini, F. Evangelisti, and C. Spinella. *J. Appl. Phys.*, 92:614, 2002.

[33] Z. Gai, X. Li, R.G. Zhao, and W.S. Yang. *Phys. Rev. B*, 57:R15060, 1998.

[34] W. Ranke. *Phys. Rev. B*, 41:5243, 1990.

[35] A.A. Stekolnikov, J. Furthmuller, and F. Bechstedt. *Phys. Rev. B*, 68:205306, 2003.

[36] F. Montalenti, P. Raiteri, D.B. Migas, H. von Kanel, A. Rastelli, C. Manzano, G. Costantini, U. Denker, O.G. Schmidt, K. Kern, and L. Miglio. *Phys. Rev. Lett.*, 93:216102, 2004.

[37] X.Z. Liao, J. Zou, D.J.H. Cockayne, J. Qin, Z.M. Jiang, X. Wang, and R. Leon. *Phys. Rev. B*, 60:15605, 1999.

[38] S.A. Chaparro, Y. Zhang, and J. Drucker. *Appl. Phys. Lett.*, 76:3534, 2000.

[39] A. Rastelli, M. Kummer, and H. von Kanel. *Phys. Rev. Lett.*, 87:256101, 2001.

[40] M. Stoffel, A. Rastelli, J. Tersoff, T. Merszhanova, and O. G. Schmidt. *Phys. Rev. B*, 74:155326, 2006.

[41] E. Sutter, P. Sutter, and J.E. Bernard. *Appl. Phys. Lett.*, 84:2262, 2004.

[42] Z. Gai, R.G. Zhao, W. Li, Y. Fujikawa, T. Sakurai, and W.S. Yang. *Phys. Rev. B*, 64:125201, 2001.

[43] Y. Tu and J. Tersoff. *Phys. Rev. Lett.*, 98:096103, 2007.

[44] G. Capellini, M. De Seta, and F. Evangelisti. *Appl. Phys. Lett.*, 78:303, 2001.

[45] M. Floyd, Y. Zhanga, K.P. Driver, J. Drucker, P.A. Crozier, and D.J. Smith. *Appl. Phys. Lett.*, 82:1473, 2003.

[46] T.U. Schulli, M. Stoffel, A. Hesse, J. Stangl, R.T. Lechner, E. Wintersberger, M. Sztucki, T.H. Metzger, O.G. Schmidt, and G. Bauer. *Phys. Rev. B*, 71:035326, 2005.

[47] G. Katsaros, G. Costantini, M. Stoffel, R. Esteban, A. M. Bittner, A. Rastelli, U. Denker, O. G. Schmidt, and K. Kern. *Phys. Rev. B*, 72:195320, 2005.

[48] U. Denker, M. Stoffel, and O. G. Schmidt. *Phys. Rev. Lett.*, 90:196102, 2003.

[49] A. Rastelli, M. Stoffel, A. Malachias, T. Merdzhanova, G. Katsaros, K. Kern, T.H. Metger, and O.G. Schmidt. *Nano Lett.*, 8:1404, 2008.

[50] J. Tersoff. *Phys. Rev. B*, 39:5566, 1989.

[51] D. Pachinger, H. Groiss, H. Lichtenberger, J. Stangl, G. Hesser, and F. Schaffler. *Appl. Phys. Lett.*, 91:233106, 2007.

[52] F.K. Le Goues, M.C. Reuter, J. Tersoff, M. Hammar, and R.M. Tromp. *Phys. Rev. Lett.*, 73:300, 1994.

[53] F.M. Ross, J. Tersoff, M.C. Reuter, F.K. Le Goues, and R.M. Tromp. *Microsc. Res. Tech.*, 42:281, 1998.

[54] T. Merdzhanova, S. Kiravittaya, A. Rastelli, M. Stoffel, U. Denker, and O.G. Schmidt. *Phys. Rev. Lett.*, 96:226103, 2006.

[55] A. Portavoce, R. Hull, M.C. Reuter, and F.M. Ross. *Phys. Rev. B*, 76:235301, 2007.

[56] A. Marzegalli, V. A. Zinovyev, F. Montalenti, A. Rastelli, M. Stoffel, T. Merdzhanova, O. G. Schmidt, and L. Miglio. *Phys. Rev. Lett.*, 99:235505, 2007.

[57] E. M. Liftshitz. *Theory of elasticity.* Elsevier, 1986.

[58] J. Tersoff and F.K. Le Goues. *Phys. Rev. Lett.*, 72:3570, 1994.

[59] V.A. Zinovyev, G. Vastola, F. Montalenti, and L. Miglio. *Surf. Sci.*, 600:4777, 2006.

[60] F. Stillinger and T.A. Weber. *Phys. Rev. B*, 31:5262, 1985.

[61] M. G. Fyta, I. N. Remediakis, P. C. Kelires, and D. A. Papaconstantopoulos. *Phys. Rev. Lett.*, 96:185503, 2006.

[62] L. Martinelli, A. Marzegalli, P. Raiteri, M. Bollani, F. Montalenti, L. Miglio, D. Chrastina, G. Isella, and H. von Känel. *Appl. Phys. Lett.*, 84:2895, 2004.

[63] P. Sonnet and P.C. Kelires. *Phys. Rev. B*, 66:205307, 2002.

[64] G. Medeiros-Ribeiro and R. S. Williams. *Nano Letters*, 7:223, 2007.

[65] R. Magalhaes-Paniago, G. Medeiros-Ribeiro, A. Malachias, S. Kycia, T.I. Kamins, and R. Stan Williams. *66*, Phys. Rev. B:245312, 2002.

[66] J. Tersoff, C. Teichert, and M.G. Lagally. *Phys. Rev. Lett.*, 76:1675, 1996.

[67] M.A. Makeev and A. Madhucar. *Phys. Rev. Lett.*, 86:5542, 2001.

[68] R. Marchetti, F. Montalenti, L. Miglio, G. Capellini, M. De Seta, and F. Evangelisti. *Appl. Phys. Lett.*, 87:261919, 2005.

[69] G. Capellini, M. De Seta, F. Evangelisti, V. Zinovyev, G. Vastola, F. Montalenti, and L. Miglio. *Phys. Rev. Lett.*, 96:106102, 2006.

[70] F. Montalenti, A. Marzegalli, G. Capellini, M. De Seta, and L. Miglio. *J.Phys.; Condens. Matter*, 19:225001, 2007.

[71] U. Denker, A. Rastelli, M. Stoffel, J. Tersoff, G. Katsaros, G. Costantini, K. Kern, N.Y. Jin-Phillipp, D.E. Jesson, and O.G. Schmidt. *Phys. Rev. Lett.*, 94:216103, 2005.

[72] M. Stoffel, A. Rastelli, S. Kiravittaya, , and O.G. Schmidt. *Phys. Rev. B*, 72:205411, 2005.

[73] O.E. Shklyaev, M.J. Beck, M. Asta, M.J. Miksis, and P. W. Voorhees. *Phys. Rev. Lett.*, 94:176102, 2005.

[74] R. Phillips. In R. Phillips, editor, *Crystals, Defects and Microstructures Modeling Across Scales*, pages 72–78. Cambridge University Press, U.K., 2001.

[75] H.T. Johnson and L.B. Freund. *J. Appl. Phys.*, 81:6081, 1997.

[76] Y. Tu and J. Tersoff. *Phys. Rev. Lett.*, 93:216101, 2004.

[77] M. De Seta, G. Capellini, and F. Evangelisti. *Phys. Rev. B*, 77:045431, 2008.

[78] B. J. Spencer and M. Blanariu. *Phys. Rev. Lett.*, 95:206101, 2005.

[79] C. Lang, D. J. H. Cokayne, and D. Nguyen-Manh. *Phys. Rev. B*, 72:155328, 2005.

[80] P. C. Kelires. *J. Phys.: Condens. Matter*, 16:S1485, 2004.

[81] Ph. Sonnet and P. C. Kelires. *Appl. Phys. Lett.*, 85:203, 2004.

[82] G. Hadjisavvas and P. C. Kelires. *Phys. Rev. B*, 72:075334, 2005.

[83] R. Marchettti, F. Montalenti, L. Miglio, G. Capellini, M. De Seta, and F. Evangelisti. *Appl. Phys. Lett.*, 87:261919, 2005.

[84] G. Medeiros-Ribeiro, A. M. Bratkovski, T. I. Kamins, D. A. A. Ohlberg, and R. S. Williams. *Science*, 279:353, 1998.

[85] F. Boscherini, G. Capellini, L. Di Gaspare, F. Rosei, N. Motta, and S. Mobilio. *Appl. Phys. Lett.*, 76:682, 2000.

[86] A. Malachias, S. Kycia, G. Medeiros-Ribeiro, R. Magalhaes-Paniago, T. I. Kamins, and R. S. Williams. *Phys. Rev. Lett.*, 91:176101, 2003.

[87] T. U. Schülli, M.I. Richard, G. Renaud, V. Favre-Nicolon, E. Wintersberger, and G. Bauer. *Appl. Phys. Lett.*, 89:143114, 2006.

[88] F. Ratto, G. Costantini, A. Rastelli, O. G. Schmidt, K. Kern, and F. Rosei. *J. Exp. Nanosci.*, 1:279, 2006.

[89] G. Costantini, A. Rastelli, C. Manzano, R. Songmuang, O. G. Schmidt, and K. Kern. *Appl. Phys. Lett.*, 85:5673, 2004.

[90] L. Wang, A. Rastelli, and O. G. Schmidt. *J. Appl. Phys.*, 100:064313, 2006.

[91] Z. Zhong, W. Schwinger, F. Schäffler, G. Bauer, G. Vastola, F. Montalenti, and Leo Miglio. *Phys. Rev. Lett.*, 98:176102, 2007.

[92] G. Vastola, R. Gatti, A. Marzegalli, F. Montalenti, and L. Miglio. In Z. M. Wang, editor, *Self-Assembled Quantum Dots*, pages 421–438. Springer, N.Y., 2008.

[93] J.F. Justo, A. Fazzio, and A. Antonelli. *J. Phys.: Condens. Matter*, 12:10039, 2000.

[94] A.T. Blumenau, M.I. Heggie, C.J. Fall, R. Jones, and T. Frauenheim. *Phys. Rev. B*, 65:205205, 2002.

[95] I.N. Remediakis, D.E. Jesson, and P.C. Kelires. *Phys. Rev. Lett.*, 97:255502, 2006.

[96] E. van der Giessen and A. Needleman. *Modell. Simulat. Mat. Sci. Eng.*, 3:689, 1995.

[97] R. Gracie, J. Oswald, and T. Belytschko. *J. Mech. Phys. Solids*, 56:200, 2008.

[98] J. P. Hirth and J. Lothe. *Theory of dislocations*. Krieger publishing company, 1982.

[99] B. Devincre, L.P. Kubin, C. Lemarchand, and R. Madec. *Mater. Sci. Eng. A*, 309:211, 2001.

[100] T. Belytschko and R. Gracie. *Int. J. Plasticity*, 23:1721, 2007.

[101] R. Hull. *Properties of Silicon Germanium and SiGe:Carbon*. Eric Kasper and Klara Lyutovich, University of Stuttgart, Germany, 2000.

[102] A.K. Head. *Proc. Phys. Soc. Sec. B*, 66:793, 1953.

[103] R. Gracie, G. Ventura, and T. Belytschko. *Int. J. Numer. Meth. Engng*, 69:423, 2007.

[104] E. Bugiel, M. Lewerenz, and H. J. Osten. *Physica E*, 37:250, 2007.

[105] X. Yu, W. Seifert, O. F. Vyvenko, M. Kittler, T. Wilhelm, and M. Reiche. *Appl. Phys. Lett.*, 93:041108, 2008.

[106] M. A. Lourenco, M. Milosavljevic, G. Shao, R. M. Gwilliam, , and K. P. Homewood. *Thin Solid Films*, 515:8113, 2007.

[107] J. S. Park, M. Curtin J. Bai, B. Adekore, M. Carroll, and A. Lochtefeld. *Appl. Phys. Lett.*, 90:052113, 2007.

[108] J. Z. Li, J. Bai, J. S. Park, B. Adekore, K. Fox, M. Carroll, A. Lochtefeld, and Z. Shellenbarger. *Appl. Phys. Lett.*, 91:02111, 2007.

[109] E. A. Fitzgerald, G. P. Watson, D. G. Ast, P. D. Kirchner, G. D. Pettit, and J. M. Woodall. *J. Appl. Phys.*, 65:2220, 1989.

[110] R. Hammond, P. J. Phillips, T. E. Wall, E. H. C. Parker, T. Graf, H. von Kanel, and A. J. Shields. *Appl. Phys. Lett.*, 71:2517, 1997.

[111] M. A. Lutz, R. M. Feenstra, F. K. LeGoues, P. M. Mooney, and J.O. Chu. *Appl. Phys. Lett.*, 66:724, 1995.

[112] R. Gatti, A. Marzegalli, V.A. Zinovyev, F. Montalenti, and L. Miglio. *Phys. Rev. B*, 78:184104, 2008.

[113] W. Cai, A. Arsenlis, C. R. Weinberger, and V. V. Bulatov. *J. Mech. Phys. Sol.*, 54:561, 2006.

[114] M. Grydlik, M. Brehm, F. Hackl, H. Groiß, T. Fromherz, F. Schäffler, and G. Bauer. *New J. Phys.*, 12:063002, 2010.

[115] K. Sato, M. Shikida, T. Yamashiro, K. Asaumi, Y. Iriye, and M. Yamamoto. *Sensors and Actuators*, 73:131, 1999.

[116] J. Tersoff. *Phys. Rev. B*, 37:6991, 1988.

[117] A. Marzegalli, F. Montalenti, and L. Miglio. *Appl. Phys. Lett.*, 86:041912, 2005.

[118] A. Marzegalli, F. Montalenti, and L. Miglio. *J. Phys. Condens. Matter*, 17:7505, 2005.

[119] M. Peach and J.S. Koehler. *Phys. Rev.*, 80:436, 1950.

[120] B.J. Spencer and J. Tersoff. *Phys. Rev. B*, 63:205424, 2001.

[121] A. Rastelli, M. Stoffel, G. Katsaros, J. Tersoff, U. Denker, T. Merdzhanova, G.S. Kar, G. Costantini, K. Kern, H. von Kanel, and O.G. Schmidt. *Microelectronics Journal*, 37:1471, 2006.

[122] U. Jain, S.C. Jain, A.H. Harker, and R. Bullough. *J. Appl. Phys.*, 77:103, 1995.

[123] Y.J. Chen, I.H. Wilson, C.S. Lee, J.B. Xum, and M.L. Yu. *J. Appl. Phys.*, 82:5859, 1997.

[124] K.L. Westra, A.W Mitchell, and D.J Thomson. *J. Appl. Phys.*, 74:3608, 1993.

[125] T. Merdzhanova, A. Rastelli, M. Stoffel, S. Kiravittaya, and O.G. Schmidt. *Journal of Crystal Growth*, 301-302:319, 2007.

[126] M. Hammar, F.K. Le Goues, J. Tersoff, M.C. Reuter, and R.M. Tromp. *Surf. Sci.*, 349:129, 1996.

[127] K. Tillman and A. Forster. *Thin Solid Films*, 368:93, 2000.

[128] A. Atkinson and S.C. Jain. *J. Phys.: Condens. Matter*, 5:4595, 1993.

[129] B. Devincre. Three dimensional stress fields expressions for straight dislocation segments. *Solid State Communications*, 93:875–878, 1995.

[130] A. J. E. Foreman. The bowing of a dislocation segment. *Philosophical Magazine*, 15:1011–1021, 1967.

[131] C. de Sansal. *Plasticité et effect de taille dans dans les polycristaux á grains micromÂ ´etriques: simulations mésoscopiques et modélisation.* PhD thesis, Ecole Centrale Paris, 2007.

[132] K. W. Schwarz. Simulation od dislocations on the mesoscopic scale. I. methods and examples. *Journal of Applied Physics*, 85:108, 1999.

[133] Yu. L. Iunin and V. I. Nikitenko. Modes of kink motion on dislocations in semiconductors. *Philosophical Magazine*, 45:1239–1246, 2001.

[134] T. E. Mitchell. *Progress in Applied Materials Research*, 6:117, 1964.

[135] J. Weertman and J. R. Weertman. *Elementary Dislocation Theory.* Macmillan Series in Materials Science, 1964.

[136] J. Weertman and J. R. Weertman. *Advanced Silicon and Semiconducting Silicon-Alloy Based Materials and Devices.* Macmillan Series in Materials Science, 1964.

[137] J. Y. Tsao. *Materials Fundamentals of Molecular Beam Epitaxy.* Academic Press, Albuquerque, 1997.

[138] E. A. Fitzgerald. *Annu. Rev. Mater. Sci*, 25:417, 1995.

[139] P. M. Mooney. *Materials Science and Engineering*, R17:105, 1996.

List of publications derived from the Ph.D. work

1. G. Vastola, R. Gatti, A. Marzegalli, F. Montalenti, L. Miglio. *Self Assembled Quantum Dots*, editeb by Zhiming M. Wang (Springer, Berlin, 2008), pp. 421-438.

2. R. Gatti, F. Uhlik, F. Montalenti. *"Intermixing in heteroepitaxial islands: fast, self-consistent calculation of the concentration profile minimizing the elastic energy "*, New J. Phys. **10**, 083039 (2008).

3. R. Gatti, A. Marzegalli, V. A. Zinovyev, F. Montalenti, Leo Miglio. *"Modeling the plastic relaxation onset in realistic SiGe islands on Si(001) "*, Phys. Rev. B **78**, 184104 (2008).

4. F. Uhlik,R. Gatti and F. Montalenti. *"A fast computational method for determining equilibrium concentration profiles in intermixed nanoislands"* , J. Phys.: Condens Matter **21**, 084217 (2009).

5. D.Digiuni,R.Gatti and F. Montalenti. *"Aspect-ratio-dependent driving force for nonuniform alloying in Stranski-Krastanow islands"*, Phys. Rev. B **80**, 155436 (2009).

6. A. Trita, F. Bragheri, I. Cristiani, V. Degiorgio, D. Chrastina, D. Colombo, G. Isella, H. von Känel, F. Gramm, E. Müller, M. Döbeli, E. Bonera, R. Gatti, F. Pezzoli, E. Grilli, M. Guzzi and L. Miglio. *"Impact of misfit dislocations on wavefront distortion in Si/SiGe/Si optical waveguides"*, Optics Communications **282**, 4716 (2009)

7. F. Boioli, V. A. Zinovyev, R. Gatti, A. Marzegalli, F. Montalenti, M. Stoffel,T. Merdzhanova, L. Wang, F. Pezzoli, A. Rastelli, O. G. Schmidt, Leo Miglio. *"Self-ordering of dislocation loops in epitaxial SiGe islands on Si(001)"*, submitted to Phys. Rev. B.

8. R. Gatti, F. Boioli, M. Grydlik, M. Brehm, T. Fromherz, F.Schäffler, Leo Miglio. *"Dislocation engineering in SiGe heteroepitaxial films on patterned Si (001) substrates"*, submitted to Appl. Phys. Lett.

9. R. Gatti, B.Devincre and L. Miglio. *"Dynamics of plastic relaxation in SiGe islands simulated with DD simulations"*, in preparation.